General Disclaimer

One or more of the Following Statements may affect this Document

- This document has been reproduced from the best copy furnished by the organizational source. It is being released in the interest of making available as much information as possible.

- This document may contain data, which exceeds the sheet parameters. It was furnished in this condition by the organizational source and is the best copy available.

- This document may contain tone-on-tone or color graphs, charts and/or pictures, which have been reproduced in black and white.

- This document is paginated as submitted by the original source.

- Portions of this document are not fully legible due to the historical nature of some of the material. However, it is the best reproduction available from the original submission.

[redacted] RE-507

SEGREGATION EFFECTS DURING SOLIDIFICATION IN WEIGHTLESS MELTS

Prepared for Contract No. NAS 8-29662 by

Chou Li

Research Department
Grumman Aerospace Corporation
Bethpage, New York 11714

Sponsored by

National Aeronautics and Space Administration
George C. Marshall Space Flight Center
Alabama, 35812

July 1975

SEGREGATION EFFECTS DURING SOLIDIFICATION IN WEIGHTLESS MELTS

FINAL REPORT

by

Chou Li

Research Department
Grumman Aerospace Corporation
Bethpage, New York 11714

Partially supported under
Contract NAS 8-29662

Sponsored by

National Aeronautics and Space Administration
George C. Marshall Space Flight Center
Marshall Space Flight Center
Alabama 35812

July 1975

Approved by: Charles E. Mack, Jr.
Charles E. Mack, Jr.
Director of Research

This report was prepared by Grumman Aerospace Corporation under partial support under Contract NAS 8-29662 sponsored by the George C. Marshall Space Flight Center of the National Aeronautics and Space Administration.

TABLE OF CONTENTS

LIST OF ILLUSTRATIONS

LIST OF TABLES

ACKNOWLEDGEMENT

The author wishes to thank Messrs. R. C. Ruff and G. Arnett of Marshall Space Flight Center for directing and monitoring this contract. He also wishes to thank Dr. J. Bredt of NASA Headquarters in Washington, D. C. for helpful discussions. Additional thanks are due to M. Gershinsky of Grumman Data Systems Corporation for the development of the computer programs; to D. Nickal of Materials Research Corporation of Orangeburg, New York for help in GaAs crystal growth; to G. Busch of Grumman Materials Research and Prof. F. F. Y. Wang of State University of New York at Stony Brook for characterization of GaAs samples; and to R. Erath and J. Gardner of Grumman Research Department for vibration measurements and data analyses. He is also grateful to Dr. G. Geschwind of the Research Department for critical reading of and comments on the manuscript.

SUMMARY

This report discusses the work partially supported under NASA Contract NAS 8-29662, "Segregation Effects During Solidification in Weightless Melts." The contract covered the period from July 1, 1973 to June, 1975.

During the contract period, we unexpectedly discovered a unique segregation pattern and evidence of strong convection currents in GaAs crystal growth. We found, also unexpectedly, some beneficial effects from vibration during GaAs growth. All these have clear and important implications in space processing.

In addition, the generalized problem of determining the temperature and solute concentration profiles during directional solidification of binary alloys with surface evaporation has been mathematically formulated. Realistic initial and boundary conditions have been defined and a computer program has been developed and checked out.

The program computes the positions of two moving (evaporation and solidification) boundaries, their velocities of movement, and the temperature and solute concentration profiles in the semi-infinite material body at selected instants of time.

The program has the following unique features:

- Two moving boundaries are involved, i.e., the evaporative boundary and freezing boundary
- Surface evaporation, and its related effects such as material loss, evaporative segregation, and surface cooling due to the heat evaporation, have been considered
- Surface temperature is realistically determined by the combined effect of heat radiation, evaporative cooling, and thermal diffusion
- Material parameters such as solid and liquid densities, specific heats, thermal conductivities, mass diffusivities, and latent heat of fusion or evaporation, can all vary with both the temperature and composition
- Realistic phase diagrams involving curved liquidus and solidus lines are used

Typical computed results for combined evaporation and solidification are included. An econotechnical model of crystal growth is presented. This model, when fully developed, will allow: prediction of crystal size, quality, and cost; systematic selecting of the best growth equipment or alloy system; optimization of growth or material parameters, and maximization of zero-gravity effects.

An important aspect of this work has been to study segregations by microprobing GaAs samples on transverse depth profiles from different locations on the sample surface. Analyses of the probe data reveal a unique segregation pattern that cannot be explained by existing phase diagrams. The variations of solidification velocities on the surface also are unexpected and could be explained by us only on the basis of strong convection currents in the growth melt. We therefore conclude that space-grown GaAs crystals by the same horizontal Bridgeman method should give more uniform and perfect crystals, in line with other Skylab crystal growth results.

Another important aspect of this work has been to study vibration effects on crystal growth. Specifically, we have carefully and systematically documented the different sources of vibrations on one set of GaAs growth furnaces and, in particular, fully characterized the beneficial vibration effects due to an unbalanced motor. The relation of vibration to liquid mixing and space processing is discussed. The report also includes a section on a GaAs statistically designed experiment. This experiment shows that with only 14 crystals, properly planned, we can study the effects of melt and growth variables on solute segregation and crystal quality. We believe that such, or similarly designed, experiments are particularly useful in space processing where the sample numbers are necessarily limited and the cost of experiments is too high to tolerate inefficiency.

1. INTRODUCTION

Space processing is moving closer to reality. Bigger, better, and more uniform single crystals of important semiconductors and welds or brazes of improved properties have already been made in space, as reported in the Third Space Processing Symposium at Marshall Space Flight Center. Although processing of structural materials may certainly have a profit potential in the long range, it appears that the high cost per pound of single-crystal electronic and optical materials makes these materials the most desirable contenders for immediate profitable returns from space processing. A selected single crystal study is, therefore, highly desirable to help us understand the segregation effects during solidification in weightless melts.

Important tools for understanding these segregation effects are analytic solutions or computer programs that simulate or predict what actually happens during space manufacturing. Such solutions and programs are probably necessary in space processing and other experiments where available time and experimental facilities are limited, the cost per sample or experiment is very high, and yet only a limited total number of tests or test samples can be conducted.

Theoretical predictions often save time while computer simulation saves cost. Specifically, analytic solutions and computer programs allow us to answer many questions during the planning or execution of space experiments on material solidification, such as learning:

- What phenomena are most important and what other phenomena are negligible
- Which influences are favorable to our understanding of weightless solidification and which are not
- What conditions lead to optimal combination of the favorable influences or elimination of the unfavorable ones
- What sample and processing conditions should be used
- What is the best way to analyze the resultant samples for understanding a particular phenomenon or influence
- How to save time and money, that is, how to maximize scientific return.

We have developed a number of analytic solutions relating to solidification and evaporation (Refs. 1-3). Several important computer programs have also been developed. Some of these solutions and programs were developed under our Contract NAS 8-27891, and they are already proving useful in correlating experimental results (Refs. 4 and 5).

However these analytic solutions and computer programs are still in their early stages of development. The physical models involved are very simple and require considerable improvements to be used for other applications. It is, therefore, an

important objective of this contract to refine and improve these models and the resultant analytic solutions and computer programs.

These refined solutions and programs are more widely useful, have greater predictive value, and provide more accurate results. Such accuracies are absolutely necessary to separate the rather subtle zero-gravity effects on solidification, in the presence of noise due to other unavoidable or unanticipated but ever-present miscellaneous effects. As a result of this continued work, more efficient space experiments and greater scientific returns appear possible. More meaningful solidification experiments and fuller utilization of the unique space environment may also result.

Of course, the predicted results of our refined solutions and programs should first be checked with selected experiments. Another objective of this contract has been, therefore, to design unique experiments to correlate the numerical results to actual solidification processes.

A. Review of Previous Contract

Under our NASA Contract NAS 8-27891, "Segregation Effects During Solidification in Weightless Melts" (Ref. 3), two types of melt segregation effects were studied: evaporative segregation, or segregation due to surface evaporation, and freezing segregation, or segregation due to liquid-solid phase transformation.

These segregation effects are closely related. In fact, evaporative segregation always precedes freezing segregation to some degree and must often be studied prior to performing meaningful solidification experiments. This is particularly true since evaporation may cause the melt composition, at least at the critical surface regions or layers, to be affected manyfold, often within seconds, so that at the surface region or layer the melting point and other thermophysical properties, nucleation characteristics, base for undercooling, and critical velocity to avoid constitutional supercooling, may be completely unexpected. More comments about the importance of evaporation is given in Appendix A.

To predict the segregation effects of solidification time and temperature and to correlate these predictions with actual experimental data, "normal evaporation equations" were developed (Refs. 1, 4-6). An evaporative congruent temperature (or equi-evaporative temperature) was then defined and listed for various binary or ternary alloys. Knowing these congruent temperatures and the solute and solvent evaporating rates, one can predict the type (solute depletion or enrichment) and magnitude of compositional or constitutional changes on the critical melt surface. One application of this unique temperature is to explain, predict, or plan "anomalous" evaporative or constitutional melting (on cooling) or solidification (on heating) experiments. We then computed for a simple model the reactive jetting forces due to surface evaporation and, in particular, showed that these forces can be very substantial on a differentially heated sample and may completely destroy the unique zero-gravity environment in space manufacturing (Ref. 7). In addition, these jetting forces may initiate surface deformation and vibration or other fluid disturbances, and may even produce some convection currents not normally anticipated. These studies also showed which sample materials are preferable, which should be avoided, and what impurities are

harmful in producing excessive jetting or effective as stabilizing influences. The relationship between normal evaporation and normal freezing was then considered. Finally, applications of evaporation to space manufacturing concerning material loss and dimensional control, compositional changes, evaporative purification, surface cooling, materials standards, and freezing data interpretation were briefly described.

In the area of segregation due to solidification, we explained in some detail the normal freezing process and its successful use in the semiconductor industry. Various constitutional diagrams demonstrated the desirability of using nonconstant segregation coefficient techniques in metallurgical studies. We then stated the basic normal freezing differential equation, together with its solutions for cases where the liquidus and solidus are quadratic, cubic, high-degree polynominal, and exponential functions of the melt temperature. The meaning of constant segregation coefficient was discussed, together with the associated errors due to curvatures of the liquidus and solidus lines and the best value of constant segregation coefficient for a given solidification experiment. Numerical methods for computing the normal freezing behavior were then given (see Appendix B). Finally, as an example, the steady state solidification of the Ni-Sn system under conditions of limited liquid diffusion and nonconstant segregation coefficients was described. This system was studied in the M553 experiment on Skylab.

B. Work Areas of Present Contract

The present contract builds on the results of the previous contract. New results and improvements are presented in the following areas:

- In the computer program:
  - Realistic surface conditions of radiation and evaporation have been incorporated
  - Allow material parameters (specific heat, diffusivities,. . .) to vary with temperature and solute concentration
  - Develop a simple crystal growth model.
- Computer results for combined evaporation and solidification are presented
- Studies of segregation in GaAs crystals
- A statistically designed GaAs Experiment
- Investigation of some vibration effects on GaAs crystal growth

2. COMPUTER PROGRAM DEVELOPED UNDER PRESENT CONTRACT

A. Introduction

Under the present contract, we have extended the programs to allow for reasonable variation of physical properties. The approach taken is to base the values of physical properties upon extrapolated values of temperature and concentration, and then to determine the values of temperature and concentration. The process is then repeated by re-evaluations of the physical properties. Other modifications of our original program are: 1) to store the physical properties for each of the mesh points and to employ the appropriate quantities at each step, and 2) to recheck the mass and heat diffusion equations to make certain that the constancy of these properties is not assumed.

Another major program modification has been to include evaporation effects. This includes evaporation before solidification that is mathematically identical to the problem of simple solidification in binary alloys. After solidification starts, significant evaporation may still exist. We then have to deal with two moving (solid-gas and solid-liquid) boundaries located at y(t) for evaporation and at z(t) for solidification, as will be described.

The initial and boundary conditions have also been modified to make the problem more physically meaningful. One such modification is to include a surface heat radiative loss term involving T^4. This term affects the convergence of the problem and creates the need for different algorithms. As reported previously (Ref. 3) the surface cooling due to evaporation is negligible for many metallic systems such as nickel and iron alloys, or other higher melting materials.

To obtain solutions for realistic boundary conditions and to include various mass transfer effects, numerical solutions of the partial differential equations of heat and mass transfer are required. We have again used the finite difference method to obtain the numerical solution.

The boundary conditions for surface temperature include radiation cooling as given by the Stefan-Boltzmann equation and also include evaporative cooling for both components of the alloy. Raoult's law has been assumed in determining the evaporation rates. At the interface it is assumed that the temperature and concentration relationships for each phase are given by the constitutional diagram for the alloy. The temperature dependence of the thermal and mass diffusion coefficients are allowed for each phase.

B. Evaporative Solidification of a Binary Alloy

Given a semi-infinite binary alloy melt, initially at concentration C_o and temperature T_o, we consider the solidification of the alloy due to surface heat loss by evaporation and radiation (Fig. 1). There are two separate regimes to be considered. The first is concerned with temperature and concentration variations

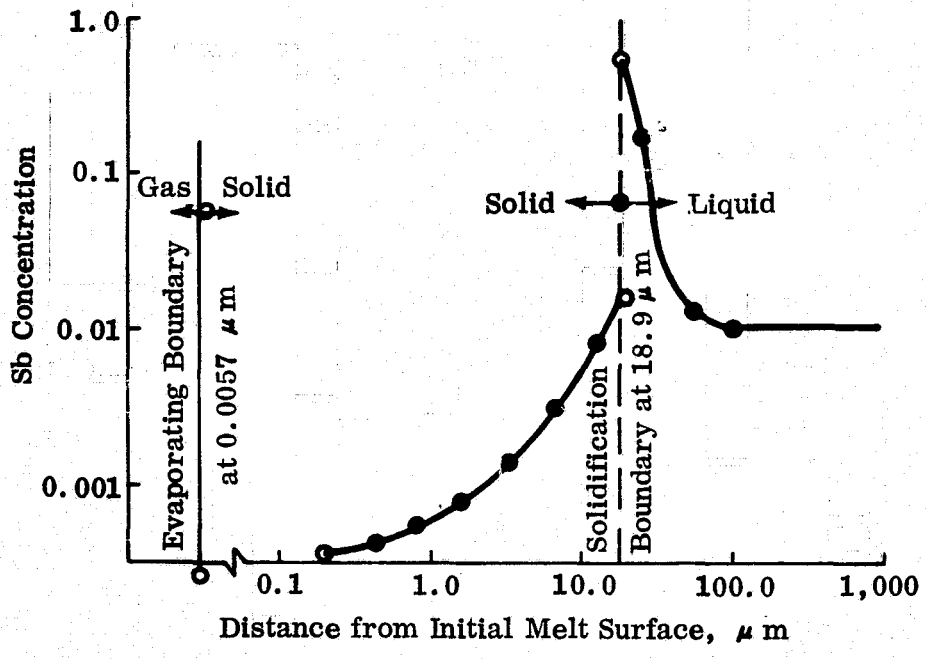

Fig. 1 Evaporation-Solidification of 0.01 Sb-Ge Initially at 970°C at 0.01 Second

before solidification begins; the evaporation causes the original liquid-vapor boundary to change. Thus, we have a moving boundary problem. The second regime begins with the solidification which introduces a boundary between the freezing solid and remaining liquid phases whose compositions, we assume, follow the phase diagram, i.e., solidus and liquidus curve relations hold. Consequently, after solidification begins, there are two moving boundaries: one is the evaporative boundary and the other is the freezing or solidification boundary.

1. Equations at the Evaporative Boundary

We denote the evaporative boundary as $x = y(t)$ where $y(0) = 0$. The evaporation rates in $mol/m^2/sec$ for pure solute and solvent are, respectively (Ref. 6):

$$U = K_e \, 10^{A_u - (B_u/T)} (M_u T_s)^{-\frac{1}{2}}$$

$$V = K_e \, 10^{A_v - (B_v/T)} (M_v T_s)^{-\frac{1}{2}}$$

where $K_e = 5.83 \times 10^{-5}$, M_u, M_v are molecular weights for solute and solvent atoms, T_s is the evaporating surface temperature in ^oK, and A_u, B_u, A_v, B_v are the evaporating constants for solute and solvent, respectively. If ρ_u and ρ_v are the solute and solvent densities, then:

$$\frac{dy}{dt} = \frac{UM_uC}{\rho_u} + \frac{VM_v(1 - C)}{\rho_v}$$

where C is the concentration at the moving boundary.

The heat loss rate equation at the boundary due to radiation and evaporation is given by:

$$\frac{\partial T}{\partial t} = -\epsilon \sigma T_s^4 - U\gamma_u C - V\gamma_v(1 - C)$$

where ϵ is emissivity coefficient, σ the Stefan-Boltzmann constant, and γ_u and γ_v are specific heats for solute and solvent, respectively.

The general ambient temperature T_A may not be at the absolute zero(0^oK). The T_s^4 term in the equation should, then, be replaced by$(T_s^4 - T_A^4)$.

The equation for the rate of concentration change is:

$$\frac{\partial C}{\partial t} = -(U - V)C$$

Since the evaporative boundary is a moving one, and since both the evaporation temperature T and solute concentration C are functions of distance x = y(t) and time t, i.e., T = T(x,t) and C = C(x,t), the total derivatives $\frac{dT}{dt}$ and $\frac{dC}{dt}$ may be obtained from the partials, i.e.:

$$\frac{dT}{dt} = \frac{\partial T}{\partial t} + \left(\frac{\partial T}{\partial x}\right)_{x = y}\left(\frac{dy}{dt}\right)$$

$$\frac{dC}{dt} = \frac{\partial C}{\partial t} + \left(\frac{\partial C}{\partial x}\right)_{x = y}\left(\frac{dy}{dt}\right)$$

where $\frac{\partial T}{\partial x}$ and $\frac{\partial C}{\partial x}$ are evaluated at the moving boundaries.

Given $\frac{dy}{dt}$, $\frac{dT}{dt}$, and $\frac{dC}{dt}$, we can integrate for y, T, and C for the moving boundary using a modified Euler method.

$$v^{(i)}_{t+\Delta t} = v_t + \Delta t \left(\frac{dv}{dt}\right)_t$$

$$v^{(i+1)}_{t+\Delta t} = v_t + \frac{\Delta t}{2}\left[\left(\frac{dv}{dt}\right)_t + \left(\frac{dv}{dt}\right)^{(i)}_{t+\Delta t}\right]$$

where $\frac{dv^{(i)}}{dt}$ is the value of the derivative at time $t + \Delta t$ using the value $v^{(i)}$ for v.

To determine $\frac{\partial T}{\partial x}$ at time t and $t + \Delta t$ requires knowledge of the distribution of temperatures at both times. Those at time $t + \Delta t$ are initially approximated by an extrapolation and are corrected using an approximated value of the temperature of the evaporating boundary with the heat diffusion difference equations. Since the change in temperature at the boundary is greatest due to the heat of evaporation, more iterations are applied to determine it than to the determination of temperature distribution by means of diffusion equations. Similar considerations hold for the determination of $\frac{\partial C}{\partial x}$ and $\frac{dC}{dt}$.

The computations of the position of the evaporation boundary [y = y(t)] , temperature (T), and solute concentration (C) at this boundary constitute an initial value problem in ordinary differential equations. Thus, given $y_o = O$, $T = T_o$, $C = C_o$, at time t = O, and given also the equations for velocity of movement of this boundary dy/dt, and rate of change of temperature and solute concentration, dT/dt and dC/dt, we can determine for selected times the values of y, T, and C. The method used is an iterated Euler scheme:

$$y_{n+1} = y_n + \frac{\Delta t}{2}\left(y'_n + y'_{n+1}\right)$$

where the initial value y'_{n+1} is taken as y'_n. This scheme must be connected to the problem of determining the temperature and solute concentration distribution within the semi-infinite body because the derivatives dy/dt, DT/dt, and dC/dt depend upon these quantities. The first step is to determine a first approximation of the temperature and solute concentration by extrapolation and then correct these values from the newly approximated values of the boundary position and the temperature and concentration at the boundary.

2. Start of Solidification

To determine the time when solidification has begun, the boundary temperature is compared with the temperature obtained by the inverse function for the liquidus curve evaluated at the boundary concentration. If the former is greater, then solidification has not yet begun. If it is smaller, then solidification has begun. In order to avoid an exact iterative procedure to determine the instant of solidification and to follow it up by a starting procedure for the first time interval thereafter, a simplified approach has been taken that introduces a small error in the evaporative boundary and

freezing boundary. By allowing the temperature to be below the solidification temperature by a small amount and by assuming that the temperatures at both boundaries are the same, a starting value of x = z(t) of the freezing boundary is determined so that the loss in concentration due to solidification is compensated by the gain in concentration at the liquidus. Given the new temperature TI2 below the temperature at which solidification begins, we compute CSS = FS(TI2) and CLL = FL(TI2), the corresponding solid and liquid concentrations given by the phase diagram. To determine DELZ = ZI2 - YI2, the distance between the evaporative boundary and solid-liquid interface, we assume that the solid is entirely at concentration CSS, and the liquid varies linearly from CLL to CC(II2), the concentration at the first mesh point x(II2) after the evaporative boundary. The total concentration is to equal the concentration in the whole regime had no solidification taken place. We assume it to be CL2 computed at YI2 and to vary linearly to CC(II2) at x(II2). This yields the equation:

$$\text{CSS} * \text{DELZ} + (\text{CLL} + \text{CC(II2)})/2 * (\text{x(II2)} - \text{YI2} - \text{DELZ}) = (\text{CL2} + \text{CC(II2)})/2 * (\text{x(II2)} - \text{YI2})$$

Hence:

$$\text{DELZ} * [\text{CSS} - (\text{CLL} + \text{CC(II2)}/2)] = (\text{x(II2)} - \text{YI2}) * (\text{CL2} - \text{CLL})/2$$

where,

$$\text{DELZ} = (\text{CLL} - \text{CL2})/2 * (\text{x(II2)} - \text{YI2}) \div (\text{CLL} + \text{CC(II2)}/2 - \text{CSS})$$

Then,

$$\text{ZI2} = \text{YI2} + \text{DELZ} \text{ and } \frac{dz}{dt} = \frac{\text{DELZ}}{\text{DELTS}}.$$

This enables us to begin the next time step with initial values for $y(t_s)$, $z(t_s)$, $\frac{dy}{dt}$, $\frac{dz}{dt}$, $T\left(y(t_s)\right) = T\left(z(t_s)\right) = \text{TI2}$, and $C\left(y(t_s)\right) = \text{CSS}$, $C_s\left(z(t_s)\right) = \text{CSS}$, $C_\ell\left(z(t_s)\right) = \text{CLL}$.

3. The Two-Boundary Problem-Derivative Estimation

The equations at the freezing boundary are those given in the Grumman Final Report RE-458 to Contract NAS 8-27891 (Ref. 3), with the exception that the freezing boundary is now called x = z(t) and not x = y(t) as in Eq. 49 c-g. At every time step we must compute (in addition to the temperature and concentration at the evaporation boundary) the temperature at the freezing boundary. The concentrations are determined by the phase diagram. The method we employ is that which determines T (the solidification temperature) and $\frac{dz}{dt}$ by means of Eq. (49) f,g. Having obtained $\frac{dz}{dt}$ we obtain z(t) by means of a modified Euler method. Since the Eq. (49) f,g required approximation for $\left(\frac{\partial T_s}{\partial x}\right)_{z,t}$ and $\left(\frac{\partial C_s}{\partial x}\right)_{z,t}$, we must develop techniques for these approximations appropriate to various situations for mesh points. In addition, for the computation $\frac{dy}{dt}$, $\frac{dT}{dt}$, and $\frac{dC}{dt}$ at the evaporative boundary, we also need $\left(\frac{\partial T}{\partial x}\right)_{y,t}$ and $\left(\frac{\partial C}{\partial x}\right)_{y,t}$. When there are two mesh points between y and z, then the

techniques alluded to above are available. This involves determining $\frac{\partial^2 T}{\partial x^2}$ at both y and z and the same for $\frac{\partial^2 C}{\partial x^2}$. When there is only one mesh point between y and z, then $\frac{\partial^2 T}{\partial x^2}$ at both points are the same. When there are no mesh points between y and z, then we can assume either that $\frac{\partial^2 T}{\partial x^2}$ is zero and hence $\left(\frac{\partial T}{\partial x}\right)_y = \left(\frac{\partial T}{\partial x}\right)_z = \frac{T(z) - T(y)}{z - y}$ or that $\frac{\partial T}{\partial x^2} = k \frac{\partial T}{\partial x}$ and hence $\left(\frac{\partial T}{\partial x}\right)_y = \left(1 - \frac{z - y}{2} k\right)\frac{\partial T}{\partial x}$ and $\left(\frac{\partial T}{\partial x}\right)_z = \left(1 + \frac{z - y}{2} k\right)\frac{\partial T}{\partial x}$. The choice of k must be small so that $\frac{\partial^2 T}{\partial x^2} = k \frac{\partial^2 T}{\partial x^2} = k^2 \frac{\partial T}{\partial x}$ is negligible. Thus, since z-y is also very small this option is indistinguishable from $\frac{\partial^2 T}{\partial x^2} = 0$. We have three cases: 1) no mesh points between two boundaries and we assume $\frac{\partial^2 T}{\partial x^2} = 0, \left(\frac{\partial T}{\partial x}\right)_y = \left(\frac{\partial T}{\partial z}\right)_z$; 2) one mesh point between y and z when $\frac{\partial^2 T}{\partial x^2}$ is obtained from the three points and: $\left(\frac{\partial T}{\partial x}\right)_y = \frac{T(z) - T(y)}{z - y} - \frac{(z - y)}{2} - \frac{\partial^2 T}{\partial x^2}$ and $\left(\frac{\partial T}{\partial x}\right)_z = \frac{T(z) - T(y)}{z - y} + \frac{(z - y)}{2} \frac{\partial^2 T}{\partial x^2}$, and 3) when two or more mesh points, say x_i and x_{i+1}, are between v and z so that we can compute $\left(\frac{\partial^2 T}{\partial x^2}\right)_z$ and $\left(\frac{\partial^2 T}{\partial x^2}\right)_y$ separately and distinct. Then: $\left(\frac{\partial T}{\partial x}\right)_y = \frac{T(x_i) - T(y)}{x_i - y} - \frac{(x_i - y)}{2}\left(\frac{\partial^2 T}{\partial x^2}\right)_y$ and $\left(\frac{\partial T}{\partial x}\right)_z = \frac{T(z) - T(x_{i+1})}{z - x_{i+1}} + \frac{(z - x_{i+1})}{2}$ $\left(\frac{\partial^2 T}{\partial x^2}\right)_z$. In general, it is necessary to compute $\frac{\partial^2 T}{\partial x^2}$ and $\frac{\partial^2 C}{\partial x^2}$ in three ways; two ways indicated above for the solid regime and a third for the liquid side of the freezing boundary. It is similarly necessary to compute $\frac{\partial T}{\partial x}$ and $\frac{\partial C}{\partial x}$ in three ways.

4. Boundary and Mesh Points

When boundary points come close to mesh points, the computation of derivatives may be vitiated by closeness to mesh point. Therefore, tests are made to determine when such closeness occurs as usually expressed in terms of a decimal fraction of the interval. In that case, the reference point is moved to the next mesh point and the values of T and C at the skipped mesh point are obtained by linear interpolation. This interpolation depends on which side of the solid-liquid interface the mesh point lies. For the evaporative boundary similar considerations hold.

5. Solution for Remaining Points

The solution for the remaining points is obtained as in the Final Report previously mentioned, pages 3-14 and 3-15 (Ref. 3). One change is, however, necessary because the first mesh point (or more) are no longer under consideration if the evaporative boundary has passed them. The subroutine TRIST is used to solve for the

remaining points. In this subroutine we compute the values of temperature and concentration at intermediate mesh points when given the values at the two extreme mesh points. We replace the values at the mesh point to the left of the evaporative boundary by those at the evaporative boundary point, before solving for the intermediate points. This can be done without destroying any useful information since that mesh point is no longer used in the computations. The subroutine TRIST does not depend upon equal spacing or any regular spacing and therefore can accommodate this usage.

6. Convergence

The convergence problem is the crux of the program. Oscillation tends to cause the needed quantities to overflow. Thus, tests must be made on all the quantities to contain them within reasonable bounds. The subroutine MOTON is used to check the monotonicity of these consecutive points. In addition, the temperature at the evaporative boundary is necessarily less than the temperature at the freezing boundary. This condition is always imposed in the program.

In addition, the solution for the solidification temperature and freezing boundary derivative (especially the latter) involves very rapidly changing quantities. More iterations should, therefore, be expended in this part of the program. Fewer iterations are needed for determining the evaporative boundary, and the temperature and concentration at that boundary. The program allows five iterations in the former for each of the latter. The number of iterations of the latter is used in a manner analogous to that described in Ref. 3.

An input quantity NIT (usually a multiple of 4) gives the maximum number of iterations. When NIT/2 iterations occur and convergence is not reached, the time step size is halved. This process is continued until either convergence is attained or the minimum step allowed by the program has been iterated NIT + 1 times. In this case the program may stop or continue on using the nonconverged quantities. Very often these quantities are sufficiently smooth so that convergence will occur on the next interval and the program gives satisfactory results.

However, if the program proceeds with the minimum step and the maximum number of iterations, the results may be spurious. In case of overflow, there is no doubt of it. Otherwise the user must look at results to decide whether he finds them reasonable.

7. Eutectic Temperature

When the interface temperature T_i reaches the eutectic temperature T_u, the program is changed so that interface temperature from then on remains at T_u. The rate of change of the boundary position is still determined from Eq. 49g on page 16 of Ref. 3. This leads to a rapid growth in the interface boundary.

C. Variable Parameter Program Modification

The original evaporative solidification program as well as its predecessors assumed that all the physical parameters were constant. Recognizing that this assumption is often a poor model of the real situation, we introduced variable parameters as

functions of melt temperature, or solute concentration, or both. As an initial effort in this direction, we limited the arbitrary functions to linear ones in the absence of any better known functional forms. The basic program logic for the linear approach would not change if non-linear terms are introduced in the future.

The specific heat of the solute C_u or of the solvent C_v are assumed to be linear functions of temperatures T only (Ref. 8):

$$C_u = C_{uo} + C_{uT} \cdot T \text{ and } C_v = C_{vo} + C_{vT} \cdot T$$

The density of the solute, ρ_u, and of the solvent, ρ_v, are also assumed to be linear functions of temperature above:

$$\rho_u = \rho_{uo} + \rho_{uT} \cdot T \text{ and } \rho_v = \rho_{vo} + \rho_{vT} \cdot T$$

The mass diffusion coefficients for the solid D_s is assumed to be a linear function of both concentration and temperature:

$$D_s = D_{sc} + D_{sc} \cdot C_s + D_{sT} \cdot T \cdot$$

The mass diffusion coefficient for the liquid D_ℓ is similarly defined:

$$D_\ell = D_{\ell c} + D_{\ell c} \cdot C_\ell + D_{\ell T} \cdot T$$

The thermal conductivity of the solid k_{su}, k_{sv} and of the liquid $k_{\ell u}$, $k_{\ell v}$ for solute and solvent, respectively, are assumed to be linear functions of temperature:

$$k_{su} = k_{suo} + k_{suT} \cdot T,\ k_{sv} = k_{svo} + k_{svT} \cdot T,\ k_{\ell u} = k_{\ell uo} + k_{\ell uT} \cdot T,\ k_{\ell v} = k_{\ell vo} + k_{\ell uT} \cdot T.$$

The thermal diffusion coefficients a_ℓ and a_s are determined from the equation $a_\ell^2 = k_\ell / \rho c$ and $a_s^2 = k_s / \rho c$, where $k_\ell = c_\ell k_{\ell u} + (1-c_\ell) \cdot k_{\ell v}$ and $k_s = c_s k_{su} + (1-c_s) k_{sv}$, and ρ and c are obtained from ρ_u, ρ_v and c_u and c_v respectively. Thus $\rho = \rho_u c + \rho_v (1-c)$ using the value of concentration C_ℓ for liquid, or C_s for solid. Similarly $c = c_u C + c_v (1-C)$ (Ref. 9) using the value of concentration C_ℓ for liquid or C_s for solid.

With these changes in physical parameters certain changes in program follow. In the original programs a subroutine TRIST was used to determine the concentration or temperature distribution at the new time $t + \Delta t$, given the values at time t and the values for the extreme points at $t + \Delta t$. This assumed a constant diffusion coefficient on either side of solid-liquid interface. With a variable diffusion coefficient the programming gains by the use of a subroutine are lost and the four uses were converted to four separate sets of instructions within the main program.

The effect of including functions of concentration and temperature instead of constants make the problem of convergence more difficult. Thus more iterations or smaller time intervals are required to bring out convergent results.

D. Single Crystal Growth Program

The computer program for crystal growth is a variant of the non-evaporative solidification program with a number of basic modifications. Instead of the three options for surface temperature, only the linear surface temperature, is provided. The conditions at the solid-liquid interface are changed by assuming only the equation for the redistribution of temperature at the moving boundary and replacing the one on concentration by assuming a constant derivative for the moving boundary. This simplifies the interface problem because it leaves only one unknown, the interface temperature. The two conditions of linear surface temperature and linear varying interface boundary simulate the conditions of crystal growth, the constant temperature gradient about the linear varying interface boundary.

The single crystal growth model is shown in Fig. 2. The computer program for this model assumes a constant temperature gradient and a constant (solid-liquid) interface velocity. This program is a variant of the linear surface temperature program developed in 1972 under our contract NAS 8-27891 (Ref. 3). In this program, the constant (solid-liquid) interface boundary velocity replaces one of the equations involving the interface boundary derivatives. This simplifies the basic iteration problem because now only the interface temperature must be obtained in a manner consistent with heat and mass diffusion equations. The linear surface temperature propagates a nearly linear temperature profile at the interface which, combined with the constant growth velocity, gives a nearly constant temperature gradient about the solid-liquid interface boundary.

Tables 1 and 2 indicate the insensitivity of the evaporation boundary and its temperature to grid spacing, provided that the spacing is always larger than the evaporation boundary point. Tables 3 and 4 involve solidification boundary and show that the temperature is insensitive to DELX but that the solidification boundary is quite sensitive to the choice of DELX. Thus, it is important to use DELX sufficiently small so that the solidification boundary movement is fully exhibited and not stunted by a large grid spacing relative to which the boundary size is small. The spacing affects the evaluation of the first and second temperature partial derivatives with time which are larger in absolute values for smaller spacings, due to more rapid temperature changes near the boundaries.

The figures (Figs. 3-5), prepared from the computed results in Tables 1-4, indicate the superiority of unequal over equal grid spacing. For DELX = 0.01 cm, where the spacing is coarse, little difference is found in the temperature distribution. For DELX = 0.001 cm, there is greater difference between the two because the equal spacing has limited the semi-infinite body to 0.027 cm and fixes the temperature at the end point to 970°C, thus not allowing the temperature to decline as rapidly as it should. For DELX = 0.0001 cm, the equal spacing method could not work at all because 0.0027 cm is too small a range to define a semi-infinite body even for the small time constants under consideration.

Fig. 4 (grid spacing DELX = 0.001), shows wide disparity between equal and unequal spacing whereas Fig. 3 (DELX = 0.01) shows good agreement. The smaller DELX needs more points to simulate the semi-infinite, one dimensional case and when restricted to IX = 28, fails to allow temperature away from the evaporating surface to decline rapidly because it is artificially pegged at x = 0.028

1. Initial conditions:

   liquid conc = c_o

   temperature = T_o

2. Growth conditions:

   Constant growth velocity = YD
   Constant temperature gradient = G
   Constant hot side temperature = T_0
   Constant cold side temperature = T_1
   Constant length of intermediate temperature of gradient = ZL
   Curved liquidus and solidus

3. Wanted:

   Concentration profiles, Ge or Si crystals.

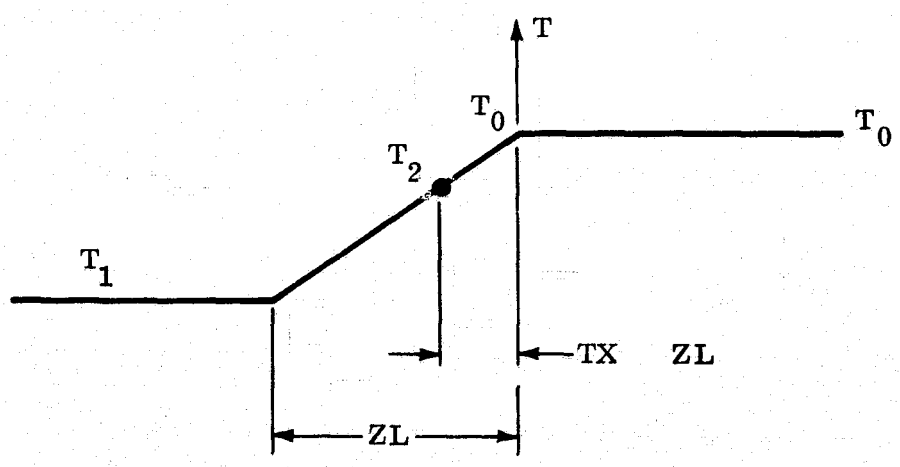

Fig. 2 Single Crystal Growth Model

Table 1. Variation of Temperature (^{o}C) at Evaporative Boundary for Various Computation Schemes

Scheme	I	II	III	IV	V
Grid Spacing	0.01 equal	0.01 unequal	0.001 equal	0.001 unequal	0.0001 cm unequal
time, ms					
0.2	966.5	966.5	966.5	966.5	966.5
0.6	959.4	959.4	959.4	959.4	959.5
1.4	945.7	945.7	945.7	945.7	945.8
1.8	938.9	938.9	938.9	938.9	939.0
2.0	935.5	935.5	935.5	935.5	935.6
2.05	934.7	934.7	934.7	934.7	N.C.
2.075	934.2	934.2	934.2	934.2	N.C.
2.0875	934.0	934.0	934.0	934.0	N.C.
2.09375	933.9	933.9	933.9	933.9	N.C.
2.1	933.8	933.8	933.8	933.8	933.9
2.1125	933.6	933.6	933.6	933.6	933.7*
2.1375	933.2	933.2	933.2	933.2	933.3*
2.1875	932.4	932.4	932.4	932.4*	932.5*
2.2875	930.8	930.8	930.8	930.8*	930.9*
2.4875	927.7	927.7	927.2	927.7*	927.7*
2.8875	921.5	921.5	921.5	921.5*	921.5*
3.6875	909.3	909.3	909.3	909.3*	909.3*
5.2875	885.8	885.8	885.8		

*Hand interpolations
N.C. not computed

Table 2. Variation of Position (μm) of Evaporative Boundary With Time for Various Computation Schemes

Scheme	I	II	III	IV	V
Grid Spacing	0.01 equal	0.01 unequal	0.001 equal	0.001 unequal	0.0001 cm unequal
time, ms					
0.2	0.122	0.122	0.122	0.122	0.122
0.6	0.351	0.351	0.351	0.351	0.351
1.4	0.752	0.752	0.752	0.752	0.752
1.8	0.927	0.927	0.927	0.927	0.928
2.0	1.009	1.009	1.009	1.009	1.010
2.05	1.029	1.029	1.029	1.029	N.C.
2.075	1.039	1.039	1.039	1.039	N.C.
2.0875	1.044	1.044	1.044	1.044	N.C.
2.09375	1.046	1.046	1.047	1.047	N.C.
2.1	1.047	1.047	1.047	1.047	1.050
2.1875	1.048	1.048	1.048	1.048*	1.052
2.2875	1.049	1.049	1.049	1.048*	1.053
2.4875	1.051	1.051	1.051	1.050*	1.055
2.8875	1.055	1.055	1.055	1.054*	1.059
3.6875	1.061	1.061	1.062	1.061	1.066
5.2875	1.072	1.072	1.072	-	-

*Hand interpolations
N.C. not computed

Table 3. Variation of Position (μm) of Solid-Liquid Interface

Scheme	I	II	III	IV	V
Grid Spacing	0.01 equal	0.01 unequal	0.001 equal	0.001 unequal	0.0001 cm unequal
time, ms					
0.21	0.205	0.204	0.109	0.109	0.106
0.24875	0.211	0.211	0.179	0.180	0.408
0.28875	0.229	0.229	0.350	0.350*	1.03
0.36875	0.283	0.283	0.866	0.860*	2.76
0.52875	0.429	0.429	2.291	N.C.	N.C.

Table 4. Variation of Temperature (^{o}C) at Solid-Liquid Interface

Scheme	I	II	III	IV	V
Grid Spacing	0.01 equal	0.01 unequal	0.001 equal	0.001 unequal	0.0001 cm unequal
time, ms					
0.21	933.8	933.8	933.8	933.8	933.9
0.24875	927.7	927.7	927.7	927.7*	927.9*
0.28875	924.5	921.4	921.5	921.4*	921.6*
0.36875	909.3	909.3	909.3	909.3*	909.4*
0.52875	885.8	885.8	885.8		

*Hand interpolations
N.C. not computed

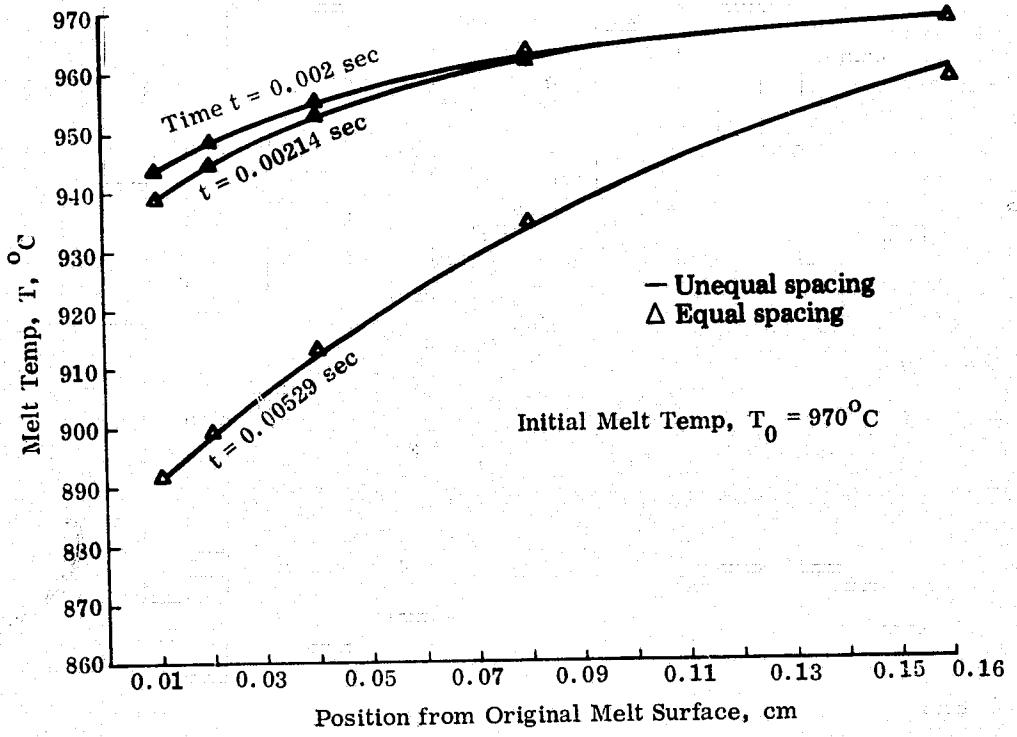

Fig. 3 Computed Temperature Distribution in Semi-Infinite Body at Different Times, t (initial grid spacing = 0.01 cm)

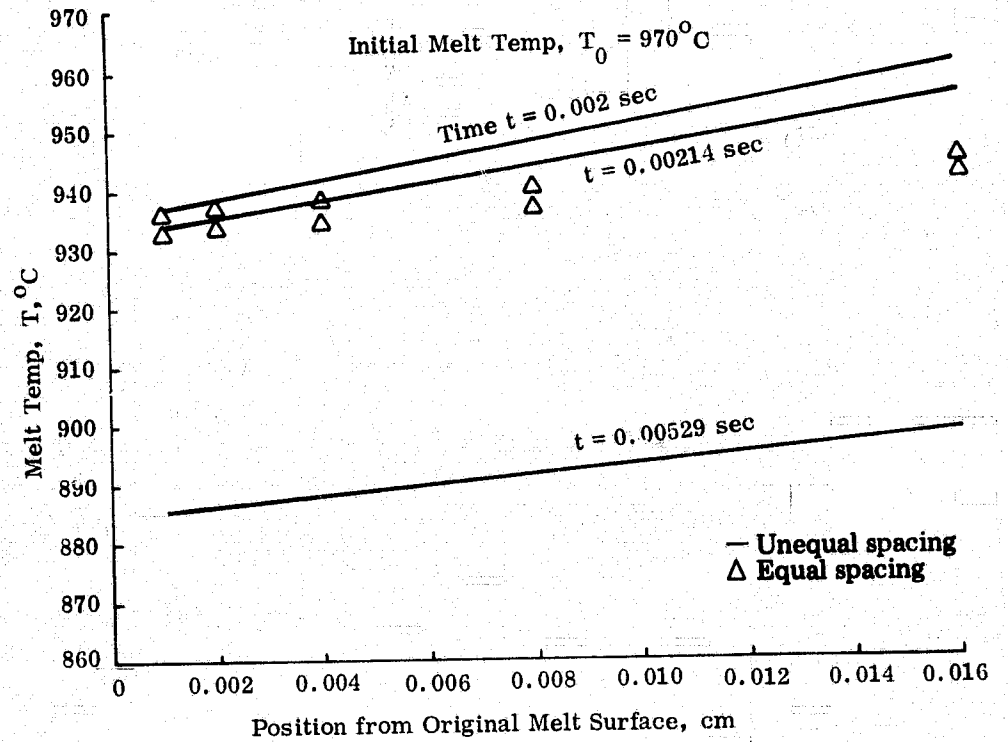

Fig. 4 Computed Temperature Distribution in the Semi-Infinite Body at Different Times, t (initial grid spacing = 0.001 cm)

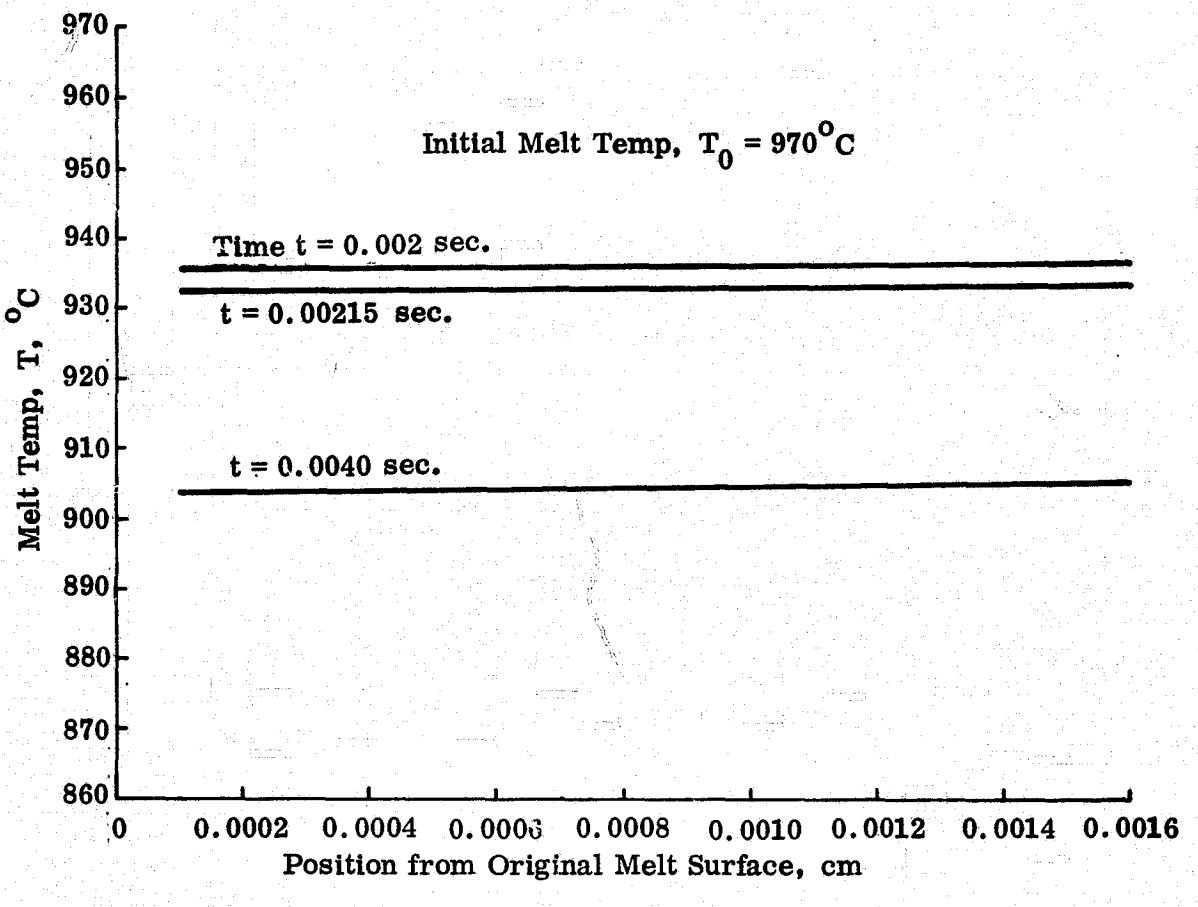

Fig. 5 Computed Temperature Distribution in Semi-Infinite Body at Different Times, t (initial grid spacing = 0.0001 cm)

cm to 970°C. The unequal spacing needs but six points to give equivalent extension and, when given 10 or 11 points, can adequately span a sufficient distance to simulate semi-infinity. At smaller DELX (0.0001) one cannot even attempt to use equal spacing without modifying the behavior at the last mesh point. For unequal spacing, 16 points will adequately represent the semi-infinite body for the times under consideration.

E. Programming Details

Some details of the programming techniques and a developed program are given in Appendices C and D.

3. COMBINED EVAPORATION AND SOLIDIFICATION TYPICAL COMPUTED RESULTS

We previously pointed out (Ref. 3) that evaporation always precedes freezing segregation and must be studied before meaningful performance and analysis of solidification experiments. This is particularly true since evaporation in the critical surface regions may cause the melt composition to be drastically altered within times as short as milliseconds. Thus the melting point and other thermophysical properties, nucleation characteristics, and critical velocity to avoid constitutional supercooling of the surface region may be completely unexpected (Ref. 3).

Evaporation, for example, may even introduce "anomalous" evaporative or constitutional melting (on cooling) or solidification (on heating) in simple binary melts. The final report to the previous contract completely discussed such newly predicted phenomena. The same report also summarized and presented some simple analytic equations for predicting the kinetics of segregation due to surface evaporation.

However, the study of combined evaporation and solidification was not undertaken under the previous contract. Nor, to our knowledge, has it been done by any other worker in the field in a systematic manner. Therefore, it was an important objective of this contract to study such a combined phenomenon.

Specifically, we have set up the necessary differential equations to include the phenomenon of evaporation in our previously developed, unidirectional solidification model. New computer logics have been devised and computer programs prepared and debugged. These work areas have been described in a previous section of this report. In this section, we present only some typical computed results on combined evaporation and solidification.

A. A Simple Example

For our first example we computed results for the semi-infinite Ge-Sb system having an eutectic temperature of 590°. These results, given in Table 5, show that for a 0.10% alloy of Sb in Ge initially at 970°C, directional solidification, from surface cooling through radiation and evaporation, begins shortly before 2.1 ms, with an interfacial temperature of 934°C and with the evaporation boundary also at 934°C, but located at only 0.105 μm from the initial melt surface. At first, the evaporating surface is losing material rapidly at the rate of over 50 μm/sec, due mostly to the loss of Sb. After a few milliseconds, the solid surface is practically all Ge, with a surface receding rate of less than 1 μm/sec. After some 30 ms, the evaporating boundary is practically stationary. These results agree with rough computations based on the evaporating rates of Ge and Sb at 700-940°C.

The rate of solidification increases with time. Initially, the rate is very low, less than 0.054 μm/sec on the average in the first 2.1 ms. This growth rate increases from 2 to 12 ms due to increasing temperature gradient in the solid. A temporary maximum growth rate of over 0.5 μm/sec is reached at 12 ms, coinciding

Table 5. Evaporation and Solidification of 0.1% Sb in Ge Alloy Initially at 970°C

Time, t, ms	Position of Evaporation Boundary y, μ m	Temp at Evaporation Boundary T_y, °C	Position of Solid Boundary z, μ m	Aver Growth Rate μm/sec	Temp at Solid Boundary T_i, °C	Note
2.1	0.1050	933.9	0.109	54	933.9	Beginning of Solidification
4.0	0.1067	904.7	1.96	490	904.8	
8.0	0.1087	847.2	19.19	2,400	849.9	
12	0.1096	794.3	39.79	1,990	806.6	
16	0.1099	745.1	48.53	3,030	750.4	
20	0.1101	698.9	49.92	2,500	704.9	
24	0.1101	655.2	51.35	2,140	661.0	
28	0.1102	613.5	52.83	1,890	619.5	
32	0.1102	573.5	65.24	2,040	590.0	Note Large Change in Solid Boundary
36	0.1102	534.9	159.5	4,430	590.0	
40	0.1102	497.5	272.2	6,810	590.0	

with a maximum solid temperature gradient. A temporary minimum growth rate is reached shortly before reaching eutectic temperature of 590°C when the solid-liquid interface is sufficiently inside the origin melt surface, and, hence, the effect of heat loss through surface radiation is relatively small. Right after reaching the eutectic solidification stage, the growth rate increases rapidly because there is then no longer the mechanism of heat loss through sensible heat changes (since the temperature of the eutectic solidification is fixed at 590°C). For still longer solidification periods, we expect the growth rate to decrease again, because of the leveling of the solid temperature gradient. (Part of the results are shown in Table 5).

B. Effect of Melt Composition

This example shows clearly the complicated process of solidification in binary alloys, and also the intricate interactions between surface evaporation, internal solidification and heat or mass transfer. Simple solidification theories and approximate solidification equations may, therefore, not be accurate in evaluating the critical initial phase of nucleation and freezing. Specifically, predicting whether constitutional supercooling occurs or whether single crystals will grow may require such numerical computer programs as we have developed under this contract.

To study the effect of melt composition on combined evaporation-solidification, we made comparative runs for the same Ge-Sb system at the same initial temperature of 970°C, but with the Sb concentrations originally at 0.01, 0.001, and 0.0001%. At short times, $t \cong 2.1$ ms, the temperature at the evaporating boundary for the four initial Sb concentrations is fairly constant at 934.0 ± 1.3°C. The position of the evaporation boundary, y, however, decreases proportionately with decreasing Sb concentration except at the highest Sb concentration. For example, decreasing Sb from 0.1 to 0.01% reduces y by a factor of 20 (instead of 10) at 2.1 ms. After about 26 ms, the evaporation boundary is stabilized in position. The percentage difference in y between 2.1 ms and 26 ms decreases logarithmically with Sb concentration, from 5% at 0.1% Sb to 18% at 0.0001% Sb. These results again confirm the fact that evaporation of Ge-Sb alloys is mainly due to the loss of Sb.

All these Ge-Sb alloys, according to the computed results, begin to solidify eutectically within 32 ms. Except for the 0.1% alloy, the interfacial temperature at any given time is independent of the initial Sb concentration. The 0.1% alloy has consistently higher interfacial temperatures than the more dilute alloys, by as much as 17°C at intermediate times. The position of the solidification boundary at a given time is consistently smaller for the 0.1% alloy than for the more dilute alloys. The difference in this position increases, as expected, with the time.

These and other results on combined evaporation-solidification have given us some unexpected data that can be summarized as follows:

1. Surface evaporation, internal solidification, and mass or heat transfer interact in complicated manners. Individual treatment of only one aspect may not be sufficient.

2. The rate of evaporation is very appreciable at first, but rapidly (in milliseconds) becomes negligible.

3. Evaporation leaves permanent and extremely large segregation effects that can radically affect melt undercooling and nucleation. The distance of the evaporation controlled layer is, however, too small (at least for Ge-Sb alloys) to be detected by the electron probe.

4. The rate of solidification does not monotonically increase or decrease, as predicted by simple, existing solidification theories; it fluctuates up and down.

C. Combined Effects of Liquid Mass Transfer and Melt Composition

The segregation effects during solidification in weightless melts are at least partly due to changing effective liquid mass transfer coefficient (i.e., solute transport rate across unit concentration gradient in the liquid), D_ℓ. Various Skylab experiments have shown D_ℓ to decrease by up to 50 times over ground control experiments, (Ref. 2), depending on the sample shape, size, temperature, composition, type of experiment, and the like. Our computer program allows us to readily simulate the evaporation-solidification behavior during the single crystal growth under varying D_ℓ. The computed results may, therefore, even give us some insight into the effects of sample shape, size, temperature, composition, and type of experiments on weightless solidification.

Hence, we have made nine systematic computer runs by simultaneously varying the initial antimony concentration c_o in germanium single crystal over three decades from 0.01 to 0.0001 and D_ℓ also over three decades from 10^{-4} to 10^{-6} cm^2/sec). The computed results are given in Tables 6 through 9.

As shown in Table 6, the solidification velocity $\dot{z}$ is predominantly determined by D_ℓ. Decreasing D_ℓ by one or two orders of magnitude reduces $\dot{z}$ by the same amount. In fact, the solidification velocity $\dot{z}$ can be approximated by $\dot{z} \approx 2000\ D_\ell$ during the time interval 0.002 to 0.01 second. Hence, the solidification velocity in Skylab samples probably was much smaller, by up to 50 times also, during some of the solidification processes. Table 6 further shows that during the initial and final stages of solidification, the solidification velocities are further reduced by mechanisms other than those related to D_ℓ. Specifically, in the initial stages of solidification, (for time $t \leq 0.001$ second), the velocity is reduced about 40 times at initial concentration $c_o = 0.01$ for all values of D_ℓ and at higher concentrations by about 35 times at $D_\ell = 10^{-6}$ cm^2/sec. During the later stages of solidification ($t > 0.02$ second), the solidification velocity is reduced by about twice at $D_\ell = 10^{-4}$ cm^2/sec.

Table 6 shows that the receding rate of the evaporating (gas-solid) boundary $\dot{y}$ decreases constantly with the evaporation-solidification time t, more so at high initial antimony concentrations c_o than at low concentrations. The decreases in $\dot{y}$, for example, between 0.001 and 0.01 second are, respectively, 160, 6, and 6 times at $c_o = 0.01$, 0.001, and 0.0001. A decrease in D_ℓ also reduces $\dot{y}$, by about one order of magnitude when c_o is reduced from 0.01 to 0.001 during the early stages of the evaporation-solidification process ($t \leq 0.002$ second), but with no decrease when c_o is further reduced from 0.001 to 0.0001, or when t exceeds 0.002 second. Thus, the evaporation behaviors of Skylab samples were also probably markedly different from those of ground samples.

A summary of some findings on the position of the solidification boundary, z, (Table 6) is given below.

Table 6. Variation of $\dot{z}$ With D_ℓ, c_o, and

c_o		0.01	0.01	0.01	0.001	0.001	
D_ℓ	cm^2/sec	10^{-4}	10^{-5}	10^{-6}	10^{-4}	10^{-5}	
	t, sec						
$\dot{z}$	0.001	5.0×10^{-3}	5.0×10^{-3}	5.0×10^{-3}	1.7×10^{-1}	1.8×10^{-2}	5.
cm/sec	0.002	1.5×10^{-1}	1.6×10^{-2}	2.4×10^{-3}	1.8×10^{-1}	1.8×10^{-2}	2.
	0.005	2.1×10^{-1}	1.7×10^{-2}	2.0×10^{-3}	2.7×10^{-1}	1.8×10^{-2}	2.
	0.01	1.8×10^{-1}	1.8×10^{-2}	1.9×10^{-3}	1.9×10^{-1}	1.8×10^{-2}	2.
	0.02	7.8×10^{-2}	1.8×10^{-2}	1.9×10^{-3}	7.8×10^{-2}	1.8×10^{-2}	1.

Table 7. Variation of $\dot{y}$ With D_ℓ, c_o, and

c_o		0.01	0.01	0.01	0.001	0.001	0.
D_ℓ	cm^2/sec	10^{-4}	10^{-5}	10^{-6}	10^{-4}	10^{-5}	
	t, sec						
$\dot{y}$	0.001	5.0×10^{-4}	5.0×10^{-4}	5.0×10^{-4}	8.5×10^{-6}	8.5×10^{-6}	8.
cm/sec	0.002	1.7×10^{-5}	1.8×10^{-5}	1.8×10^{-5}	6.9×10^{-6}	6.7×10^{-6}	7.
	0.005	9.2×10^{-6}	9.6×10^{-6}	1.0×10^{-5}	3.6×10^{-6}	3.6×10^{-6}	3.
	0.01	3.2×10^{-6}	3.2×10^{-6}	3.6×10^{-6}	1.2×10^{-6}	1.2×10^{-6}	1.
	0.02	3.1×10^{-7}	3.2×10^{-7}	3.7×10^{-7}	1.2×10^{-7}	1.2×10^{-7}	1.

Table 6. Variation of $\dot{z}$ With D_ℓ, c_o, and t

01	0.001	0.001	0.001	0.0001	0.0001	0.0001
$^{-6}$	10^{-4}	10^{-5}	10^{-6}	10^{-4}	10^{-5}	10^{-6}
$\times 10^{-3}$	1.7×10^{-1}	1.8×10^{-2}	5.7×10^{-3}	1.8×10^{-1}	1.9×10^{-2}	6.2×10^{-3}
$\times 10^{-3}$	1.8×10^{-1}	1.8×10^{-2}	2.5×10^{-3}	1.8×10^{-1}	1.8×10^{-2}	2.5×10^{-3}
$\times 10^{-3}$	2.7×10^{-1}	1.8×10^{-2}	2.1×10^{-3}	2.8×10^{-1}	1.8×10^{-2}	2.1×10^{-3}
$\times 10^{-3}$	1.9×10^{-1}	1.8×10^{-2}	2.0×10^{-3}	2.1×10^{-1}	1.8×10^{-2}	2.0×10^{-3}
$\times 10^{-3}$	7.8×10^{-2}	1.8×10^{-2}	1.9×10^{-3}	7.9×10^{-2}	1.8×10^{-2}	1.9×10^{-3}

Table 7. Variation of $\dot{y}$ With D_ℓ, c_o, and t

01	0.001	0.001	0.001	0.0001	0.0001	0.0001
$^{-6}$	10^{-4}	10^{-5}	10^{-6}	10^{-4}	10^{-5}	10^{-6}
$\times 10^{-4}$	8.5×10^{-6}	8.5×10^{-6}	8.5×10^{-6}	8.5×10^{-6}	8.5×10^{-6}	8.5×10^{-6}
$\times 10^{-5}$	6.9×10^{-6}	6.7×10^{-6}	7.1×10^{-6}	6.9×10^{-6}	6.7×10^{-6}	7.1×10^{-6}
$\times 10^{-5}$	3.6×10^{-6}	3.6×10^{-6}	3.9×10^{-6}	3.6×10^{-6}	3.6×10^{-6}	3.9×10^{-6}
$\times 10^{-6}$	1.2×10^{-6}	1.2×10^{-6}	1.4×10^{-6}	1.2×10^{-6}	1.2×10^{-6}	1.4×10^{-6}
$\times 10^{-7}$	1.2×10^{-7}	1.2×10^{-7}	1.4×10^{-7}	1.2×10^{-7}	1.2×10^{-7}	1.4×10^{-7}

FOLDOUT FRAME 2

Table 8. Variation of z (cm) With D_ℓ, t, and c_o

c_o	0.01	0.01	0.01	0.001	0.001	0.001
D_ℓ	10^{-4}	10^{-5}	10^{-6}	10^{-4}	10^{-5}	10^{-6}
t, sec						
0.001	1.1×10^{-6}	1.1×10^{-6}	1.1×10^{-6}	1.1×10^{-5}	1.3×10^{-6}	4.8×10^{-7}
0.002	1.4×10^{-4}	1.7×10^{-5}	3.7×10^{-6}	1.8×10^{-4}	2.1×10^{-5}	3.7×10^{-6}
0.005	6.8×10^{-4}	6.6×10^{-5}	1.0×10^{-5}	7.9×10^{-4}	7.3×10^{-5}	1.0×10^{-5}
0.01	1.6×10^{-3}	$1.5 \text{ c } 10^{-4}$	2.0×10^{-5}	1.6×10^{-3}	1.6×10^{-4}	2.0×10^{-5}
0.02	2.6×10^{-3}	3.3×10^{-4}	3.9×10^{-5}	2.6×10^{-3}	3.4×10^{-4}	4.0×10^{-5}

Table 9. Effect of c_o, D_ℓ, and t on the Position of Evaporation E

c_o	0.01	0.01	0.01	0.001	0.001	0.001
D_ℓ	10^{-4}	10^{-5}	10^{-6}	10^{-4}	10^{-5}	10^{-6}
t, sec						
0.001	5.6×10^{-7}	5.6×10^{-7}	5.6×10^{-7}	5.1×10^{-8}	5.1×10^{-8}	5.1×10^{-8}
0.002	5.8×10^{-7}	5.8×10^{-7}	5.8×10^{-7}	5.8×10^{-8}	5.9×10^{-8}	5.9×10^{-8}
0.005	6.2×10^{-7}	6.2×10^{-7}	6.2×10^{-7}	7.4×10^{-8}	7.4×10^{-8}	7.5×10^{-8}
0.01	6.5×10^{-7}	6.5×10^{-7}	6.5×10^{-7}	8.4×10^{-8}	8.5×10^{-8}	8.7×10^{-8}
0.02	6.6×10^{-7}	6.6×10^{-7}	6.7×10^{-7}	8.9×10^{-8}	9.0×10^{-8}	9.2×10^{-8}

Table 8. Variation of z (cm) With D_ℓ, t, and c_o

	0.001	0.001	0.001	0.0001	0.0001	0.0001
	10^{-4}	10^{-5}	10^{-6}	10^{-4}	10^{-5}	10^{-5}
$.0^{-6}$	1.1×10^{-5}	1.3×10^{-6}	4.8×10^{-7}	1.1×10^{-5}	1.2×10^{-6}	4.0×10^{-7}
$.0^{-6}$	1.8×10^{-4}	2.1×10^{-5}	3.7×10^{-6}	1.9×10^{-4}	2.1×10^{-5}	3.6×10^{-6}
$.0^{-5}$	7.9×10^{-4}	7.3×10^{-5}	1.0×10^{-5}	8.0×10^{-4}	7.4×10^{-5}	1.0×10^{-5}
$.0^{-5}$	1.6×10^{-3}	1.6×10^{-4}	2.0×10^{-5}	1.7×10^{-3}	1.6×10^{-4}	2.0×10^{-5}
$.0^{-5}$	2.6×10^{-3}	3.4×10^{-4}	4.0×10^{-5}	2.6×10^{-3}	3.4×10^{-4}	4.0×10^{-5}

9. Effect of c_o, D_ℓ, and t on the Position of Evaporation Boundary, y (cm)

	0.001	0.001	0.001	0.0001	0.0001	0.0001
	10^{-4}	10^{-5}	10^{-6}	10^{-4}	10^{-5}	10^{-6}
10^{-7}	5.1×10^{-8}	5.1×10^{-8}	5.1×10^{-8}	6.0×10^{-9}	6.0×10^{-9}	6.0×10^{-9}
10^{-7}	5.8×10^{-8}	5.9×10^{-8}	5.9×10^{-8}	1.4×10^{-8}	1.5×10^{-8}	1.4×10^{-8}
10^{-7}	7.4×10^{-8}	7.4×10^{-8}	7.5×10^{-8}	2.9×10^{-8}	2.9×10^{-8}	3.0×10^{-8}
10^{-7}	8.4×10^{-8}	8.5×10^{-8}	8.7×10^{-8}	4.0×10^{-8}	4.0×10^{-8}	4.2×10^{-8}
10^{-7}	8.9×10^{-8}	9.0×10^{-8}	9.2×10^{-8}	4.4×10^{-8}	4.5×10^{-8}	4.8×10^{-8}

FOLDOUT FRAME 2

1. The position of the solidification boundary, z , increases with the evaporation-solidification time, t, but according to no apparently simple rules or equations, at least from t = 0.001 to 0.02 second. Within this time interval, each increasing time step (which is 2.0 or 2.5 times the previous time t) increases the z value by multiplication factors F of 20.1, 4.3, 2.2, and 1.6, respectively, from short to long t. (Fig. 6)

2. D_ℓ also exerts great influences on z (Fig. 6 and 7). Decreasing D_ℓ (due, for example, to low gravity) decreases z, by an average factor F of 8.4 per decade of decrease in D_ℓ . The average factor F is, however, greater for changing D_ℓ from 10^{-5} to 10^{-4} cm^2/sec (F = 8.8) than from 10^{-6} to 10^{-5} cm^2/sec (F = 7.9) as shown in Fig. 6 and Table 10.

3. The effect of D_ℓ on z depends very much on the evaporation-solidification time t. That is, D_ℓ and t strongly interact. Each decade increase in D_ℓ may increase z by as little as a multiplication factor F of 1.8 (at t = 0.001 second and D_ℓ from 10^{-6} to 10^{-5} cm^2/sec), or as much as 10.6 (at t = 0.005 second and D_ℓ from 10^{-5} to 10^{-4} cm^2/sec), as shown in Table 10 and Fig. 6

Table 10. Multiplication Factors F Due to Changing D_ℓ at Different t

t, sec	0.001	0.002	0.005	0.01	0.02	Average
D_ℓ change, cm^2/sec						
10^{-6} to 10^{-5}	1.8	5.4	7.1	7.8	8.5	7.9
10^{-5} to 10^{-4}	6.4	8.6	10.6	10.4	7.7	8.8
Average	4.1	7.0	8.9	9.1	8.1	8.4

4. There is a consistent trend of c_o on z also. This c_o effect on z is, however, minimal. Each decade increase in c_o increases z by only about 3%. (Fig. 8) These z increases are practically zero at small D_ℓ (10^{-6} and 10^{-5} cm^2/sec) and low concentrations (c_o = 0.0001).

5. The solidification velocity $\dot{z}$ changes with t in a manner strongly dependent on D_ℓ , not only in magnitude but in the shape of the $\dot{z}$-t curve (Fig. 9). Such results are not available from close-form equations or simple computer simulations.

Finding 4 indicates that it is impractical or impossible to duplicate or study the effect of zero gravity on z, the position of the solidification boundary, by simply varying the antimony concentration (c_o) in germanium. If this trend holds generally, one may conclude that a single composition is probably adequate for an entire binary system, for the study of zero gravity effects on z.

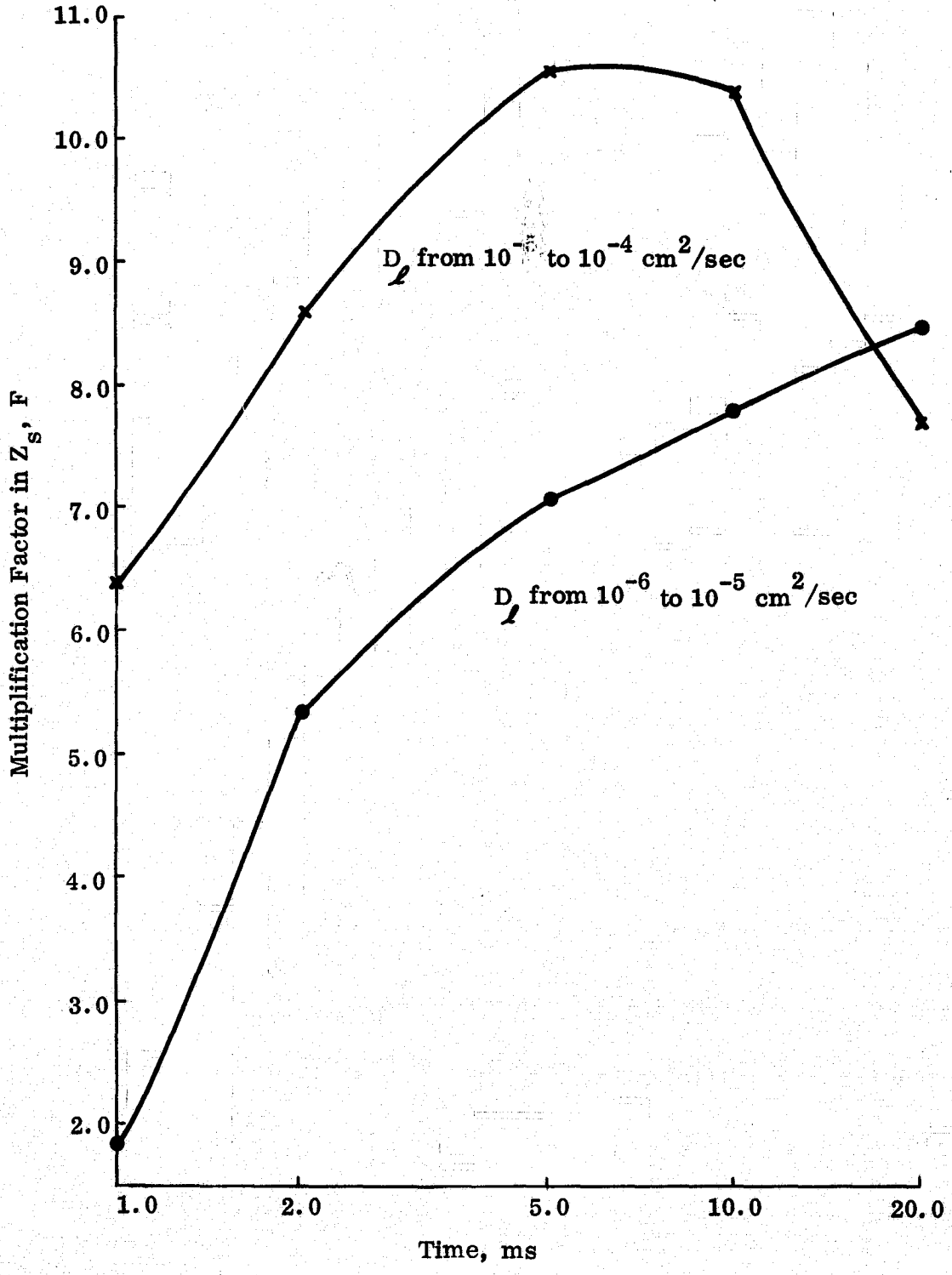

Fig. 6 Multiplication Factor for Crystal Length at Different Times for Two Decade-Changes in D_ℓ

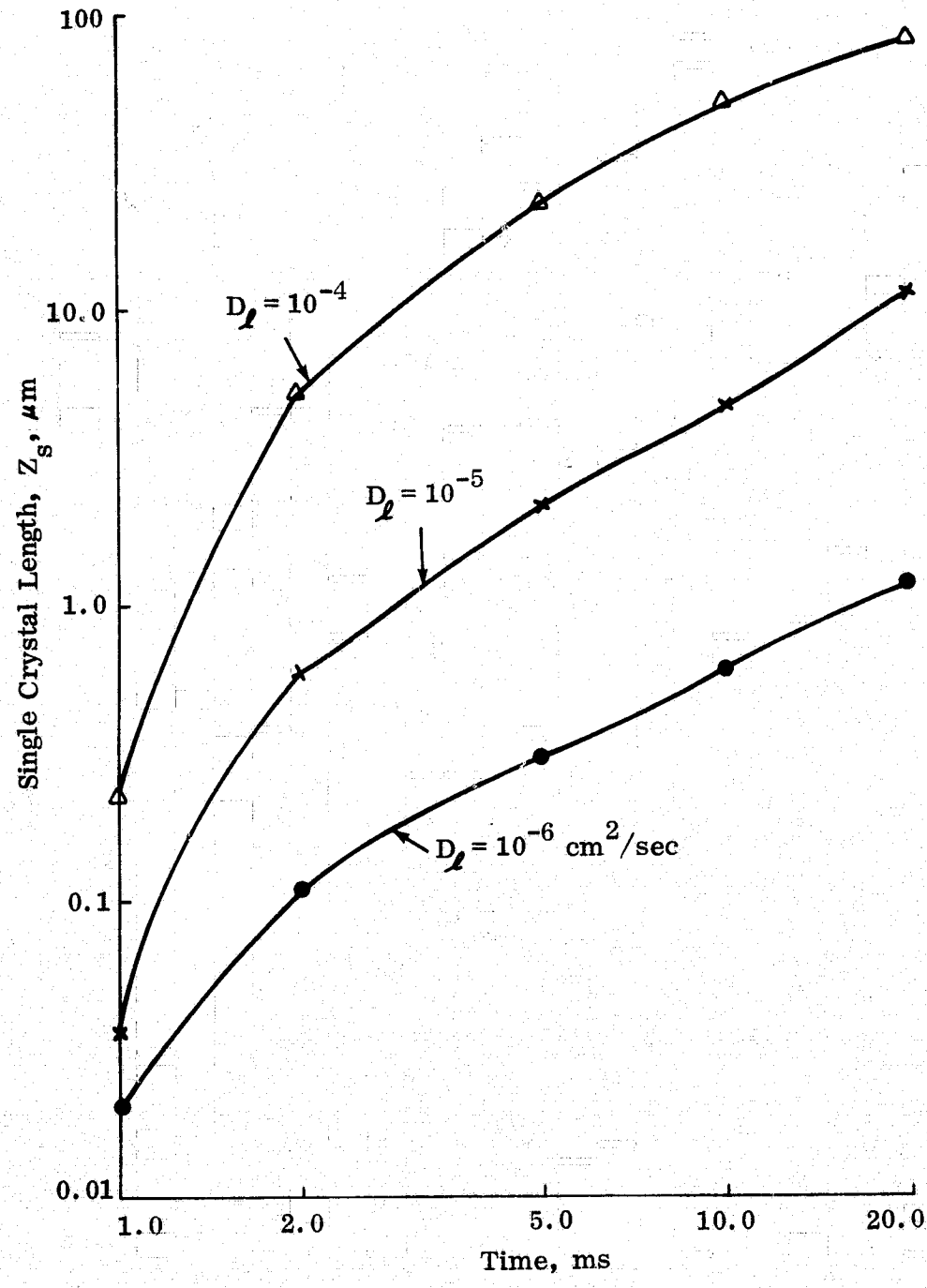

Fig. 7 Position of Solidification Boundary at Different Times for Various Liquid Mass Transfer Coefficients

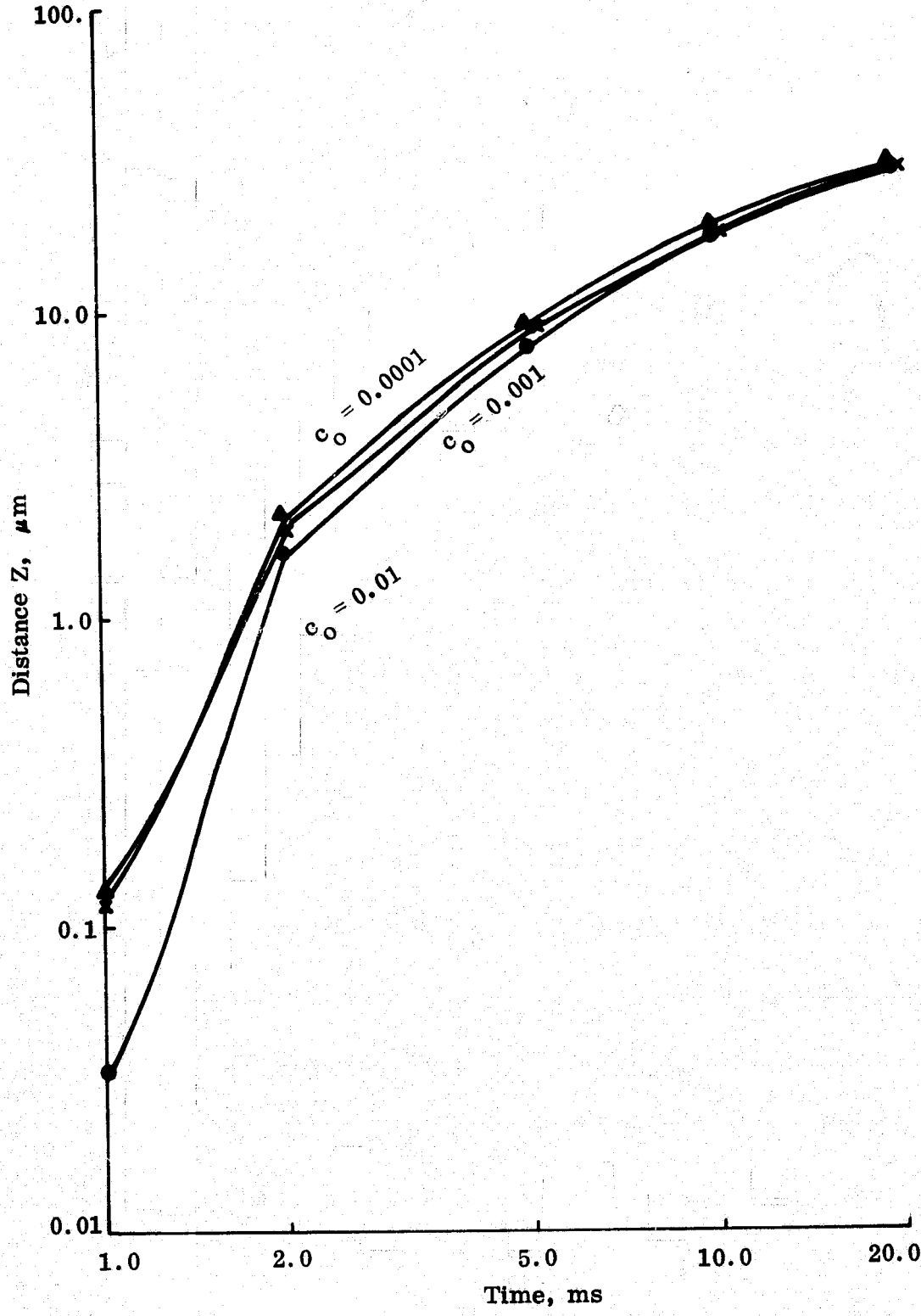

Fig. 8 Position of Solidification Boundary at Different Times for Various Initial Antimony Concentration in Ge

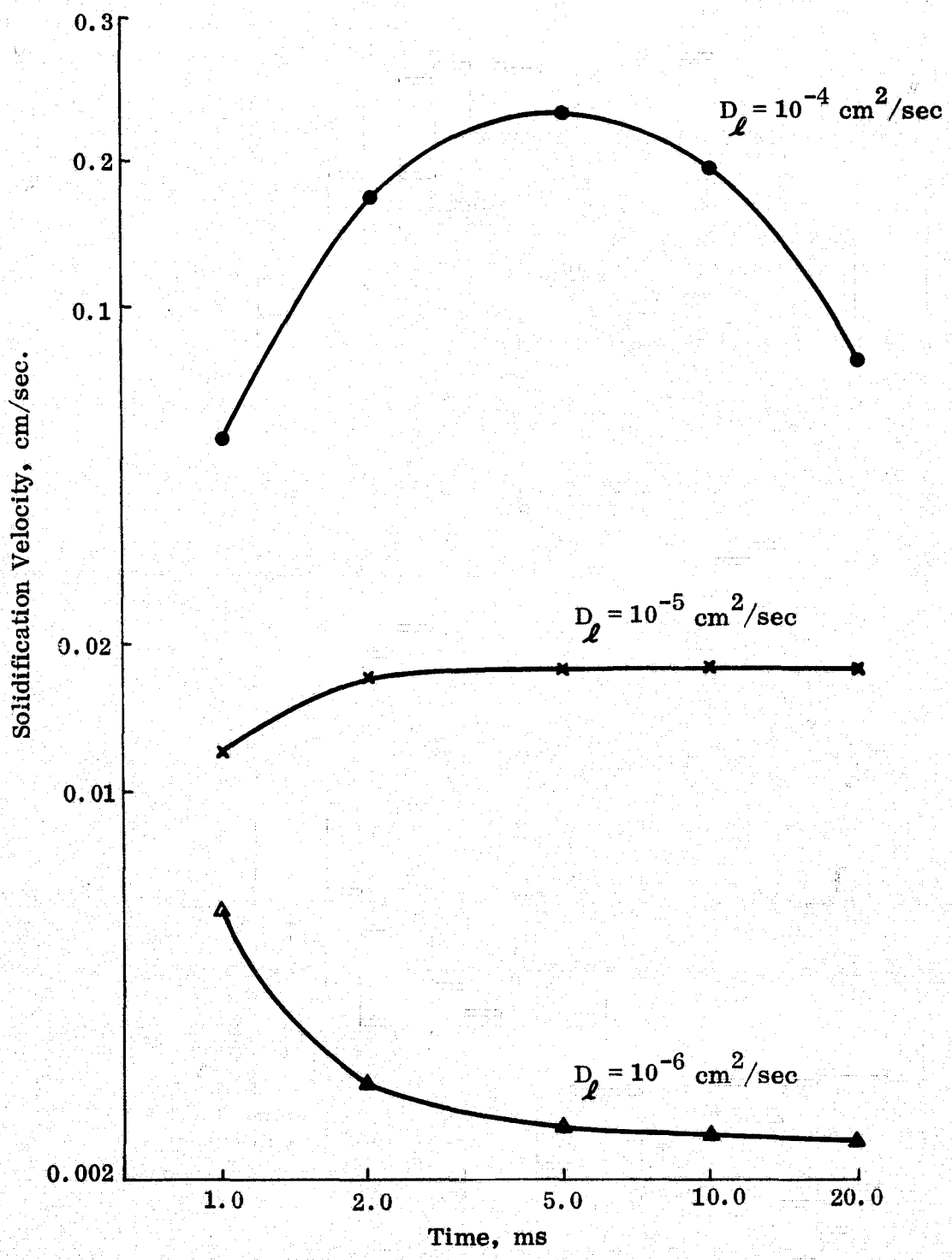

Fig. 9 Variation of Solidification Velocity With D_ℓ and t

Finding 3 suggests that an optimum time interval may exist (i.e., from t = 0.005 to 0.01 second) for the study of effects on z of zero gravity through changing D_ℓ, because of the large multiplication factors F in this time interval. Such study requires, however, submicron (depth) resolution techniques for sample characterization.

For example, the effect of zero gravity is shown to reduce the effective liquid mass transfer from 10^{-4} to 10^{-5} cm^2/sec (Ref. 10). Finding 3 thus suggests that zero-gravity effects related to this mass transfer will be most noticeable when the crystal lengths on ground-base and space-processed samples are compared at 5 to 10 ms after the initiation of cooling and solidification. Future space processing experiments may, therefore, be planned with this in mind, to maximize the chance of detecting and characterizing the generally subtle zero-gravity effects among the many inherent noises. (Ref. 3).

D. Summary of Combined Evaporation and Solidification

The work under this contract has accomplished the following:

1. Developed computer programs to study combined evaporation and solidification with surface evaporation and radiative cooling.

2. Confirmed the importance of evaporation, as pointed out in the final report of our last NASA contract (Ref. 3).

3. Using the developed computer programs, studied the individual effects of concentration on combined evaporation-solidification in the Sb-Ge system.

4. Further studied the combined effects of effective liquid mass transfer and melt composition on combined evaporation-solidification through systematic computer simulation.

5. Discovered the complicated interaction of melt composition c_o, liquid mass transfer coefficient D_ℓ, and cooling time t on evaporation-solidification.

6. Examined these new results in relation to possible zero-gravity effects and space processing.

Notice that the computer programs developed under this contract, while still limited to a unidirectional model, account for not only heat and mass transfer, but also for surface evaporation and radiative cooling. Some predicted results have been confirmed, and some other unexpected results were discovered. For example, it is shown that the solidification velocity does not necessarily change monotonically with the cooling time. In fact, the same velocity may increase or decrease with time, or reach maximum at an intermediate time, depending on D_ℓ. Also, D_ℓ markedly affects the position of the solidification boundary z, but not that of the evaporation boundary. On the other hand, increasing c_o affects the position of the evaporation boundary, but not that of the solidification boundary (at least for Ge-Sb alloys studied).

The discovery of a maximum effect of a given change in D_ℓ, as measured by z, is probably the most directly relevant to space processing. By utilizing this information, many future space processes can be systematically designed for maximum scientific return. Such designs should involve not only the sample configuration and size or furnace capability, but also sample characterization techniques. The results on the position of the evaporation boundary, y (see Table 9) have also been analyzed. Among the three studied parameters, D_ℓ, c_o, and t, c_o most influences y. Decreasing c_o by one decade from 0.01 and 0.001 reduces y by factors 8.5 and 2.6, respectively, as shown in Fig. 10. Increasing t always increases y, but at decreasing rates with increasing t. This time effect is most noticeable at low c_o (Fig. 6). D_ℓ, on the other hand, is unimportant on y, particularly at high D_ℓ values (Fig. 6).

The evaporation velocity, $\dot{y}$, decreases with increasing t and is reduced by 2-4 orders of magnitude within 20 ms, depending on c_o. There is also an interaction between c_o and t on $\dot{y}$. Thus, while a diffusion-controlled, somewhat steady-state condition is reached at low concentrations (c_o = 0.001 and 0.0001) within 1 ms, the same condition is not reached at a higher concentration (c_o = 0.01) after 2 ms (See Fig. 12).

Thus, while D_ℓ greatly affects the solidification boundary position, z (or single crystal length) or growth velocity $\dot{z}$ (Figs. 6, 7, 9), it has almost negligible effect on y (Fig. 11). This can be explained as follows: At reduced D_ℓ (such as in space), enhanced solute pile-up ahead of the solid-liquid interface causes lowering of the melting point and, hence, reduced solidification under given thermal conditions. Because at 970°C antimony evaporates seven to eight orders of magnitude faster than germanium, the solute depletion at the evaporating boundary is so rapid that even one or two orders of magnitude variations in D_ℓ change y only very slightly.

E. Additional computed results

Additional computed results for combined evaporation and solidification, and their uses in space processing, are given in Appendix E on an "Econotechnical Model of Capital Growth".

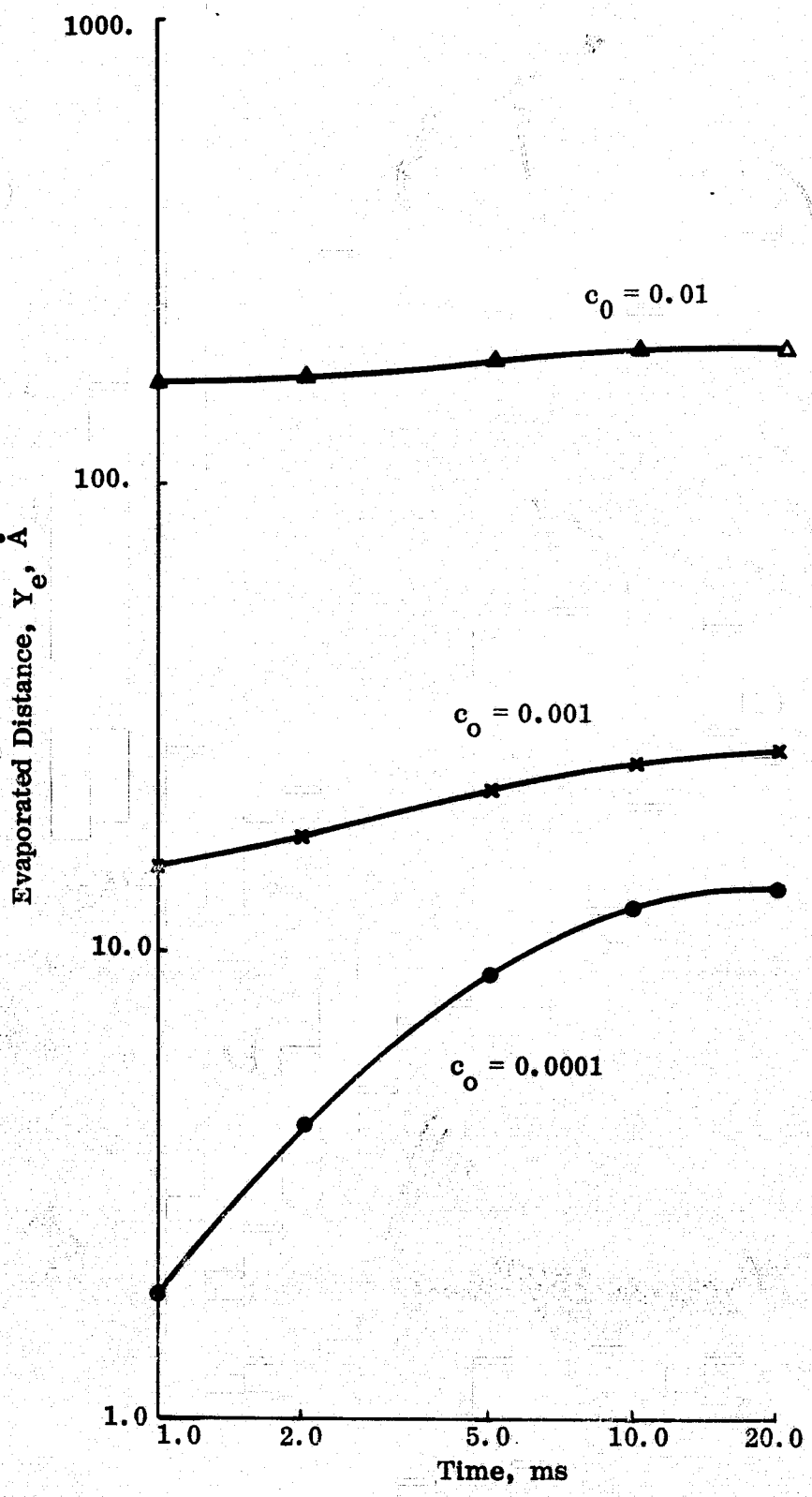

Fig. 10 Position of Evaporation Boundary at Different Times for Various Sb Concentrations in Ge

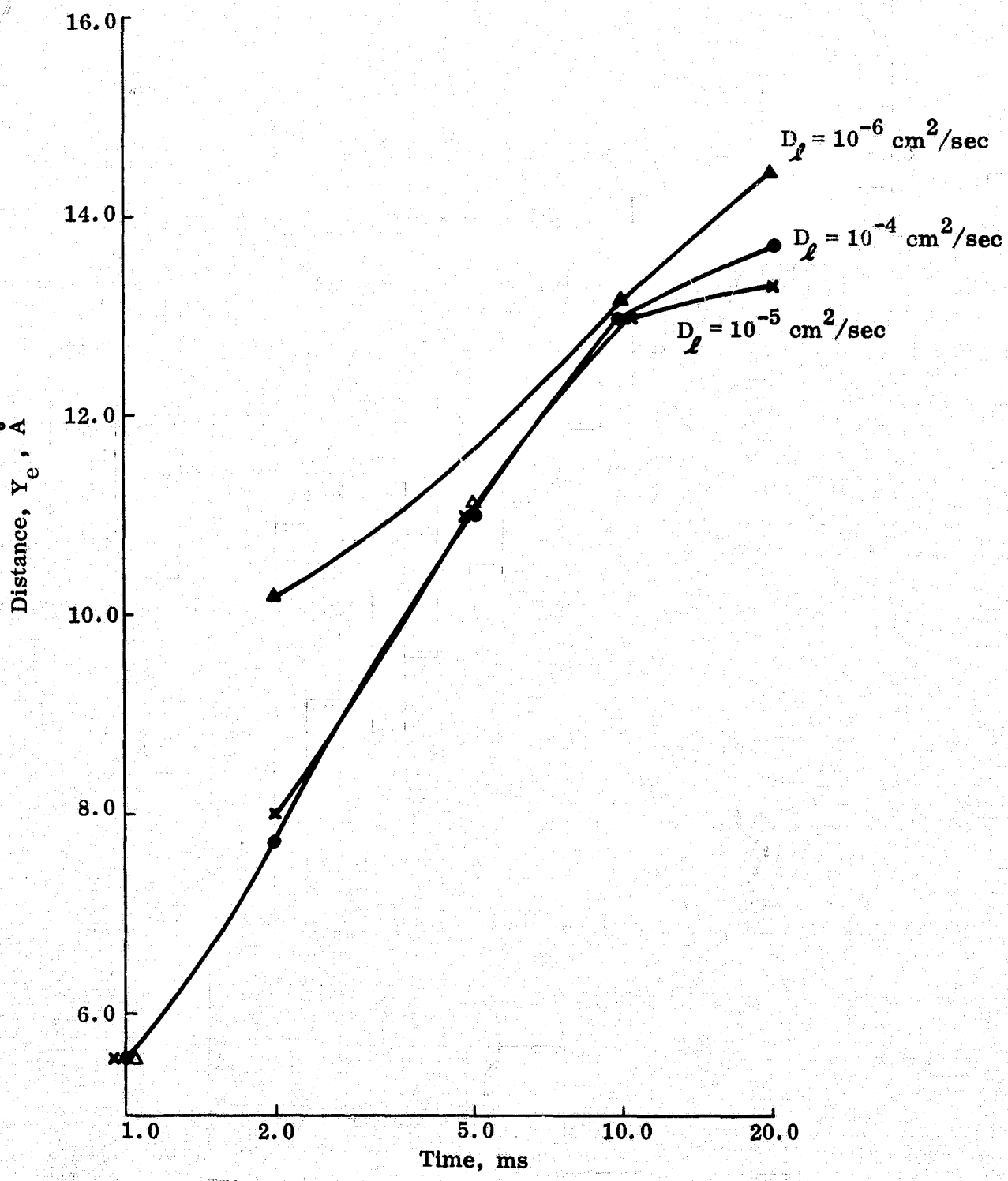

Fig. 11 Position of Evaporation Boundary at Different Times for Various Liquid Mass Transfer Coefficients

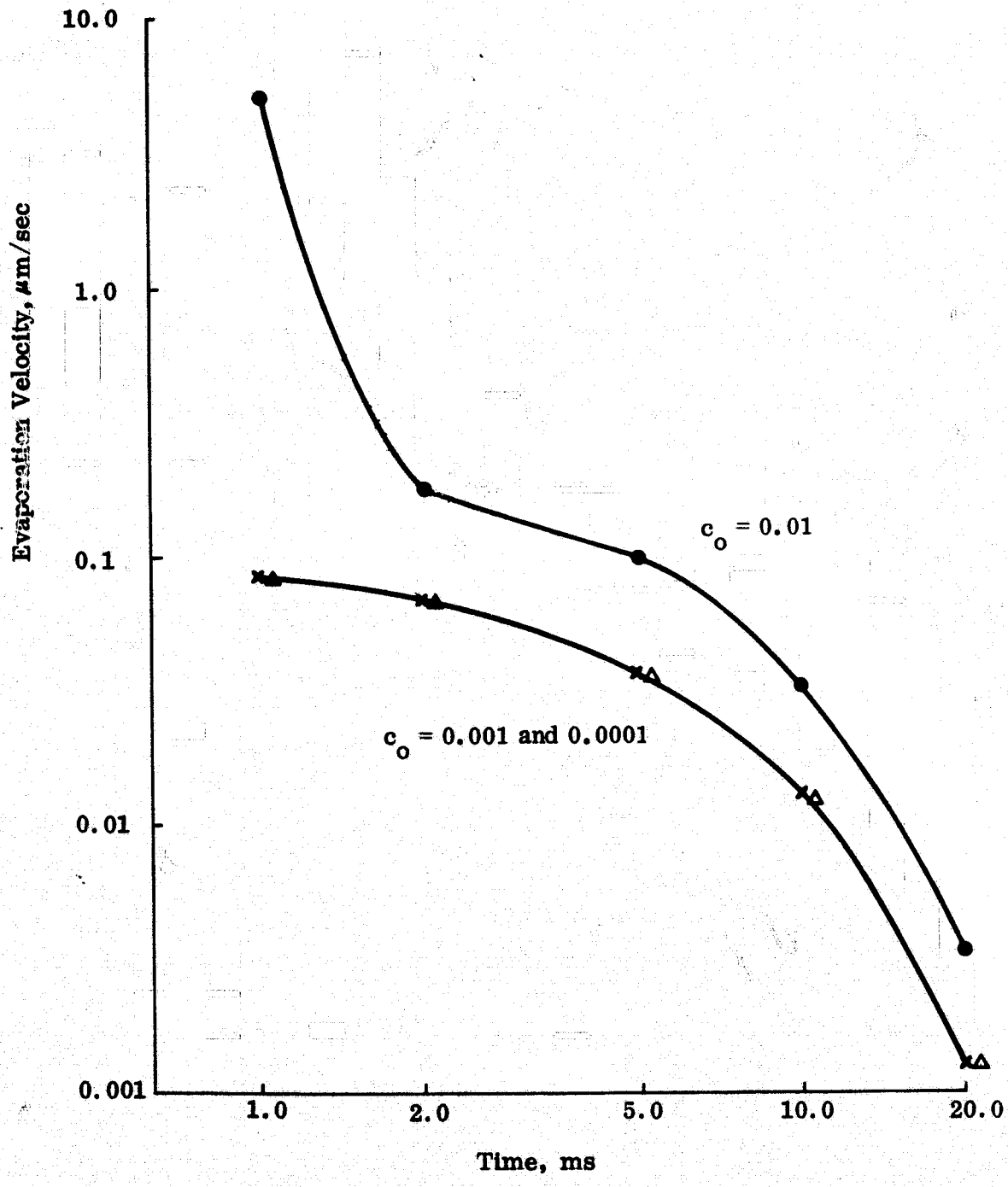

Fig. 12 Variation of Evaporation Velocity with c_o and t

4. THE GaAs STATISTICALLY DESIGNED EXPERIMENT

The GaAs designed experiment was set up to achieve the following objectives:

1. Provide samples for checking our numerical computation programs.
2. Study the effect of melt and growth variables on solute segregation and crystal quality.
3. Show the power of such designed experiments, particularly in space processing where the sample numbers are necessarily limited and the cost of experiments is too high to tolerate inefficiency.

A. Experimental Design

Altogether 16 crystals were scheduled to be grown, according to a statistical design.

Four input or independent variables were studied. They are:

1. Dopant types, at four levels: four in number:
   a. Cr
   b. Si
   c. Te
   d. Zn.
2. Dopant concentrations at four levels:
   a. 10^{17} atoms/cc
   b. 5×10^{17} atoms/cc
   c. 10^{18} atoms/cc
   d. 5×10^{18} atoms/cc.
3. Growth rates, also at four levels:
   a. 0.10 in/hr
   b. 0.16 in/hr
   c. 0.22 in/hr
   d. 0.28 in/hr

4. Temperature gradient, also at four levels:

   a. 4^{o} C/in.

   b. 6^{o} C/in.

   c. 8^{o}/in.

   d. 10^{o}C/in.

Table 11 gives the GaAs crystal growth plan.

The dependent variables or crystal characteristics to be measured at four different positions along the crystal axis (i.e., at $\frac{1}{2}$, 1, $1\frac{1}{2}$, and 2 inches from the seeding planes) are:

   a. Free carrier concentration, in atoms/cc

   b. Hall mobility, in cm^2/volt-sec

   c. Resistivity, in ohm-cm.

Zinc is a p-type dopant in GaAs, while Cr, Si, and Te are n-type dopants. Thus, the experiment gave both p and n-type GaAs crystals, with holes and electrons, respectively, as the majority carriers. Electrons have much higher mobilities than holes, as will be shown in this experiment also.

The doping concentration in this experiment varies over a factor of 50, from 1 x 10^{17} to 5 x 10^{18} atoms/cc. This covers a range wide enough to study, e.g., the effect of dopant concentration on segregation patterns or carrier mobility, without being too wide to cause difficulties in crystal growth or characterization.

Growth rate and liquid temperature gradient are two well-known growth parameters. Both affect not only the growth morphology but also the solute distribution or segregation pattern.

Among the dependent variables to be measured, the free carrier concentrations tie in with the solute redistribution pattern. Without contamination, compensation, but with 100% dopant ionization, these concentrations give the solute concentration profiles directly. The Hall mobility and resistivity are important characteristics for electronic materials such as GaAs.

The experimental plan was designed according to a completely orthogonal Latin Square Design (Ref. 11). This design allows the study of a maximum of five input variables at four levels each. In this experiment, however, only four input variables were included. The design is given in Table 11.

Table 11. GaAs Crystal Growth Schedule

Crystal No.	Dopant	Concentration	Growth Rate (in./hr.)	Temp. Grad. (^{o}C/in.)
1	Te	1×10^{17}	0.16	8
2	Si	5×10^{18}	0.22	8
3	Cr	5×10^{18}	0.28	6
4	Si	5×10^{17}	0.16	6
5	Zn	5×10^{18}	0.16	4
6	Cr	1×10^{18}	0.16	10
7	Te	1×10^{18}	0.22	6
8	Zn	1×10^{18}	0.28	8
9	Cr	5×10^{17}	0.10	8
10	Si	1×10^{18}	0.10	4
11	Si	1×10^{17}	0.28	10
12	Zn	1×10^{17}	0.10	6
13	Te	5×10^{17}	0.28	4
14	Zn	5×10^{17}	0.22	10
15	Cr	1×10^{17}	0.22	4
16	Te	5×10^{18}	0.10	10

B. Experimental Detail

The GaAs crystals were grown by Materials Research Corporation at Orangeburg, New York under contract. Furnace 3 was used exclusively for this experiment. This is a horizontal growth furnace measuring about five feet long and encased in a six-foot hood provided with access doors on all sides. A 2-inch (O. D.) quartz tube about 2 feet long is half filled with polycrystalline GaAs material together with the necessary dopants, and a single crystalline seed at one end. The growth furnace has three zones whose temperatures can be individually controlled to achieve the necessary temperature gradients in the liquid melt. After melting and homogenization and seed wetting, the furnace was moved away from the seed and growth began. Single crystals were not always obtained and some tests had to be repeated. Each crystal grown was later sliced by four diamond cuts at $\frac{1}{2}$, 1, $1\frac{1}{2}$ and 2 inches from the seed.

During the crystal growth, it was unexpectedly found that some vibrations enhanced the chances of obtaining single crystal throughout the entire crystal length. These vibration effects have been systematically studied and will be discussed in the following section.

C. Experimental Data

Macrophotographs on the three samples on each crystal were first taken. Examples of such photos are shown in Fig. 13, for Crystal No. 1. This crystal is thus seen to vary in width from 33 mm at $\frac{1}{2}$ inch, through 39.5 mm at 1 inch and 42.3 mm at $1\frac{1}{2}$ inches to 44.3 mm at 2 inches.

Data on free carrier concentrations, Hall mobilities, and resistivites at $\frac{1}{2}$, 1, $1\frac{1}{2}$ and 2 inches from the seed are given in Tables 12, 13 and 14.

Table 12. Free Carrier Concentration

Crys. No.	Intended Carrier Concentration (10^{17})	at $\frac{1}{2}$ in	at 1 in.	at $1\frac{1}{2}$ in.	at 2 in.	Avg.	Stand. Dev.	Coef. Varia.	Conc Avg/ Intend	Conc $2''/\frac{1}{2}''$
1	1.00	2.00	2.00	2.09	2.13	2.06	0.06	0.031	2.06	1.065
2	50.0	54.9	53.1	51.7	50.6	52.6	0.21	0.004	1.10	0.922
3	50.0	44.5	46.8	47.7	48.9	47.0	0.21	0.004	0.89	1.099
4	50.0	37.0	39.0	39.5	39.9	38.8	0.14	0.036	0.74	1.078
5	50.0	48.8	49.7	49.9	51.0	49.8	0.11	0.002	0.97	1.045
6	10.0	11.0	11.0	11.4	12.7	11.4	0.11	0.009	1.10	1.155
7	10.0	17.1	20.3	21.9	23.8	20.8	0.32	0.016	1.71	1.392
8	10.0	16.8	17.7	18.3	20.4	18.3	0.17	0.010	1.68	1.214
9	5.00	3.84	3.97	4.13	4.30	4.06	0.22	0.055	0.77	1.120
10	10.0	15.6	15.8	16.7	17.8	16.5	0.11	0.006	1.56	1.141
11	1.00	1.47	1.48	1.62	1.77	1.58	0.15	0.092	1.47	1.204
12*	1.00									
13	5.00	6.15	6.60	6.74	6.98	6.62	0.40	0.061	1.23	1.135
14*	5.00									
15	1.00	1.56	1.72	1.84	1.89	1.75	0.16	0.092	1.56	1.212
16	50.0	57.1	56.3	56.1	54.9	56.1	0.11	0.002	1.14	0.961
*Crystals 14 and 12 were not available.						Avg.		0.030	1.28	1.125

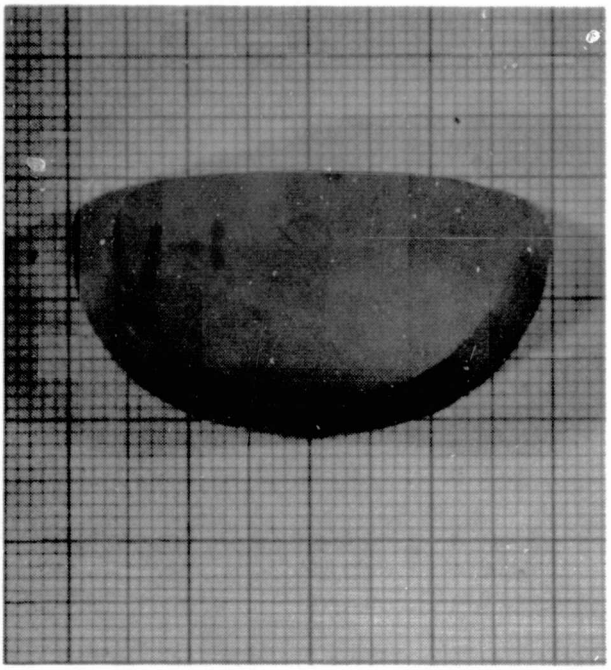

at 1 inch

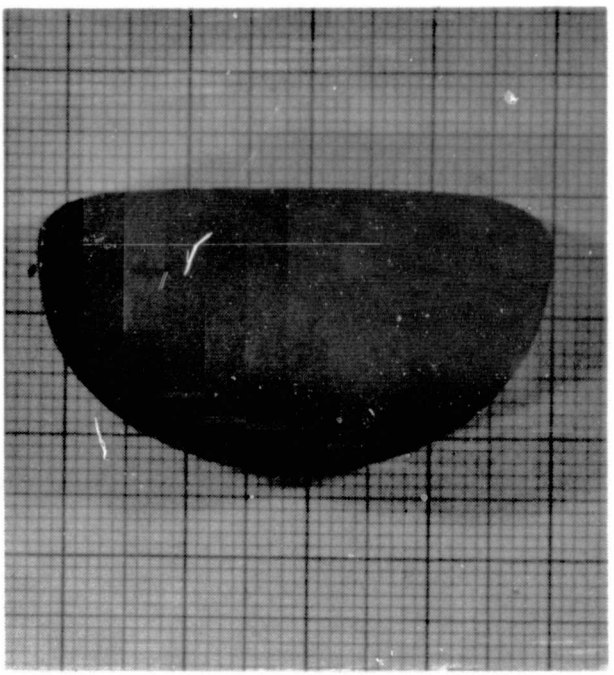

at 1 1/2 inches

1 cm

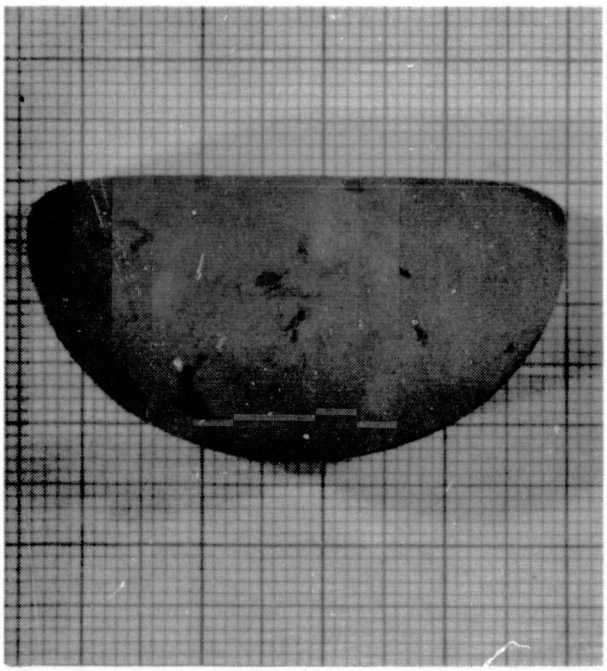

at 2 inches

Fig. 13 Macrophotos on Sample Slices 1-1, 1-2, and 1-3 for GaAs Crystal No. 1

Table 13 Hall Mobility Data

Crys. No.	Mobilities, (cm^2/v-sec) at $\frac{1}{2}$ in.	at 1 in.	at $1\frac{1}{2}$ in.	at 2 in.	Avg.	Stand. Dev.	Coef. Var.	Ratio 2 in/$\frac{1}{2}$ in.
1	2156	2153	2141	2136	2146.5	9.71	0.00453	0.991
2	1371	1402	1409	1429	1402.8	28.17	0.02008	1.042
3	2370	2362	2357	2342	2357.8	13.60	0.00577	0.988
4	3330	3327	3320	3318	3323.8	5.83	0.00175	0.996
5	163	164	167	169	165.8	2.43	0.01465	1.037
6	2376	2365	2366	2360	2366.8	7.77	0.00328	0.993
7	3247	3252	3242	3217	3264.5	17.00	0.00521	0.991
8	138	144	147	149	144.5	5.34	0.03697	1.080
9	2279	2264	2250	2239	2258.0	19.43	0.00860	0.982
10	2010	2007	2007	1988	2003.0	10.68	0.00533	0.990
11	3401	3399	3374	3368	3385.5	16.03	0.00473	0.990
12*								
13	2719	2706	2701	2693	2704.8	12.63	0.00467	0.990
14*								
15	1480	1476	1465	1462	1470.8	8.74	0.00594	0.988
16	2438	2430	2427	2401	2424.0	17.97	0.00242	0.985

*Crystals 12 and 14 are not available.

Table 14 Resistivity Data (in 10^{-3} ohm-cm)

Crys. No.	at $\frac{1}{2}$ in.	at 1 in.	at $1\frac{1}{2}$ in.	at 2 in.	Avg.	Stand. Dev.	Coef. Var.	Ratio 2 in./$\frac{1}{2}$ in.
1	14.48	14.47	14.41	14.31	14.42	0.083	0.0057	0.988
2	83.0	94.0	96.0	97.0	93.0	7.77	0.0835	1.193
3	1.9	1.85	1.76	1.64	1.79	0.126	0.0705	0.863
4	5.09	5.16	5.19	5.27	5.18	0.087	0.0169	1.035
5	7.85	7.63	7.41	7.41	7.58	0.214	0.0282	0.944
6	240.	230.	210.	170.	212.5	34.0	0.160	0.708
7	1.09	1.34	1.57	2.03	1.51	0.457	0.302	1.862
8	26.9	25.2	23.7	21.6	24.35	2.57	0.106	0.803
9	7.15	7.16	7.10	7.06	7.12	0.0486	0.0068	0.987
10	2.00	1.85	1.84	1.74	1.86	0.126	0.0168	0.870
11	12.5	12.7	12.9	13.4	12.88	0.437	0.034	1.072
12*								
13	3.06	3.18	3.29	3.36	3.22	0.146	0.0452	1.098
14*								
15	270.	260.	220.	190.	235.	38.9	0.165	0.704
16	4.49	4.32	4.31	4.33	4.36	0.087	0.0200	0.964
Avg								1.006

*Crystals 12 and 14 were not available.

D. Results and Conclusions

Analysis of the experimental data (Ref. 11) have yielded the following results

1. On Free Carrier Concentrations

a. Concentration Variations Along the Crystal Length

1. Without exceptions, this concentration changed monotonically along the crystal length.

2. Concentrations increased in 12 of the 14 crystals. Only in No. 2 and 16 did the concentration decrease with distance from the seed. For the 12 crystals, the average ratio of concentration at 2 inches to that at $\frac{1}{2}$ inch was 1.176 (or 17.6% increase in concentration from $\frac{1}{2}$ inch to 2 inches). The same average ratio was 0.942 (or 5.8% decrease in concentration from $\frac{1}{2}$ inch to 2 inches) for the other two crystals. The combined average for this ratio on all 14 crystals was 1.125. Thus, on the average, the concentration increased from $\frac{1}{2}$ inch to 2 inches by about 12.5%. These small increases indicate that nearly steady-state conditions were reached after $\frac{1}{2}$ inch.

3. Cr-doped crystals had the greatest increases in concentration from $\frac{1}{2}$ inch to 2 inches by an average of 14.6%; Te-doped crystals next, by 13.8%; followed by Zn-doped crystals (12.6%) and Si crystals (8.6%).

4. The maximum ratio of concentration at 2 inches to that at $\frac{1}{2}$ inch (last column of Table 12) was 1.392 (or 39.2% increase from $\frac{1}{2}$ inch to 2 inches) on Te-doped crystal No. 7; the minimum ratio was 0.922 (or 7.8% decrease from $\frac{1}{2}$ inch to 2 inches) on Si-doped crystal No. 2.

5. Increasing the growth rate seemed to increase this ratio, from 1.074 at growth rate of 0.10 in./hr to 1.163 at growth rate of 0.28 in./hr at least during the initial transient conditions. This conclusion agrees with the common solidification theory based on the solute-enriched layer ahead of the solid-liquid interface (Ref 12).

6. No systematic effects of melt concentration or liquid temperature gradient have been observed.

b. Ratio of Average Concentration to Initial Melt Concentration

These ratios are given in Column 10 of Table 12:

1. The average concentrations in the crystals were generally higher than the concentrations in the initial melts, by about 28% on the average.

2. More crystals (10) had higher average concentrations presumably due to contamination; fewer crystals (4) had lower average concentrations probably due to compensation, than the initial melt compositions.

3. Maximum ratios of 2.00 and 1.71 (100% and 71% higher) occurred on Te-doped crystals No. 1 and 7; minimum ratio of 0.74 (26% less) occurred on Si-doped crystal No. 4.

4. On the average, Te-doped crystals had the highest ratios, averaging 1.52, Cr-doped crystals the lowest with average 1.08, Si (1.22 average) and Zn (1.33 average) crystals had intermediate ratios.

5. Increasing the growth rate increased this ratio, from 1.16 at 0.10 in./hr, through 1.20 and 1.46 at 0.16 and 0.22 in./hr respectively, to 1.32 at 0.28 in./hr.

c. On the Coefficient of Variation on Concentration

This coefficient is also a measure of the variation of carrier concentration along the crystal length, due to the combined effect of doping, contamination, and compensation.

1. The average coefficient of variation on carrier concentration was 0.030.

2. Again, doping types had important effect. Cr-doped crystals had the highest coefficients, averaging 0.040. Si-doped crystals were next, averaging 0.034, followed by Te-doped crystals, averaging 0.028. Zn-doped had the lowest coefficients, i.e., the least variable, averaging 0.006.

3. Doping concentrations had the most important effect on these coefficients; increasing the initial melt concentration reduced the coefficients. The averages were: 0.072 at 10^{17} atoms/cc; 0.051 at 5×10^{17} atoms/cc; 0.010 at 10^{18} atoms/cc, and 0.003 at 5×10^{18} atoms/cc.

4. Increasing growth rate also increased these coefficients. Averages were: 0.020 at 0.10 to 0.16 in./hr; 0.37 at 0.22 in./hr, and 0.42 at 0.28 in./hr.

2. On Mobilities

a. Average Mobility

1. The average mobility of all 56 readings (four on each crystal) was 1587 cm^2/v-sec.

2. Dopant type again had the most important effect. Zn-doping gave the lowest mobility. The average was only 155 cm^2/v-sec, compared to the average of 2340 cm^2/v-sec for the other three types of doping. The ratio of 15.1 (2340/155) agrees with the fact that the Zn-doped crystals are p-type materials with holes as the majority carriers, while the other three types are all n-type materials with electrons as the majority carriers. Electrons move much faster than holes in semiconductors such as GaAs.

3. Among crystals other than Zn-doped, Te-doping gave the highest mobility (2604 cm^2/v-sec) and Cr-doping the lowest (2075 cm^2/v-sec), with Si-doping in the middle (2371 cm^2/v-sec).

4. As expected, increasing the doping concentration in the initial growth melt reduced the average mobility, from 2465 cm^2/v-sec at initial melt concentration c_o of 10^{17} or 5×10^{17} atoms/cc, through 1223 cm^2/v-sec at $c_o = 10^{18}$ atoms/cc, to 1074 cm^2/v-sec at 5×10^{18} atoms/cc.

b. Mobility Variation Along Crystal Length

1. With only one notable exception on Crystal No. 7, mobility changed monotonically along the crystal length.

2. Eleven crystals decreased, and only three crystals (No. 2, 5, and 8) increased in mobility from the seed ends on. This is most easily seen by examining the ratio of mobility at 2 inches to that at $\frac{1}{2}$ inch. The average ratio for the 11 crystals was 0.989 (or 1.1% decrease from $\frac{1}{2}$ inch to 2 inches). The average ratio for the 3 crystals was 1.053 (or 5.3% increase from $\frac{1}{2}$ inch to

2 inches). The combined average for all 14 crystals was 1.003 (or only 0.3% increase from $\frac{1}{2}$ inch to 2 inches).

3. The maximum ratio was 1.080 (or 8.0% increase in mobility from $\frac{1}{2}$ inch to 2 inches) on Crystal No. 8, and the minimum ratio was 0.982 (or 1.8% decrease in mobility from $\frac{1}{2}$ inch to 2 inches) on Crystal No. 9.

4. Increasing the growth rate v increased this ratio, from 0.985 at v = 0.10 in./hr, through 1.004 at v = 0.16 in./hr and 1.007 at v = 0.22 in./hr, to 1.012 at v = 0.28 in./hr.

5. Increasing initial doping concentration in the melt also increased this ratio, averages being 0.990 at $c_o = 10^{17}$ or 5×10^{17} atoms/cc to 1.013 at $c_o = 10^{18}$ or 5×10^{18} atoms/cc.

c. On Coefficient of Variation on Mobility

This coefficient is also a measure of the variation of mobility along the crystal length, due to the combined effect of doping and crystal perfection.

1. The average coefficient of variation on mobility for all 14 crystals was 0.0062 (or 0.62%). Maximum coefficient was 3.70% with Crystal No. 8, and the minimum coefficient was 0.18% with Crystal No. 4.

2. Zn-doping gave decidedly more mobility variation along the crystal length than the other three types of doping. Averages were 0.0233 (or 2.33%) vs 0.0050 (or 0.50%).

3. Increasing the growth rate v increased the mobility variation along the crystal length. Averages were 0.0043 (or 0.43%) for v = 0.10 and 0.16 in./hr vs 0.0084 (or 0.84%) for v = 0.22 and 0.28 in./hr.

4. Increasing doping concentration in the initial melt also increased the mobility variations along the crystal length. Averages were 0.0046 (or 0.46%) for $c_o = 10^{17}$ and 5×10^{17} atoms/cc vs 0.0083 (or 0.83%) for $c_o = 10^{18}$ and 5×10^{18} atoms/cc.

3. On Average Resistivities

1. The minimum resistivity of all 56 readings (four on each crystal) was 1.64×10^{-3}, and the maximum 0.27 ohm-cm.

2. Among the four different types of dopants, Cr gave the highest average resistivity (28.2×10^{-3} ohm-cm), while Te the lowest (4.2×10^{-3} ohm-cm), with Si (10.4×10^{-3} ohm-cm) and Zn (12.3×10^{-3} ohm-cm) giving intermediate values. This conclusion agrees with the common observation that Cr is a "semi-insultaing" dopant in the GaAs while Te can give very low resistivity materials.

3. As expected, the higher the dopant concentration, the lower the resistivity. Averages are 35.2×10^{-3}, 4.91×10^{-3}, 11.0×10^{-3}, and 8.6×10^{-3} ohm-cm at concentrations $c_o = 10^{17}$, 5×10^{17}, 10^{18}, and 5×10^{18} atoms/cc.

E. Discussion on the GaAs Experiment

Crystal growth is generally still an art. Also, two of the 16 crystals originally planned in this experiment could not be grown because of unexpected personnel changes at our vendor. The measurement errors appeared to be large, when one compares the measured results given in Tables 12 to 14 with other measured results independently obtained by Prof. Franklin Wang's group at the State University of New York at Stony Brook (See Table 15).

Yet the results appear to be useful. In particular, the conclusions seem to check well with established practices in the industry (Ref. 13). There are no anomalies or unique results observed.

The ratios of concentration at 2 inches to that at $\frac{1}{2}$ inch give some idea about the segregation coefficients. The higher this ratio, the greater the segregation coefficient. Since Te-doped crystals had the highest ratios, 1.52 on the average, hence, Te would have the highest segregation coefficient in the GaAs melt and Cr the lowest segregation coefficient in the GaAs melt. Si and Zn would have intermediate segregation coefficients, with the segregation coefficient of Zn being greater than that of Si. Exact segregation coefficients on all these four dopants in GaAs are not available in the literature.

One interesting confirmation of the existing theory (Ref. 12) is the conclusion that increasing the growth rate increased the above ratio. This can be explained as follows: increasing the growth rate increases the solute pile-up ahead of the solid-liquid interface, at least for the beginning portions of completed growth. The localized liquid solute concentration at the interface is increased. The solute concentration in the solid crystal freezing out also is increased to maintain a nearly constant segregation coefficient for these dilute melts, hence, the observed results.

One disturbing thing is that the melts in some cases were contaminated or compensated. Some crystals had the solute concentrations decreasing along the length instead of increasing. The sources of this contamination is not known.

Contamination of semiconductor melts is not uncommon (Ref. 13) in view of the extreme dilution of the doping elements. Generally, the solute concentrations of the solutes varied in this experiment from 10^{17} to 5×10^{18} atoms/cc, corresponding to ppm or tens of ppm. A single dust particle near the seed would thus easily have contaminated the melt and even compensated the trace doping elements.

The contamination problems, however, make the strict correlation with computed profiles difficult. There are also only four data points on each crystal even though we tried hard but failed to develop other more or less continuous probing techniques to obtain more data.

Nevertheless, we believe that this experiment fulfilled two of the stated objectives of the experiment, i.e., to study the effect of melt and growth variables on solute segregation and crystal quality; and to show the usefulness of such designed experiments. No correlation between computed and measured results has been made, partly because of budgetary constraints.

In particular, we have shown that this type of statistically designed experiment works, in crystal growth also. The good correlation of the observed results with the generally accepted results lend credence to this approach. We also feel that this type of experiment is particularly useful in space. This is because space experiments must necessarily be limited in sample size, and yet zero-gravity effects may be so subtle relative to the many ever-existing noises (experimental errors or other effects) (Ref. 3) that improved techniques in experimental design and data analyses must be resorted to for meaningful results to be obtained with a minimum number of samples, in a short time, and at low costs.

Table 15 Data on GaAs Samples, Work Done at SUNY

Crys.	Resistivity, ohm-cm	Mobility, cm^2/volt. sec	Concentration, 10^{17}
1	0.00193	2212	14.6
2	0.00529	981	12.0
3	0.00565	2160	5.12
3	0.00533	2296	5.11
4	0.0026	1122	21.4
4	0.00232	1649	16.3
5	0.0348	90	19.9
5	0.032	84	23.0
6	0.170	2082	0.17
6	0.0756	5325	0.155
7	0.00192	1232	26.4
7	0.00192	1265	25.7
8	0.0357	90	19.4
8	0.0339	120	15.3
10	0.00335	1611	11.6
10	0.00287	1455	14.9
11	0.0166	2840	1.32
11	0.0156	2722	1.47
13	0.018	2463	1.40
13	0.0176	2987	1.19
15	0.594	989	0.106
15	0.755	1021	0.0811
16	0.00208	1213	24.8

5. SEGREGATION IN GaAs CRYSTALS

In connection with our statistically designed GaAs experiment, we selected a number of GaAs ($\frac{1}{2}$ in) slabs for microprobe analyses. Studies on the Ga and As concentration profiles reveal an unanticipated segregation phenomenon and some evidence of strong convection currents. This section details the experimental procedures, results, data analyses, conclusions, and discussions.

A. Experimental

The GaAs crystals were grown at our vendor, Materials Research Corporation at Orangeburg, New York. The growth equipment was horizontal Bridgeman quartz tube furnace. The GaAs polycrystalline melt materials and a single crystalline seed were placed in a sealed 2 inches diam x 2 feet quartz tube or boat filled with argon under partial vacuum. Only about half of the sealed quartz tube was filled with GaAs.

The sealed quartz tube was placed inside the quartz tube, which was supported in a SiC tube about $\frac{1}{4}$ inch-thick. The SiC tube is heated by three sets of equally spaced Globars inside an insulated furnace (Fig. 14). The furnace is thus longitudinally divided into three individually controlled temperature zones. Specifically, each zone can be controlled in temperature to about $\frac{1}{2}^{o}$C independently of the other two zones. The furnace is driven by a scan motor to move longitudinally relative to the SiC and quartz tubes containing the sealed quartz tube and GaAs melt for the growth to initiate and continue.

It was found that various kinds of vibrations existed on the growth furnace. Further, the vibrations from the scan motor markedly and unexpectedly improved the crystal quality and yield. Details of these vibration effects will be described in Section 6.

The GaAs were usually doped with 10^{17} to 5×10^{18} atoms/cc of Cr, Si, Te, and Zn. Typical growth conditions were 0.19 in./hr with a liquid temperature gradient of 7°C/in.

After growth, the crystals were sliced on an ID diamond saw into $\frac{1}{2}$ inch slices. Selected slice samples were mounted and microprobed at 3-micron intervals up to 72 microns with an electron microprobe Model AMR/3 made by Phillips.

B. Results

On each GaAs slice sample, a number of microprobe transverses were taken. Figure 15 shows locations of the surface points from which concentration profiles perpendicular to the surface were made on a typical sample.

The Ga and As concentration profiles related to these surface points were given in Fig. 16 to 21.

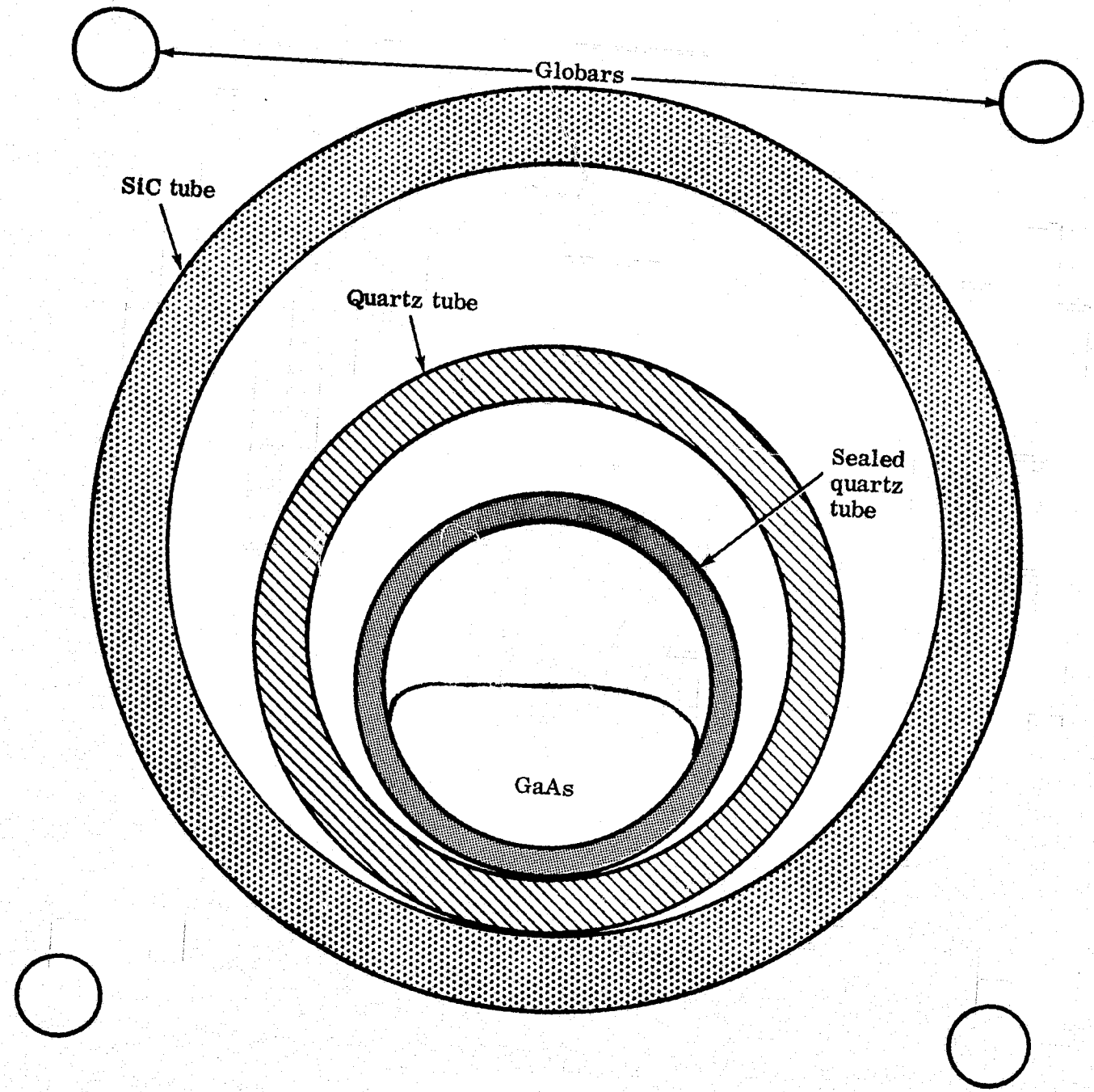

Fig. 14 GaAs Growth Furnace

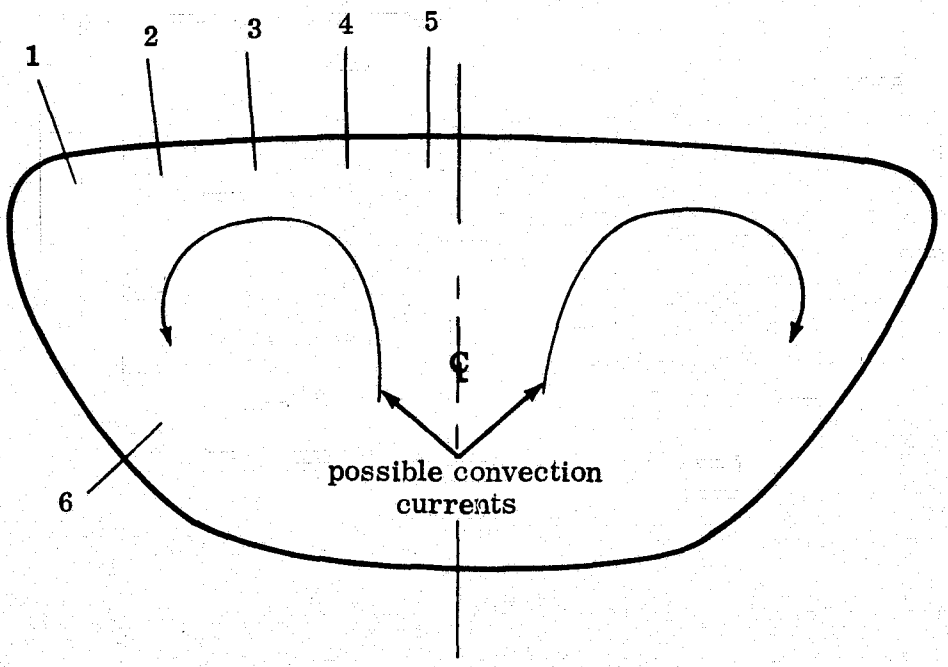

Fig. 15 Location of the Ga and As Microprobe Transverses

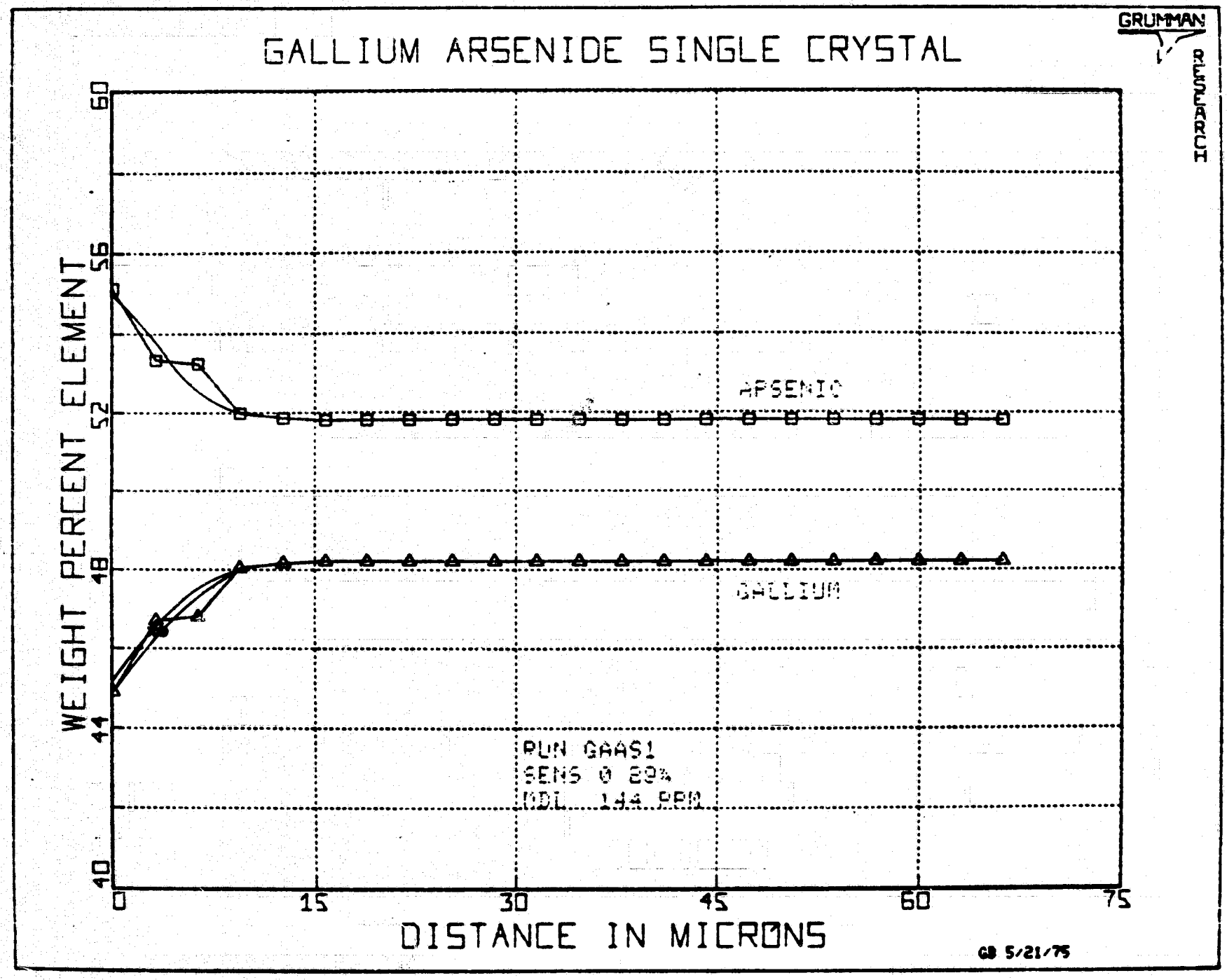

Fig. 16 Ga and As Concentration Profiles at Point 1

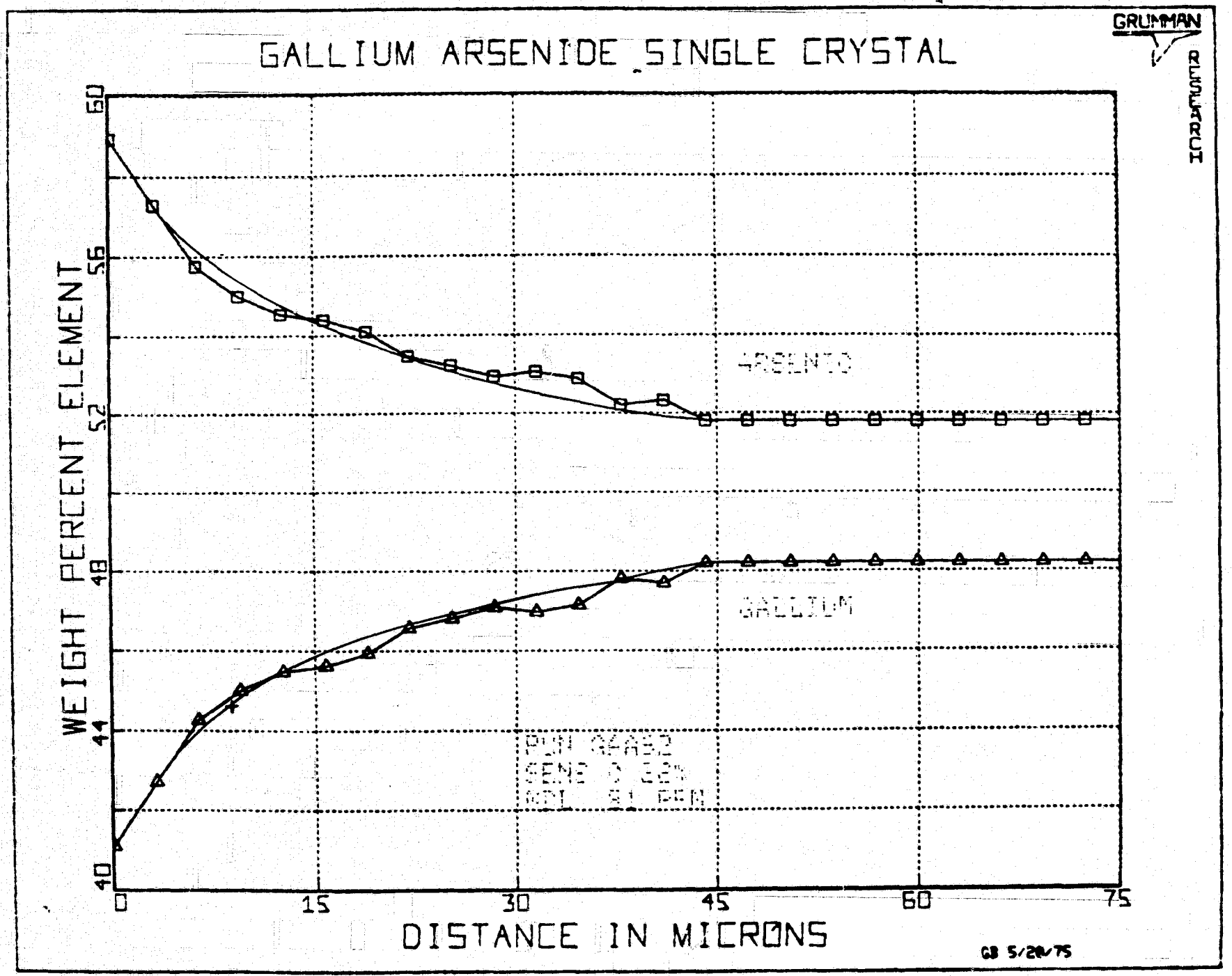

Fig. 17 Ga and As Concentration Profiles at Point 2

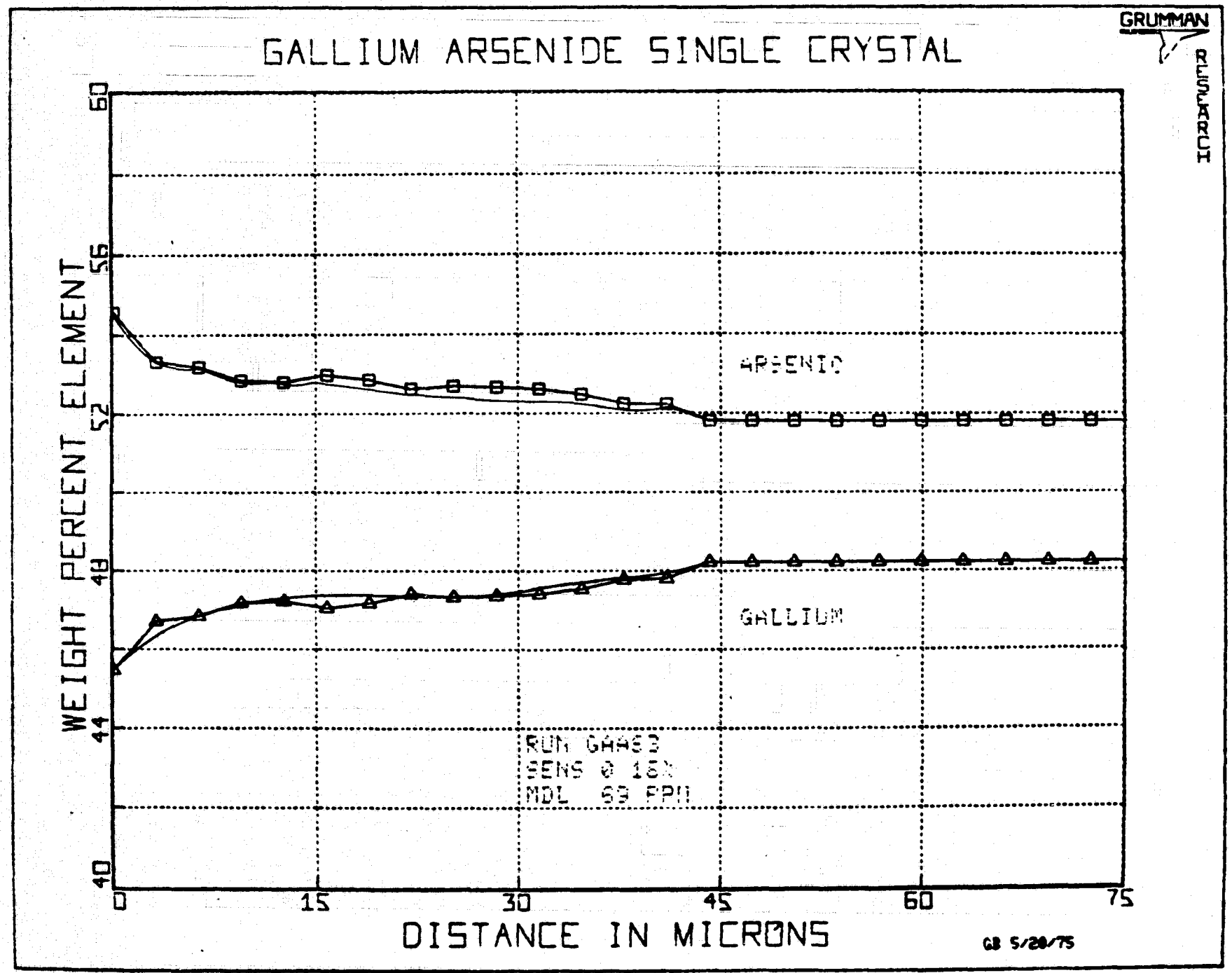

Fig. 18 Ga and As Concentration Profiles at Point 3

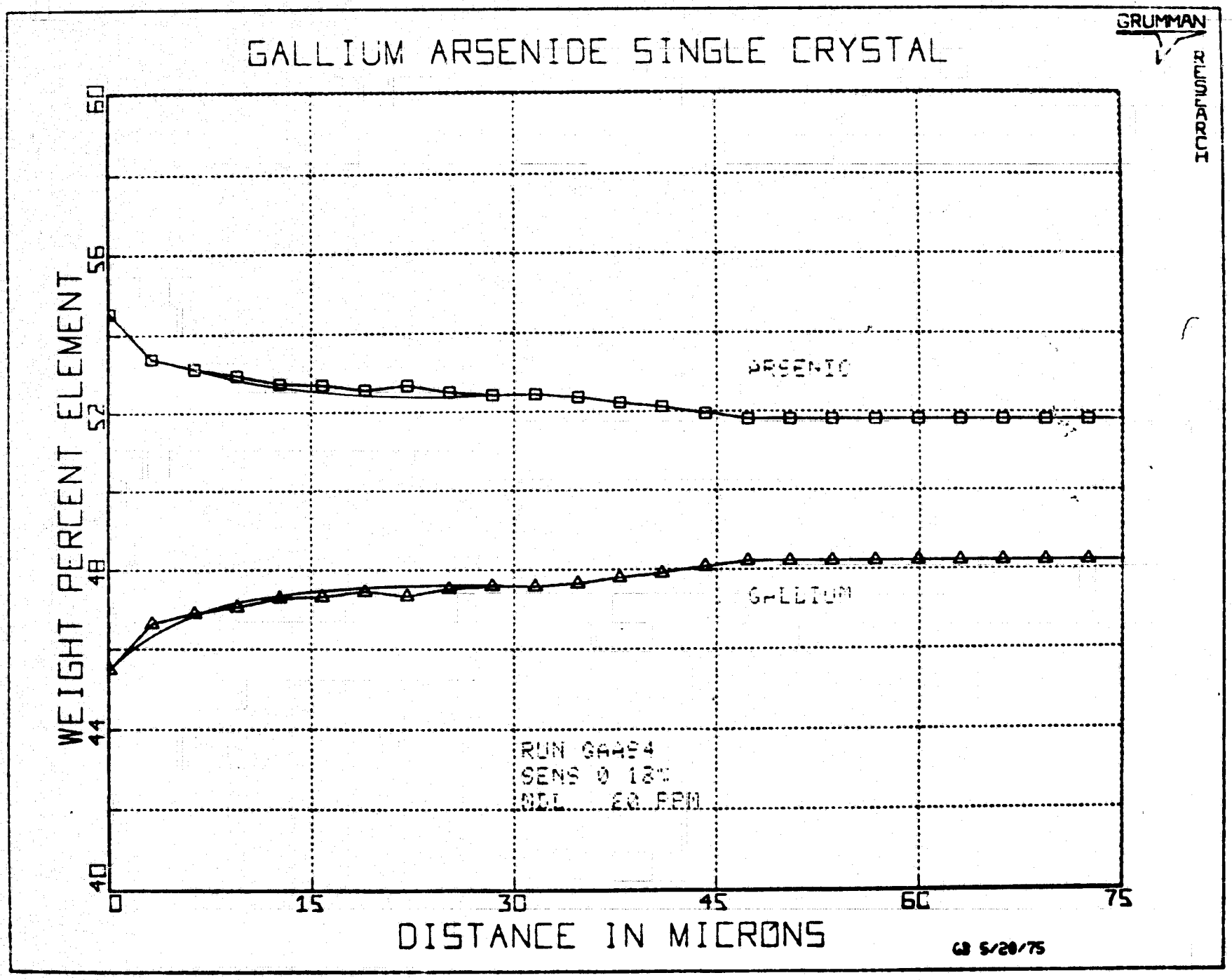

Fig. 19 Ga and As Concentration Profiles at Point 4

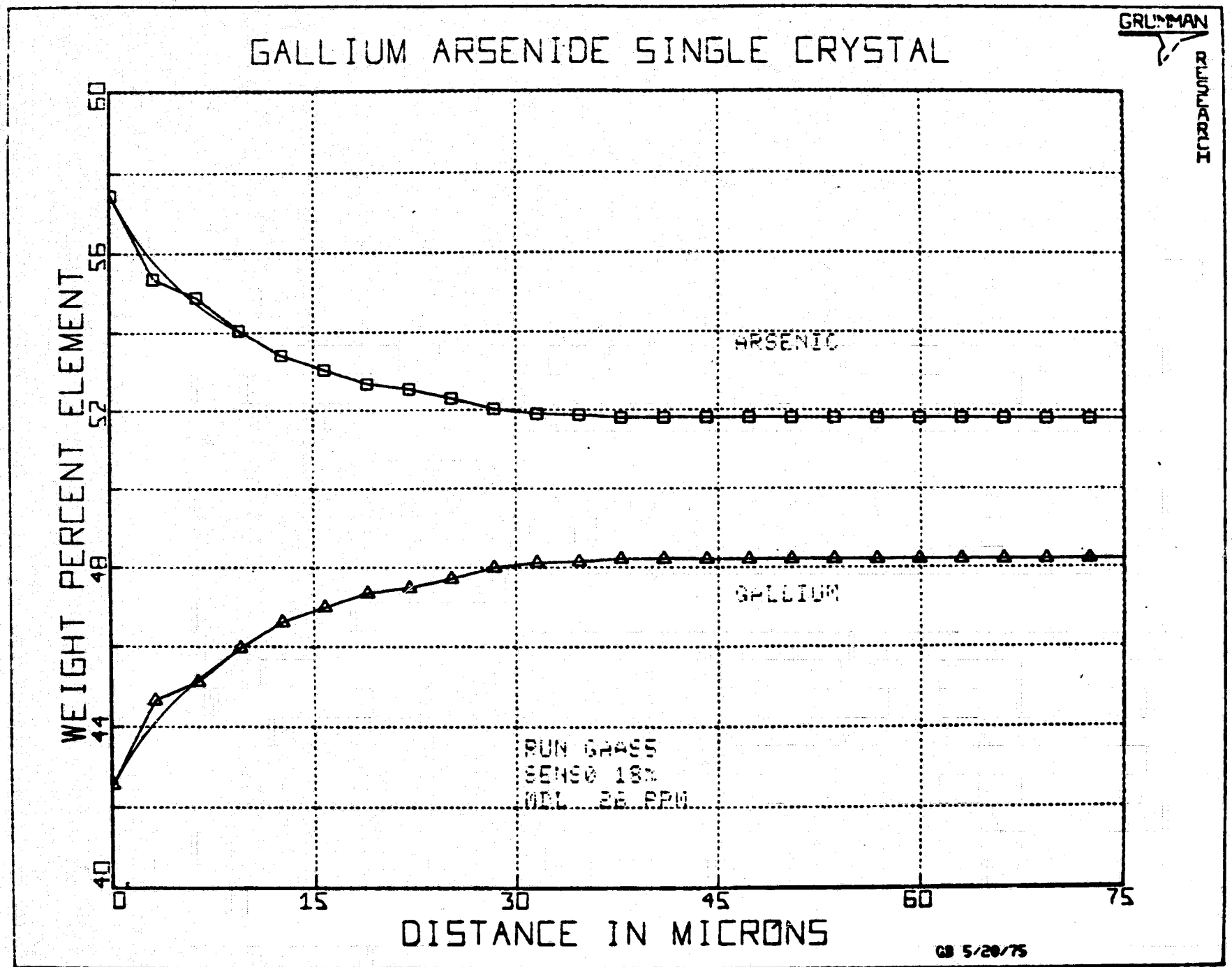

Fig. 20 Ga and As Concentration Profiles at Point 5

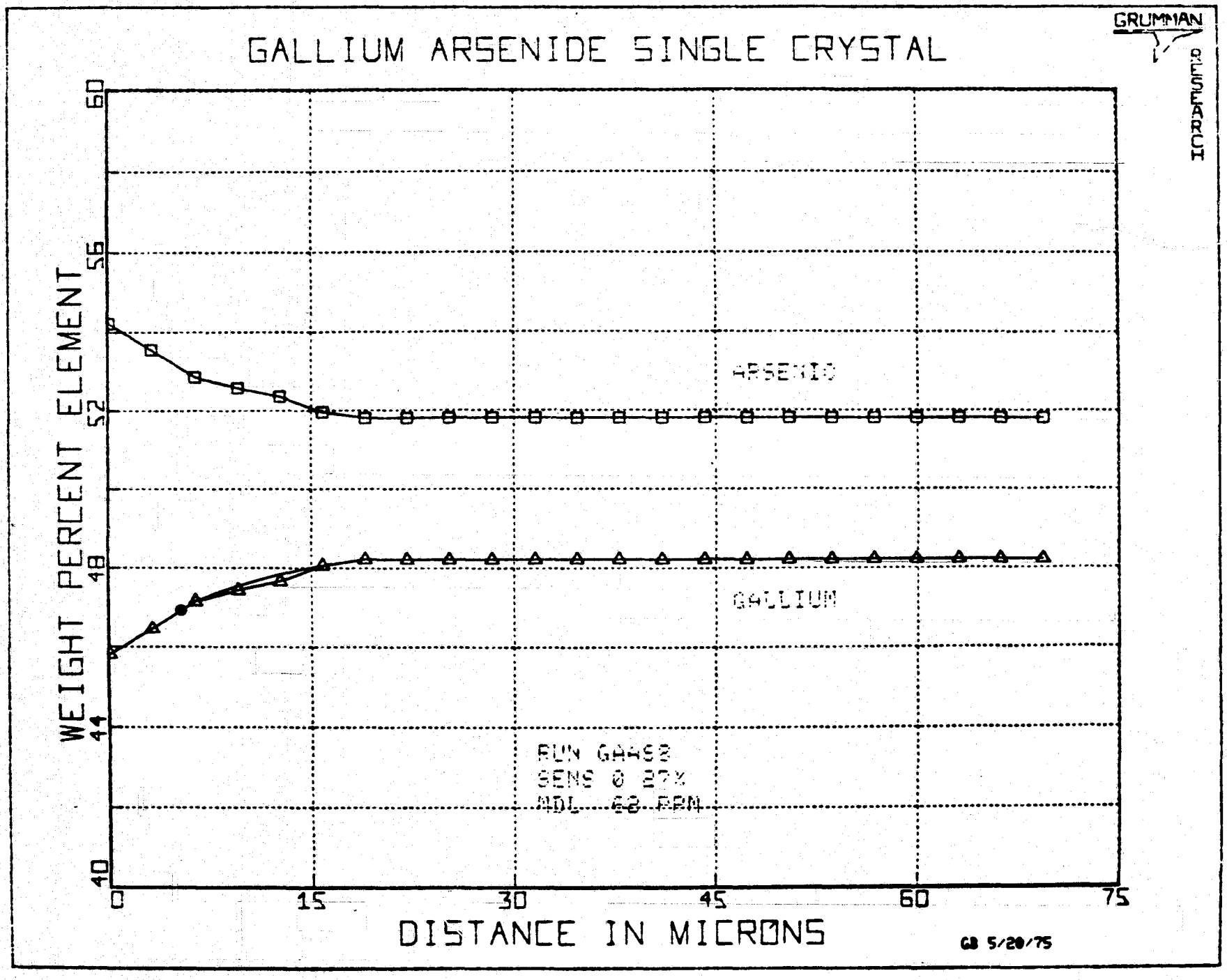

Fig. 21 Ga and As Concentration Profiles at Point 6

C. Analysis of Results

At all the six surface locations, Ga is depleted, while As is enriched. The distance, d, over which this depletion or enrichment takes place varies from 15 microns at location 1, to 47 microns at location 4. The values of d are given in Table 16, line 2 .

Beyond this distance d, the Ga and As concentrations in the bulk of the crystal are constant, down to the third decimal place: Ga at 48.3 weight percent (50.1 atomic percent), and As at 51.7 weight percent (49.9 atomic percent). Notice that the sum of Ga and As concentrations add up to 1.000, as they should. The same is true for any probed point on the sample.

The surface concentrations of Ga and As, however, vary from location to location. Ga concentration varies from 0.411 at surface point 2 to 0.458 at surface point 6, (line 7 of Table 16) while As concentration varies from 0.542 at surface point 6 to 0.589 at surface point 2 (line 4 of Table 16). Average surface concentrations are Ga 0.4422 and As 0.5578 weight fractions (or 46.0 and 54.0 atomic percent). These surface concentrations are also given in Table 16.

Table 16 (lines 6 and 9) also gives the average concentrations (of Ga and As) for each transverse, and the "half distance" d/2 showing the depths inside the surafce that have these average concentrations.

D. Discussion

The precision of the microprobing is better than 0.001 in weight fractions, for both Ga and As. This can be seen from the following:

1. Underneath the surface regions (i.e., 15 to 47 microns thick), the Ga concentration is constant at 0.483 ± 0.000; and As concentration is constant at 0.517 ± 0.000, for the (up to 18 times at location 1) repeated readings at 3 micron intervals.

2. The sum of Ga and As concentrations at <u>any</u> point on the sample adds up to 1.000 ± 0.000.

The observed concentration variations must, therefore, be real.

These surface concentrations cannot be caused directly by surface evaporations, because these evaporations are limited generally to the fractional micron surface layers, as shown in Section 2.

Also, if the segregations were due to evaporation, we would except the surface regions to be depleted in As and enriched in Ga, because of vapor pressure considerations given below. This is opposite to what was observed. Table 17, taken from p. 57 of Ref. 14, for example, gives the temperatures (in ^{o}C) for As and Ga to reach different vapor pressures (in atmospheres). Notice the much higher Ga evaporating temperature than As for the same vapor pressure. Also, the density, molecular weight, and mole fraction of Ga in the evaporating GaAs are roughly equal to the corresponding values for As (Ref. 13).

We must, then, assume that the observed Ga and As segregation patterns are caused by solidification.

Table 16. Characterization of GaAs Sample

Location	1	2	3	4	5	6	Average	Line
			Distances					1
d	15	45	45	47	38	19	34.8 microns	2
d/2	4.0	8.9	6.5	7.0	6.9	5.4	6.45 microns	3
			As concentrations (Weight Fractions)					
Surface	0.551	0.589	0.546	0.545	0.574	0.542	0.5578	4
Interior	0.517	0.517	0.517	0.517	0.517	0.517	0.5170	5
Average	0.534	0.553	0.532	0.531	0.546	0.530	0.5377	6
			Ga Concentrations (Weight Fractions)					
Surface	0.449	0.411	0.454	0.455	0.426	0.458	0.4422	7
Interior	0.483	0.483	0.483	0.483	0.483	0.483	0.4830	8
Average	0.466	0.447	0.468	0.469	0.454	0.470	0.4623	9
			Effective Segregation Coefficients (Surface/Interior)					
As	1.066	1.139	1.056	1.054	1.110	1.048	1.079	10
Ga	0.930	0.851	0.940	0.942	0.882	0.948	0.9155	11
			Estimated Growth Velocities					
	0.775	0.180	0.537	0.530	0.278	0.739	0.5065 cm/sec	12

Table 17. Evaporating Temperatures To Reach Given Vapor Pressures

Pressures	0.0001	0.001	0.01	0.1	0.5	1.0	Atm
As	308	363	428	499	578	610	^{o}C
Ga	1178	1329	1515	1751	1965	2071	^{o}C

The exact leveling off of the Ga and As concentrations beyond the surface regions indicates the attainment of steady-state conditions. The surface segregations are, therefore, merely transient solidification results.

The surface regions are very thin (15 to 47 microns) relative to the size of the samples (oblong shape 24 mm x 46 mm). Hence, the initial melt concentrations also were Ga 0.483 and As 0.517.

The effective segregation coefficients for Ga and As in GaAs melt are, therefore, about 0.9155 and 1.079, respectively. However, these coefficients, obtained from the surface and initial concentrations, vary from location to location, as given in Table 16 (lines 10 and 11).

Notice that the effective segregation coefficient for Ga in GaAs varies from 0.851 at location 2 to 0.948 at location 6, a range of 11.4%. The same coefficient for As in GaAs varies from 1.048 at location 6 to 1.139 at location 2, a range of 8.0%.

The surface concentrations, C_f, of As (or Ga) appeared to depend on the half distance, d/2 as shown in Fig. 22. A regression analysis (Ref. 15) shows, however, that the correlation is statistically insignificant. For example, the regression coefficient is only 0.6918, the value of t is 1.916, and the value of F is only 3.672. All these values are below the 90% significance levels (Ref. 15). Thus, the surface concentration C_f is independent of the half distance d/2.

The surface region thickness d_s also appears to depend on the half distance d/2, as shown in Fig. 23. A regression analysis confirms this. The (regression) coefficient is R = 0.8426, t = 3.129, and F = 9.791. These are all significant at the 95% levels (Ref. 15).

The prediction equation is:

$$t_s = -11.95 + 7.253 \times d/2 \pm 8.55, \; t_s \text{ and } d/2 \text{ both in microns.}$$

where ±8.55 is the adjusted standard error of estimate (Refs. 16-17).

From the surface and bulk (interior) concentrations, and the half distances, one can estimate the local freezing velocities V, following the Pohl diffusion-limited model (Ref. 18). These V values are given in Table 16, line 12.

As indicated above, the microprobing accuracy is good, probably to better than 0.0005 weight fraction. The observed Ga and As concentration variations are, therefore, real.

Therefore we can safely say that Ga was depleted from the surface and As enriched at the surface. The primary mechanisms of this depletion and enrichment could not be evaporation. They must be the result of solidification.

That is, Ga segregated from the GaAs melt having an initial melt concentration of 48.3% by weight, with an effective segregation coefficient less than unity. The average coefficient was 0.9155. On the other hand, As segregated from the same GaAs melt having an initial melt concentration of 0.517, with an effective segregation coefficient greater than unity. The average coefficient was 1.079.

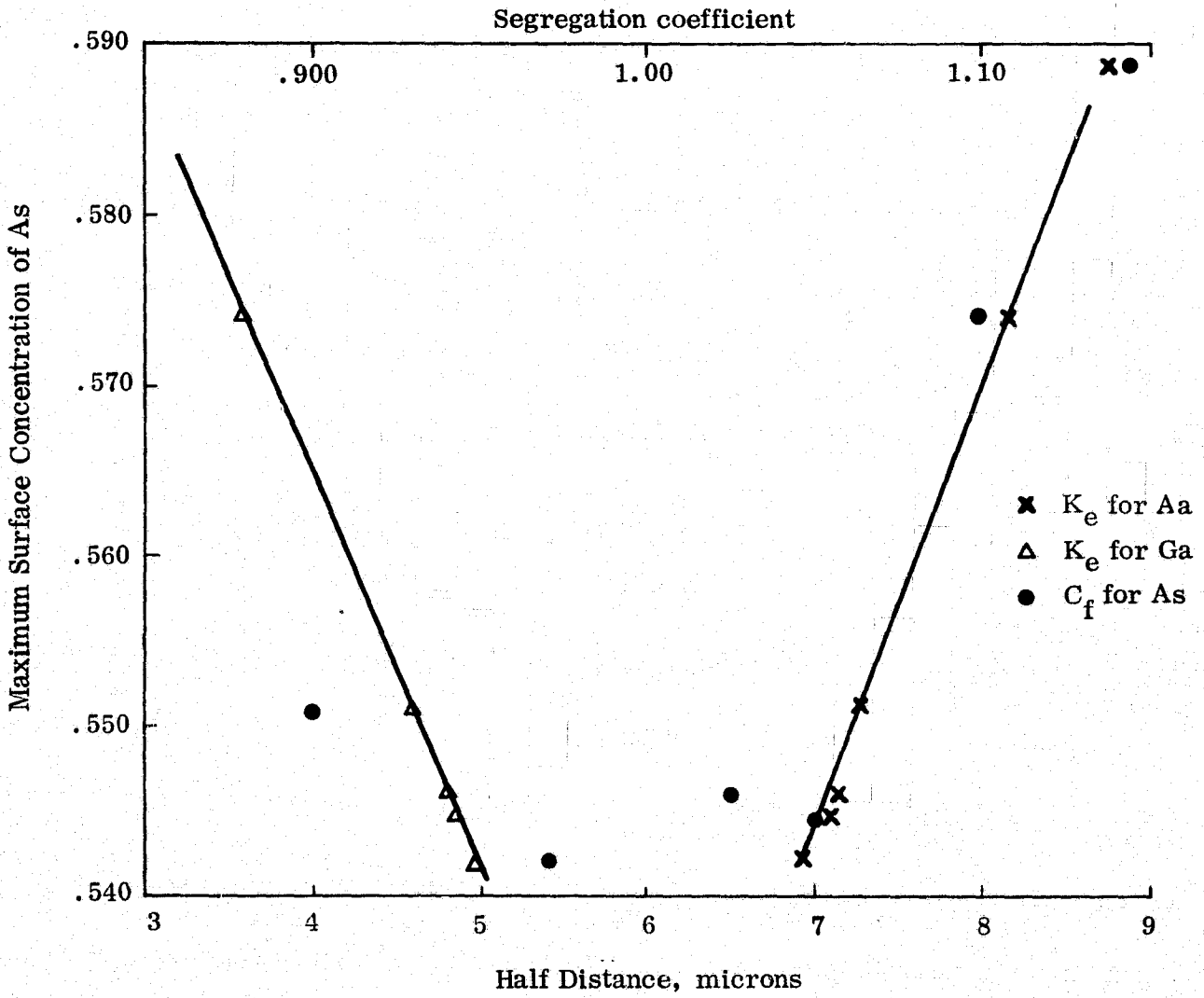

Fig. 22 Relation Between Maximum As Concentrations and Half Distance, or Effective Segregation Coefficients

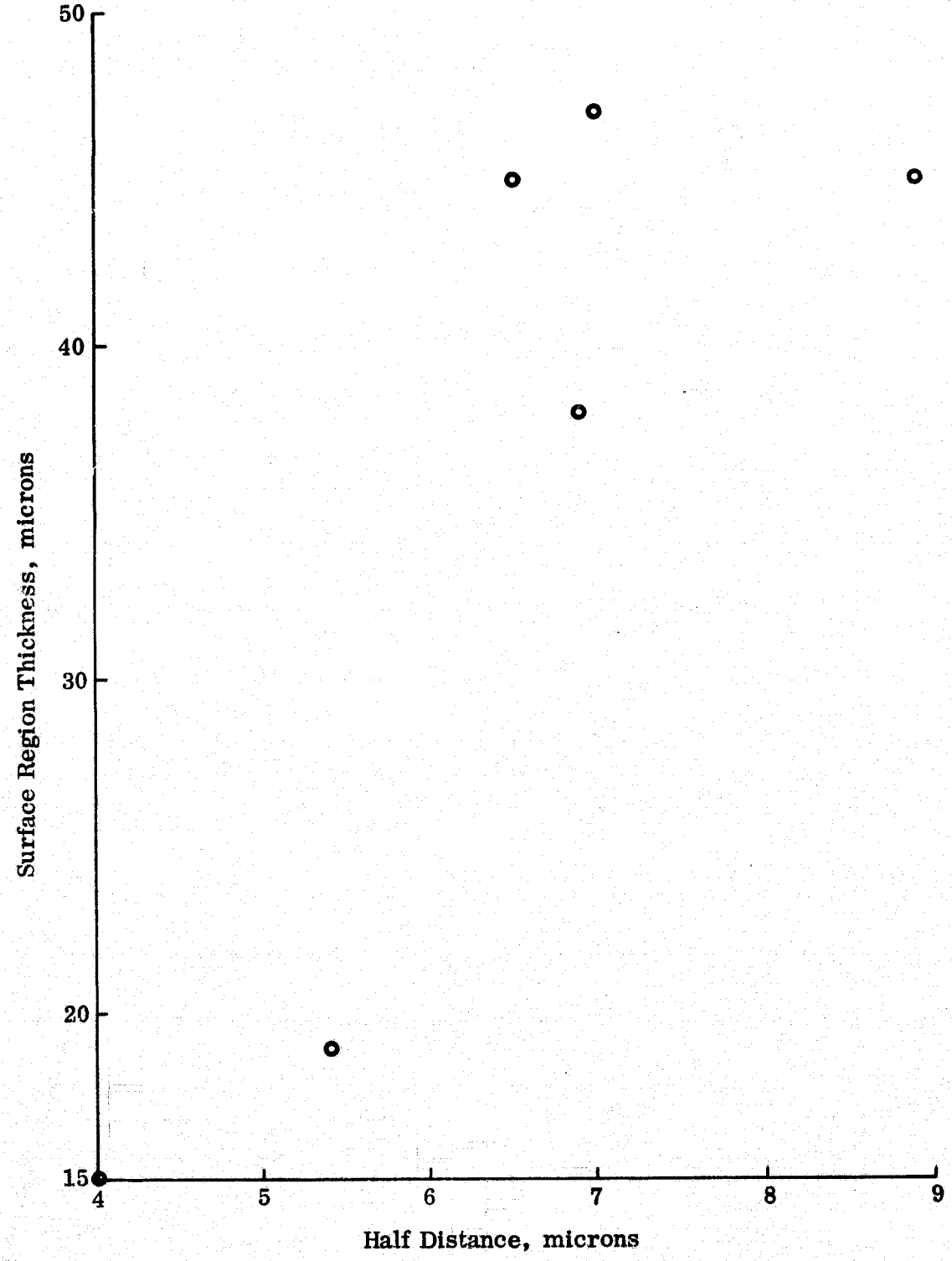

Fig. 23 Correlation Between Surface Region Thickness and Half Distance

According to Hansen's phase diagram (Fig. 24) for GaAs (Ref. 19), the liquidus curve is a single continuous line extending across the entire composition range. The tangent to the liquidus curve at the GaAs compound composition is a nearly horizontal line. There is no solidus curves except for the vertical line at the GaAs composition (See Fig. 24). There should, therefore, be no segregation due to solidification. The solid and liquid phases must be of the same composition, i.e., 50 atomic percent of Ga and 50 atomic percent of As. (or 0.482 weight fraction of Ga and 0.518 weight fraction of As).

On the basis of our segregation results, the actual phase diagram for GaAs at the peak region may look like that shown in Fig. 25. The initial GaAs melt may be slightly poorer in Ga than 50 atomic percent, e.g., 0.481 weight fraction, not as observed. Possibly, the probing accuracy is off by a substantial calibration error, even though the precision was good. The GaAs freezing out will thus follow the solidus line PG, and not PA. Ga will then be surface depleted, as observed. But the bottom of the solidus line PG must then be near 50 atomic percent (0.483 weight fraction of) Ga. The peak point P must thus be slightly off to the right of the 50:50 (atomic percent) mark.

Also, both the effective segregation coefficients (for Ga and As) are close to unity. Hence, the liquidus and solidus lines for either side of the GaAs peak must be very close at the peak, since the liquidus at the peak is nearly horizontal, the solidus lines must also be nearly horizontal. There must then be a wide spread between the two solidus lines in Fig. 25. This is also not present in the Hansen diagram (Fig. 24).

The observed As concentration was as high as 58.9 weight percent (or 57.2 atomic percent). The deviation of the solidus line PG at close to the melting point of GaAs (1511^{o}K according to Ref. 20) must be at least 7.2 atomic percent, or almost one major grid spacing on the Hansen's phase diagram (Fig. 24). Such is also not shown.

We conclude from the above that Hansen's GaAs phase diagram needs modification, to account for the observed solidification phenomen.

Let us examine more closely the relationships between the surface concentration C_f, surface region thickness d_s, half distance d/2, and effective segregation coefficients k_e. The regression between c_f and d/2 is statistically insignificant. The regression of d and d/2 is significant at the 95% level. The regression of k_e for Ga or As on c_f is significant at the 99% level.

Thus, while c_f and d/2 or d can vary independently of each other, d and d/2 can be estimated one from the other. At any location for either Ga or As, k_e can be directly computed with high confidence, once the surface concentration c_f is known by probing.

The growth velocities v from Pohl analysis (Ref. 18) show a unique trend. In particular, location 2 had the smallest velocity, followed by that at location 5, while locations 1 and 6 had the highest velocities. The high velocities at locations 1 and 6 can be explained on the basis of cooling effects of the contacting bottom at location 6, and the corner effect at location 1. But the unique velocity distribution for the other locations, 2 to 5, still deserves careful interpretation.

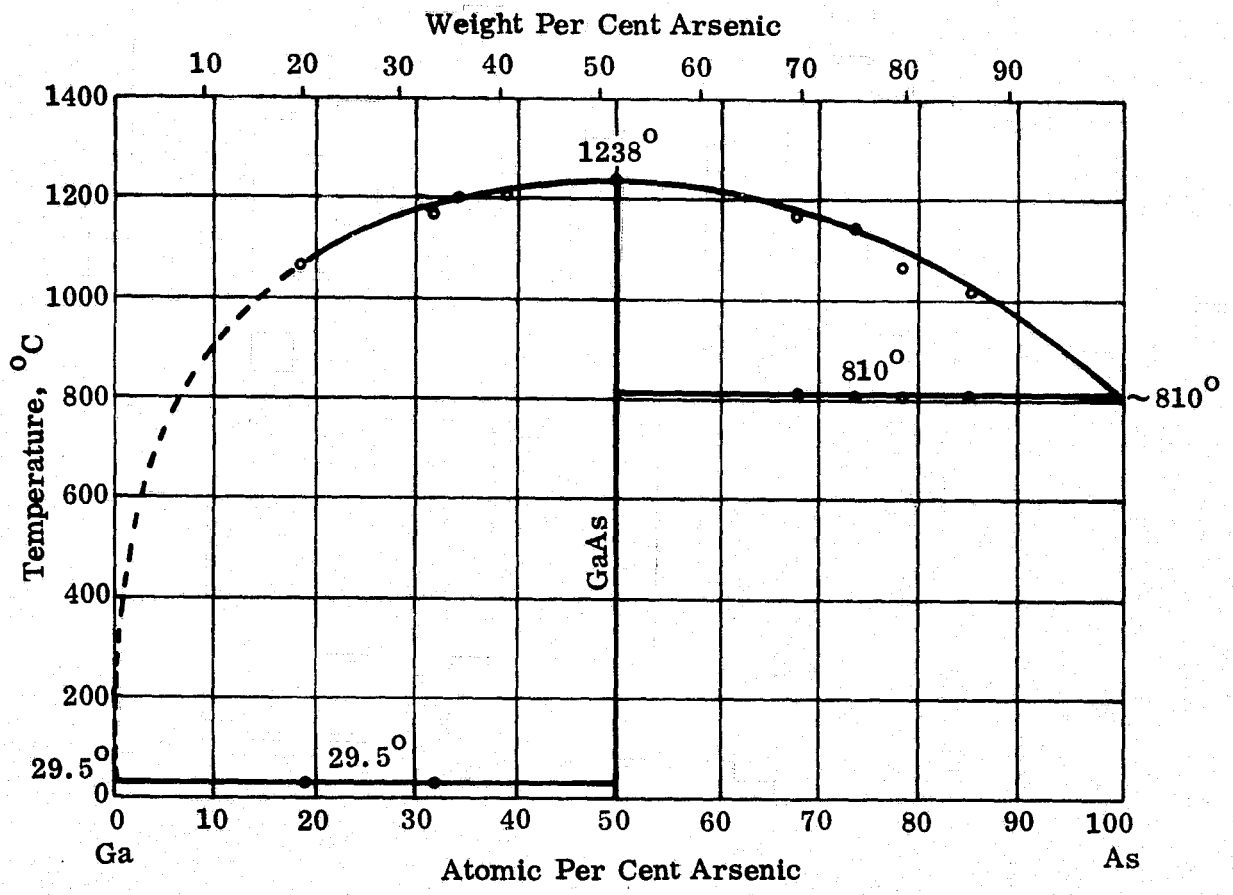

Fig. 24 As-Ga Diagram by Hansen

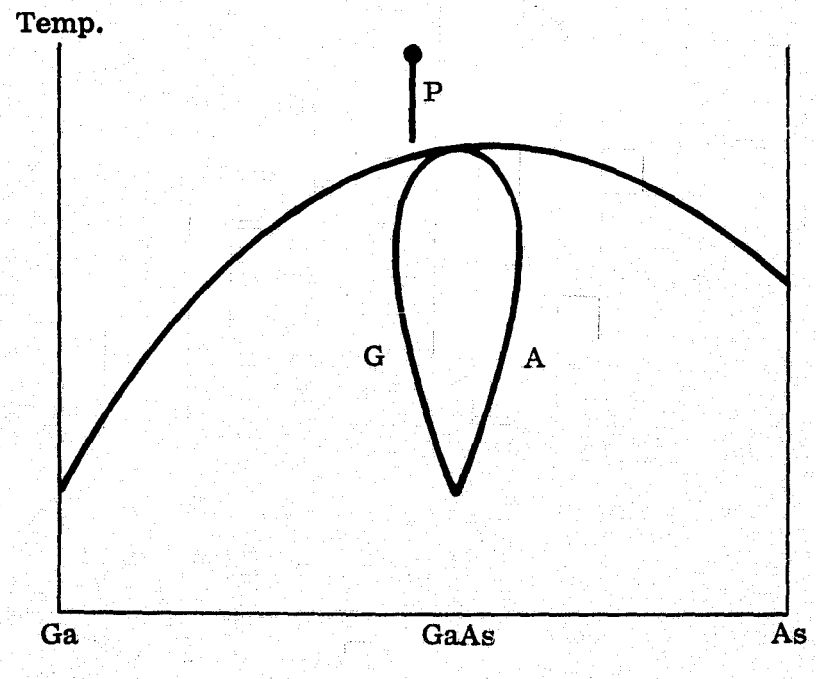

Fig. 25 Possible Phase Diagram for GaAs

Let us first review briefly the assumptions involved in the Pohl analysis (Ref. 18). Pohl assumes that the one-dimensional solidification is diffusion-limited, and that the segregation coefficient is not very large. The effect of limited stirring (due to convection, for example) can in some sense be lumped into an overall effective liquid mass transfer, whose practical results follow the Fick's first law (Ref. 21). The effective segregation coefficient, k_e, in this case is, however, close to unity, quite different from the assumed values. But the Pohl equation is still, in this particular case, better than the Tiller equation (Ref. 12) which is good only for k_e approaching zero.

In spite of these limitations, we feel that the Pohl analysis still should give some rough estimates of the localized growth velocities. The unique velocity distribution pattern must, therefore, be significant.

This unique velocity pattern can not be explained directly on the basis of thermal phenomena, such as temperature fluctuations, because then the velocities on the top surface locations should at the worst change monotonically. Such was not the case. The temperature inside the sealed quartz boat or tube was in fact very stable, because of the enclosing quartz and SiC tubes, and equidistant, spaced-apart Globar heating rods outside the SiC tubes. The thermal inertia of the SiC and quartz tubes and the surrounding ambient should have amply stabilized the temperature inside the sealed quartz boat or tube. The three-zone, temperature controllers also controlled the temperature of each zone to within about $0.5^{o}C$ of their intended values (Ref. 22).

The unique velocity distribution could not have been caused by physical or chemical processes related to the melt surface, such as oxidation, chemical reactions, or dust settling, because the velocities should then be uniform or vary monotonically from the center location 5 to the edge or corner location 1. The effect of extraneous vibrations observed (and to be described in Section 6) also could not be the cause, for similar reasons.

By this process of elimination, we thus conclude that the unique velocity distribution must be related to phenomena inside the GaAs melt, such as convection currents, as shown below.

When the furnace was slowly withdrawn, the SiC tube cools first, followed by the quartz tube, the sealed quartz tube or boat, and the GaAs melt. With temperature controls on the SiC tube the cooling must be very uniform.

The bottom (location 5) of the GaAs melt, which contacted the sealed boat, must cool fairly fast, as was observed. The corner (location 1) might have cooled equally fast, or even slightly faster, because of the combined effects of heat radiation and corner cooling. The locations 5 and 2 were probably subject to high normal fluxes of convection currents, and received heat from the interior of the hot GaAs melt. These two locations therefore cooled the slowest. This leaves the intermediate locations 4 and 3 to cool at intermediate speeds, as observed.

If this explanation proves to be correct, its implication to containerless, space processing is clear. Specifically, in zero-gravity conditions, there are no gravitational convection currents; only true diffusion operates. For a spherical geometry, there will only be a radial temperature gradient and concentration gradient. The growth velocities will be the same at all surface locations (for a simple geometry). There will be no variations in temperature, concentration, and growth velocity in directions other than radial. This definitely was not the case with our GaAs crystal growth conditions, as can be seen by comparing Fig. 16 to 21.

Not only will be the space GaAs crystals be more uniform in concentration, but the crystals will be more perfect. This is because the crystal can tolerate uniform radial shrinking stresses, but not nonradial stresses. There are several reasons for this: (1) the neighboring regions stressing each other were at different temperatures and, therefore, had different strengths; (2) absence of arch effects for nonradial stresses, and (3) higher temperature and concentration gradients introduces higher mismatch stresses.

Note that GaAs has great potential as an electronic material, but is generally found to be of lower quality than expected. The mobilities, for example, are very low, particularly in p-type materials. Usually, the mobilities in these p-type materials are only between 100 to 500 cm^2/volt-sec (Ref. 13). These poor characteristics are generally believed to be caused by imperfections. We do not know how much of these imperfections are related to convection currents. But certainly, removal of the convection-induced defects must help.

In other words, space processing, because of the absence of convection currents, might give better GaAs crystals in terms of uniformity and defect contact.

E. Summary of Conclusions

This section describes some results of microprobing work on GaAs crystal samples. We find that:

1. Probing gave Ga and As concentrations precise to ±0.0005 in weight fractions.
2. The bulk of the original GaAs melt had a Ga concentration of 0.483 weight fraction (50.09 atomic percent) and As concentration of 0.517 weight fraction (49.91 atomic percent).
3. There was significant Ga depletion and As enrichment on the surfaces of from 15 to 47 microns thick. Average surface concentrations were: Ga - 44.22 weight percent 54.00 atomic percent) and As - 55.78 weight percent (46.00 atomic %).
4. These segregations are real, because of the small probing errors.
5. These segregations could not be caused by evaporation, but must be caused by solidification.
6. On solidification, Ga segregated with an average effective segregation coefficient of 0.9155, and As with an average effective segregation coefficients of 1.079.
7. These segregation coefficients k_e are not anticipated, at least according to Hansen's phase diagram on GaAs.
8. The half distances, or depth to average concentrations, varied from 4.0 to 8.9 microns, with an average of 6.45 microns.
9. The surface concentration (of either Ga or As) did not correlate with the half distances d/2.

10. The surface region thickness d_s correlated significantly (95%) with, and could be predicted from, d/2. The prediction equation is:

$$d_s \text{ (microns)} = -11.95 + 7.253 \times d/2 \text{ (microns)} \pm 8.55$$

11. The effective segregation coefficients k_e can almost be exactly calculated from the surface concentrations alone:

$$k_e \text{ for As} = 1.936\ C_f$$

$$k_e \text{ for Ga} = -0.084 - 2.064\ C_f$$

12. The growth velocities at different locations have been estimated by a Pohl analysis. These velocities varied from 0.180 to 0.775 cm/sec. These initial velocities apply only to the surface regions (15 to 47 microns thick).

13. The melt interface probably was concave toward the liquid.

14. Hansen's GaAs phase diagram probably needs modification.

15. These growth velocities have a unique distribution pattern which can not be explained on the basis of furnace temperature, surface reactions, dust settling, vibration, or other causes external to the GaAs melt. The presence of a gravitational convection current, however, quite satisfactorily explains this velocity distribution pattern.

16. In space, there is little gravitational convection current. There should be no temperature, concentration and stress gradients in the nonradial directions. The stress pattern will be relatively simple and readily tolerated. More uniform and defect-free GaAs crystals will, therefore, be grown in space.

6. VIBRATION EFFECTS ON CRYSTAL GROWTH

Our vendor, the Materials Research Corporation of Orangeburg, New York, in growing the 14 GaAs crystals for our statistically designed experiment, noted that a damaged and unbalanced scan motor (used for moving the horizontal Bridgeman Furnace) actually improved the yield of single crystals. "Yield" as used here means the proportion in a growth run of crystals which are completely single crystalline over the entire length of about 2 feet. The location of this motor on the furnace is shown in Fig. 26.

That the yield was improved was convincingly shown by distinct improvements whenever this motor was switched back and forth from one furnace to another of identical design. Data comparing the yield with the unbalanced motor to the yield with a balanced motor as control are given in Table 18. These data on GaAs crystal growth (Ref. 22) are for two identically designed furnaces during three successive growth periods, or runs 1 to 3, after the motor was unbalanced due to accidental damage and the unusual effects of this damaged motor were noted. For example, during growth period 1, furnace 3 was with the unbalanced motor and had three completely single crystals out of four grown. Simultaneously, furnace 10 had the balanced motor and yielded no completely single crystals out of six tried.

Table 18. GaAs Yield Data Comparing Motors, Furnaces, and Growth Periods

Growth Period	Furnace 3	Furnace 10
1	Unbalanced motor; yield 3/4	Balanced motor; yield 0/6
2	Balanced motor; yield 0/3	Unbalanced motor; yield 3/3
3	Unbalanced motor; yield 3/3	Balanced motor; yield 1/5

It can be shown that such results are statistically significant (Ref. 23). That is the unbalanced motor markedly improved the yield of completely single-crystalline GaAs crystals, on both furnace 3 and furnace 10, for all periods 1 to 3.

Systematic work on the effect of vibration during crystal growth is seldom documented and studied in detail. According to Dr. R. A. Laudise, Assistant Director, Materials Research Laboratory of the Bell Telephone Laboratories, no systematic work has been done on the effects of vibration on crystal growth, nor does he know of any current work in this area at other laboratories (Ref. 24). In some previous MIT work (Ref. 25), vibrations of varying frequencies were introduced to the crystal grower, without any appreciable effect being noticed at any frequency.

A. Relation of Vibration Effects to Low-G Crystal Growth

Vibrations may have beneficial or harmful effects on crystal yield. We hypothesize that the vibration effects we observed probably have to do with liquid mixing or mass transfer ahead of the solid-liquid interface. Some Skylab experiments also pointed to reduced liquid mixing and effective solute transfer as a most important zero-gravity segregation effect, according to E. McKannon, A. Ukanwa, and T. Bannister (Ref. 10). We have, therefore, taken a close look at vibration effects during GaAs crystal growth.

We arrived at the above hypothesis through a process of elimination, even though detailed thermal, metallurgical, mechanical, and thermodynamic analyses have not been made.

A notable possible effect of vibration to crystal growth is to change the instantaneous growth rate by, e.g., momentarily perturbing the temperature or temperature gradient through adiabatic expansion and cooling at the solid-liquid interface. Another possible effect of vibration is to modify the instantaneous solute concentration through localized and periodically varying (non-symmetric), artificial gravity effects due to density differences between the solute and solvent melt. When the instantaneous growth velocity, temperature gradient, or solute concentration, separately or in combination, exceeds the critical limits, constitutional supercooling and polycrystalline growth result. But since the vibrations from the unbalanced motor is only of the milli-g level, as will be shown, they should have relatively negligible effects, particularly when compared to the effects of unavoidable, fractional degree temperature fluctuations always present in the melt. There may also be a boundary layer that damp these effects through mechanical or thermal inertia effects. For similar reasons, the periodic tensile and compressive or shear forces at the interface can be also ruled out. It has been estimated that the effect of applying 100,000 psi in some respects is equal to a change in melt temperature of only $0.3^{o}C$ (Refs. 26-28). Such temperature fluctuations are inherent in the furnaces.

Vibration may also force the liquid melt to make better contact with the wall of the quartz tube, at least for ultrasonic welding or soldering operations. But the frequency and the milli-g forces are again probably too low to be very effective. In addition, this effect of vibration will introduce additional nuclei and is opposite to what happened. Another possible vibration effect is to precipitate nuclei in the GaAs melts saturated or nearly saturated with some unknown impurities. But again this should result in nucleation, and not denucleation, as was probably observed.

We can also assume that the GaAs melt contained refractory, particulates that could act as nuclei for polycrystalline growth. Such particles may, for example, be dust particles or grains from the quartz tube (Ref 29). These particles must, in addition, be difficult to dissolve in, or wet by, the GaAs melt. Vibrations, however, enhanced the wetting and dissolution, thereby achieving denucleation (Ref. 30). However, the milli-g forces at the particular frequencies are probably too small or incorrect to achieve these results.

The most plausible mechanism, we believe, is as follows: Vibration introduced some additional mixing effects in the liquid ahead of the interface. A controlled, milli-g, vibrative force might have introduced a gentle "massaging" action into the liquid. The longitudinal vibrations (along the axis of the quartz growth tube) increased the longitudinal, effective liquid mass transfer and reduced the likelihood of longitudinal, constitutional supercooling. Transverse vibrations (perpendicular to the growth tube axis) increased the transverse, effective liquid mass transfer and reduced transverse solute concentration gradients and constitutional supercoolings. In either case, polycrystalline growth is supressed, as was observed.

Crystal growth is generally still an art. Growth defects often appear and disappear mysteriously. In particular, many crystals uncontrollably go polycrystalline.

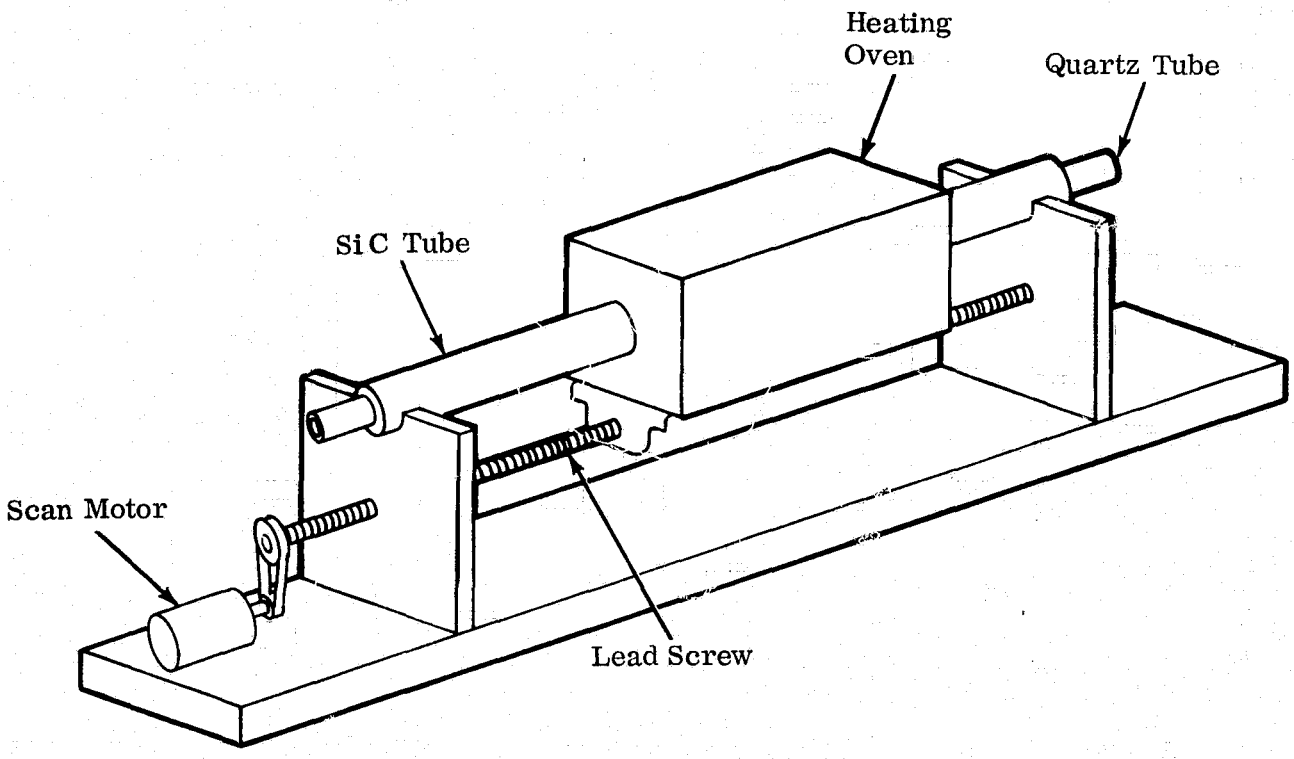

Fig. 26 Schematic of Typical Furnace

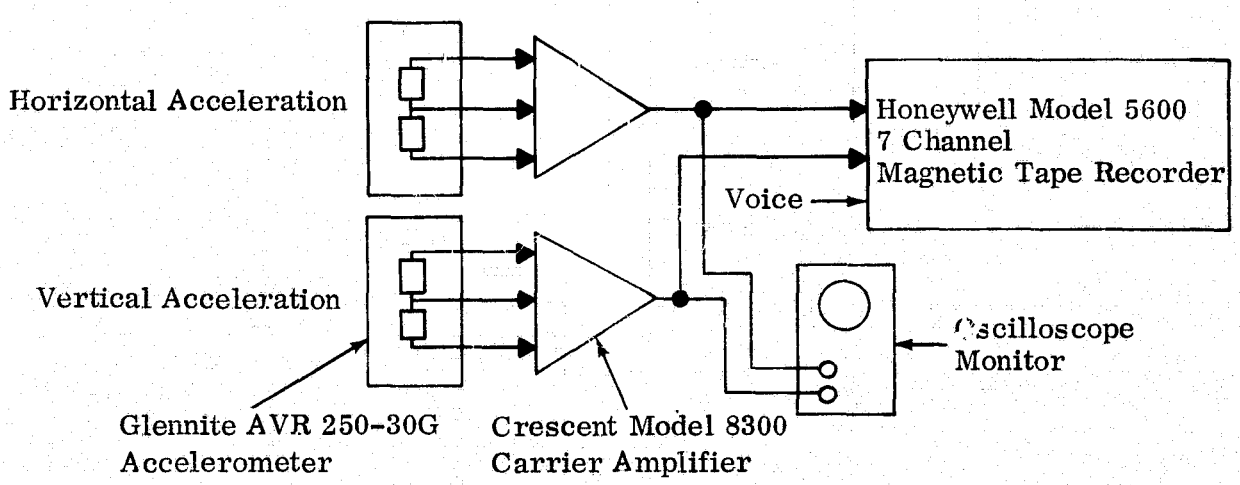

Fig. 27 Instrumentation for Recording Furnace Vibrations

Yet without good crystals, modern electronics would not have been developed and many other physical and metallurgical discoveries would not have been made. Many electrical, optical, and mechanical structures are still material limited. It would thus appear that efforts should be spent to follow up on significant leads related to crystal growth and quality improvement. In addition, the space environment may provide unique conditions that may lead to improved growth techniques or theoretical understandings, as will be shown in the discussion of this vibration work. We have undertaken a study to determine exactly what happened due to the vibrations from the unbalanced motor.

B. Experimental Detail

We simultaneously measured the vibrations in the horizontal and vertical directions with Glennite AUR 250-30G accelerometers, together with Model 8300 Crescent amplifiers and an oscilloscope for instant visual observations. The amplified vibration signals were recorded with a Honeywell Model 5600 tape recorder on 1/2 inch magnetic tapes operating at 60 inches/sec in the FM mode. Figure 27 shows the instrument set-up.

Five critical points in the furnace were selected for the vertical and horizontal vibration measurements. These points are given below and are marked "X" in Fig. 28.

1. On scan motor
2. On aluminum chain block supporting the lead screw
3. On SiC tube supporting the quartz tube
4. In quartz boat inside the quartz tube at the seed location
5. On heating oven for quartz tube.

The Glennite accelerometers together with the Crescent amplifiers have a combined sensitivity of about 1.5 volts DC per g (gravitational constant), and a linearity of ± 0.25% of full scale. The frequency response of the amplifiers is -3 dB at 300 Hz and -12.5 dB at 10^3 Hz. The noise content in the output is 10 mV which is equivalent to 0.0069 g.

Under the operating conditions given above, the bandwidth of the recorder is 10^4 Hz with a signal to noise ratio of 49 dB. The noise output of the recorder is equivalent to 0.0035 g. An additional channel in the recorder was used for voice identification of each run which insured positive identification of the data during playback. An oscilloscope, used to monitor the signals being recorded, identified any overloads or malfunctions of the equipment during recording, and provided a check on the overall input-output characteristics of the recorder.

Before making a tape recording, either furnace 3 or furnace 10 and the recording point on it were selected. In all runs furnace 3 had the unbalanced scan motor, while furnace 10 had the balanced or control motor. The unbalanced motor could simply be turned on or off. The balanced motor, on the other hand, could not only be turned on or off, but also be adjusted to different voltage settings to change its rotating speed.

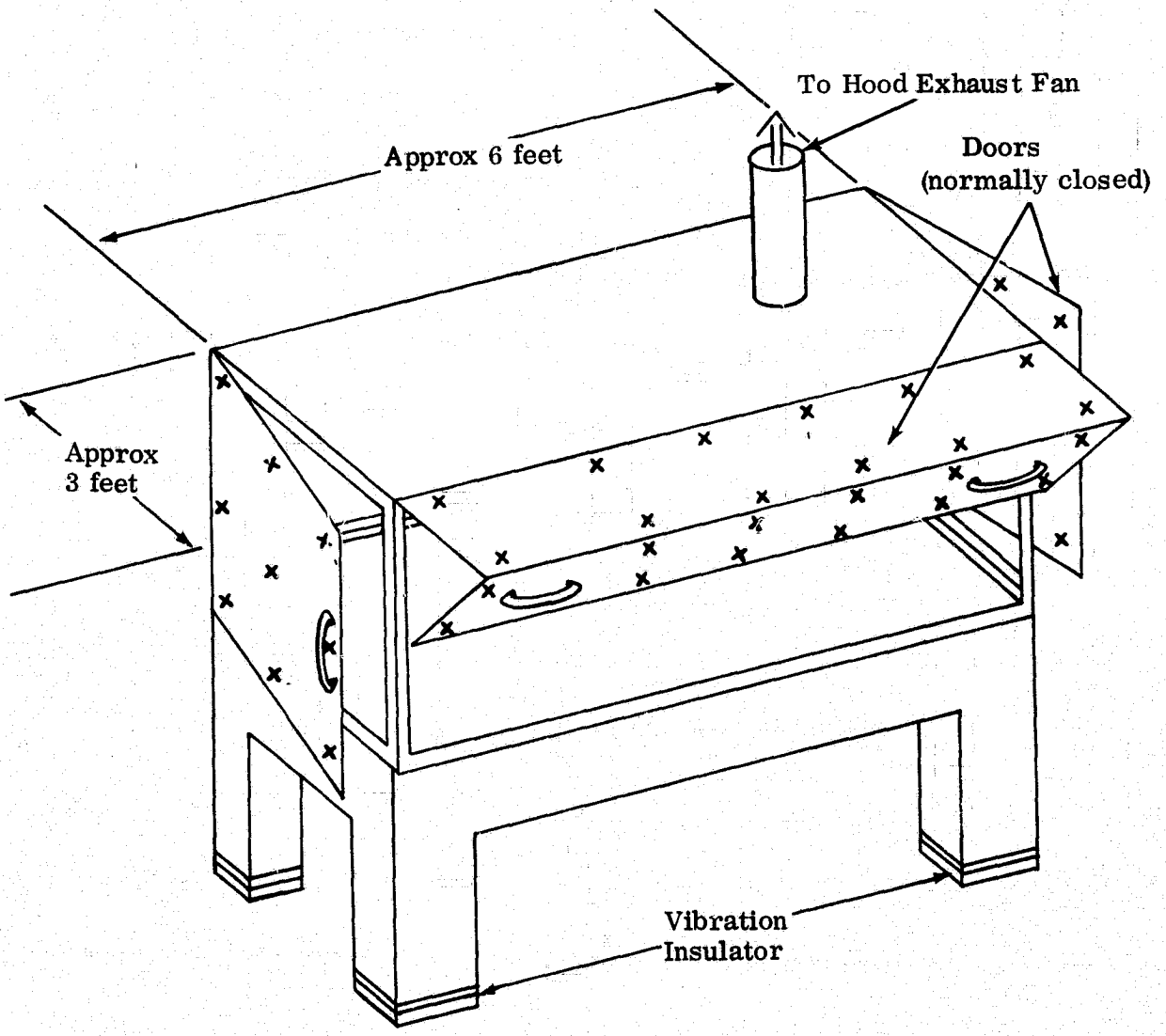

Fig. 28 Furnance Enclosure

Furnace 3 had the cooling fan for the electronic temperature circuit in operation, but furnace 10 had the same cooling fan removed for repair during the time of measurement.

The background noises were first recorded. The several motors on the furnace or in the room were then (selectively or) successively turned on. In general, the order of turning on the motors were: cooling fan, heater fan (for room heating), hood fan (for furnace exhaust), and scan motor (for furnace driving relative to the stationary quartz boat containing the GaAs melt for growth). Each motor was turned on for 30 seconds before the next motor was activated, except for the scan motors, which were turned on for one minute intervals. After the last or scan motor was on for one minute, it was turned off, followed by the successive turning off of the other motors in the reverse order at 30 second intervals.

In Run 6, the end doors of the furnace hood (Fig. 28) were tapped with the middle finger, successively but in order, at locations marked "X" in Fig. 28. Some time was also spent waiting for a freight train to pass (within 200 feet). This allowed us to record the vibrations due to the passing train in Run 11.

C. Data and Data Analyses

1. Data:

Altogether, 16 recording runs were made on four reels of magnetic tape. The contents of the recorded tapes are given in Table 19.

2. Oscilloscope Pictures:

The oscilloscope photos were made by playing back the magnetic tapes on the Honeywell Model 5600 tape recorder connected to an oscilloscope (Tektronix 545). The vertical and horizontal signals were individually amplified before being fed simultaneously to the oscilloscope. Each oscilloscope photo thus contains two signals in the form of two wavy lines. The top line is for the vertical signal, while the lower one for the horizontal signal. On those photographs having 1/9 g per cm display, the noise component due to the instrumentation is about 0.07 cm, or 0.0008 g.

Figures 29a through 29e, from Run 7, are oscilloscope photos of the vibration signals inside the quartz tube (at the seeding plane) of furnace 3. They are, respectively, for background noise, cooling fan on, heater fan on, hood fan on, and scan motor on. The hood fan introduced some vibrations, mostly in the vertical direction (0.06 g). The unbalanced scan motor, however, introduced both vertical and horizontal vibrations of far greater magnitude (0.10 g).

Figures 30a through 30d, from Run 8, are oscilloscope photos of the vibration signals inside the quartz tube but on furnace 10. They are, respectively, for background noise, heater fan on, hood fan on, and (balanced) scan motor on. The balanced scan motor did not seem to introduce any significant vibrations, in either the vertical or horizontal direction.

Figures 31a through 31d, from Run 5, are oscilloscope photos of the vibration signals on the SiC tube on furnace 3, respectively for background with cooling fan on, heater fan on, hood fan on, and scan motor on. By comparison with Figures 29a-29e,

Table 19 Vibration Signals on GaAs Furnaces as Recorded

Reel No.	Run No.	Furnace No.	Record Point	Notes
1	1	3	SiC tube	Background--30 secs recorded
1	2	3	SiC tube	Heater fan only on--30 sec
1	3	3	SiC tube	Hood fan only on--30 sec
1	4	3	SiC tube	Scan motor and hood fan on--30 sec
1	5	3	SiC tube	Cooling fan on--30 sec Heater fan on--30 sec Hood fan on--30 sec Scan motor on--60 sec Scan motor off--30 sec Hood fan off--30 sec Heater fan off--30 sec Cooling fan off--30 sec
2	6	3	SiC tube	Tapping three hood doors, Side doors 9 times each, front door 20 times
2	7	3	Quartz boat	Background--30 sec Cooling fan on--30 sec Heater fan on--30 sec Hood fan on--30 sec Scan motor on--60 sec Scan motor off--30 sec Hood fan off--30 sec Heater fan off--30 sec Cooling fan off--30 sec
2	8	10	Quartz boat	Background--30 sec Heater fan on--30 sec Hood fan on--60 sec Scan motor at 5 mv--30 sec Scan motor at 10 mv--30 sec Scan motor at 15 mv--30 sec Scan motor off--30 sec Hood fan off--30 sec Heater fan off--30 sec
3	9	3	SiC tube	Background--30 sec Cooling fan on--30 sec Heater fan on--30 sec Hood fan on--30 sec Scan motor on--60 sec Scan motor off--30 sec Hood fan off--30 sec Heater fan off--30 sec Cooling fan off--30 sec
3	10	3	On Scan motor	Background--30 sec Cooling fan on--30 sec

Table 19 Vibration Signals on GaAs Furnaces as Recorded (Continued)

Reel No.	Run No.	Furnace No.	Record Point	Notes
				Scan motor on--60 sec
				Scan motor off--30 sec
				Cooling fan off--30 sec
3	11	3	Chain block	Passing freight train within 200 feet
3	12	3	Chain block	Background--30 sec
				Cooling fan on--30 sec
				Scan motor on--60 sec
				Scan motor off--30 sec
				Cooling fan off--30 sec
4	13	3	Chain block	Background--30 sec
				Cooling fan on--30 sec
				Scan motor on--30 sec
				Scan motor off--60 sec
				Cooling fan off--30 sec
4	14	3	SiC tube	Background--30 sec
				Cooling fan on--30 sec
				Scan motor on--60 sec
				Scan motor off--30 sec
				Cooling fan off--30 sec
4	15	3	On furnace	Background--30 sec
				Cooling fan on--30 sec
				Scan motor on--60 sec
				Scan motor off--30 sec
				Cooling fan off--30 sec

Figures 33a and 33b, from Runs 12 and 10, show respectively the vibrations on the aluminum, support chain block and directly on the scan motor of furnace 3. By comparing these two photos with Figs. 29e and 31d, one notices that, as expected, the vibrations grew stronger as the recording point was shifted from inside the quartz tube (Fig. 29e), through the SiC tube (Fig. 31d) and chain block (Fig. 33a), to directly on the scan motor (Fig. 33b). Tapped end doors vibrated even more strongly (Fig. 29f).

Figure 34, from Run 11, shows that no additional noises were introduced on chain block of furnace 3 by a freight train passing within 200 feet.

D. Computer Signal Analyses

The recorded vibration signals on the magnetic tapes were played back onto an Adage Ambilog computer for Fourier analyses of the spectrum distribution, power spectral density (PSD), autocorrelation, and cross-correlation. The Honeywell tape recorder was again used, to play back the signals at a rate of 3×10^3 samples per second for storage in a buffer storage unit of 4×10^3 capacity. When the data buffers were filled, each channel was unbiased by subtracting its means and then unitized by dividing by its maximum value. The PSD function of each series was then calculated and stored in the spectrum buffer, and subsequently read out and automatically plotted

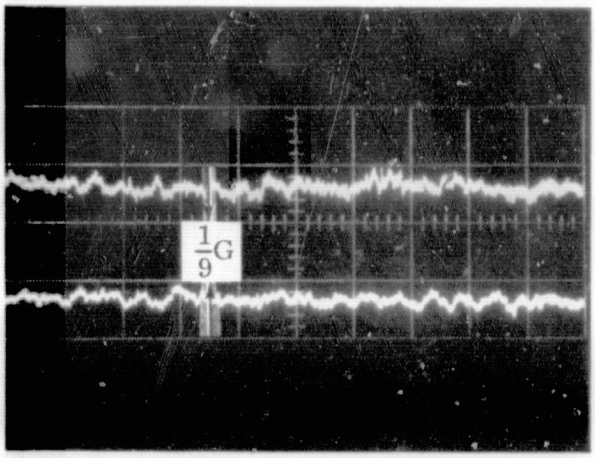

a - Background

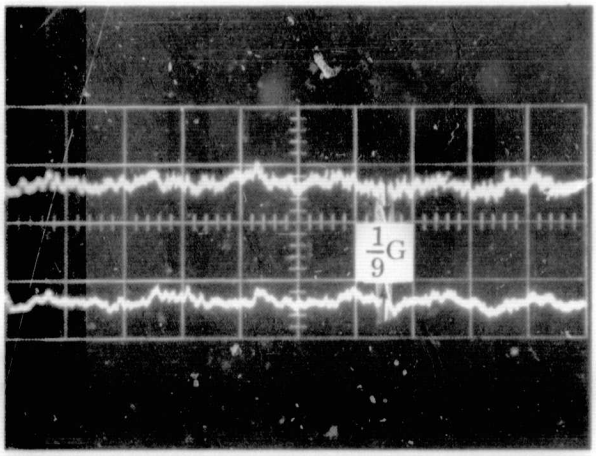

b - Heater Fan On

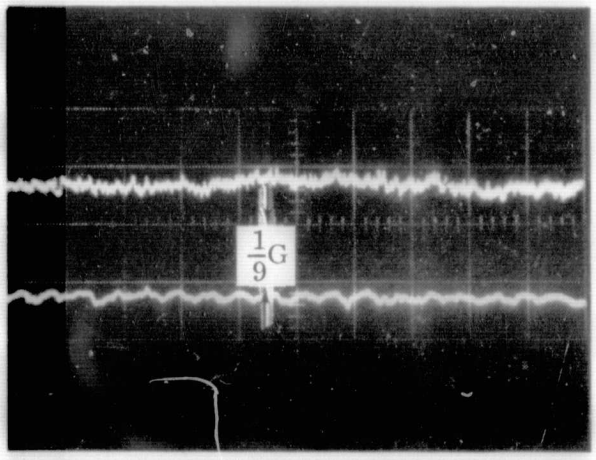

c - Cooling Fan On

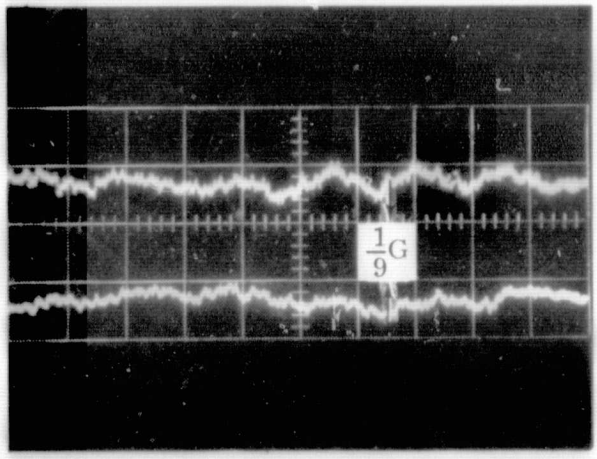

d - Hood Fan On

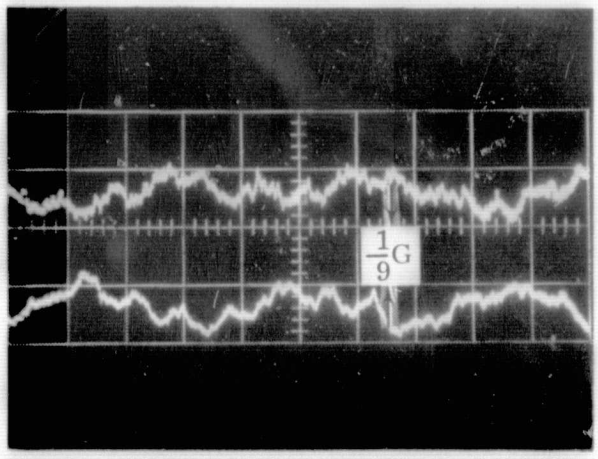

e - Scan Motor On

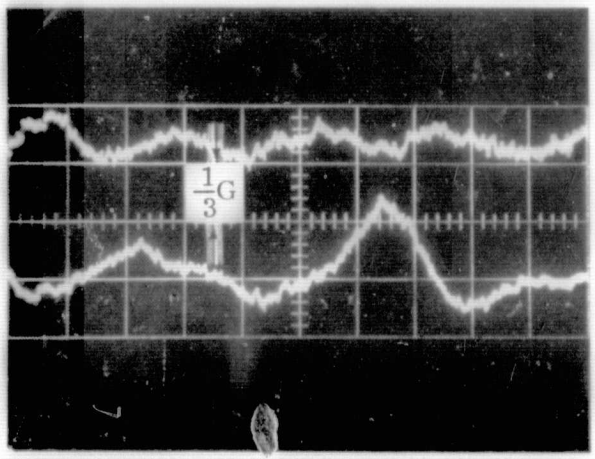

f - End Door Tapped

Fig. 29 Vibrations on SiC Tube of Furnance No. 3

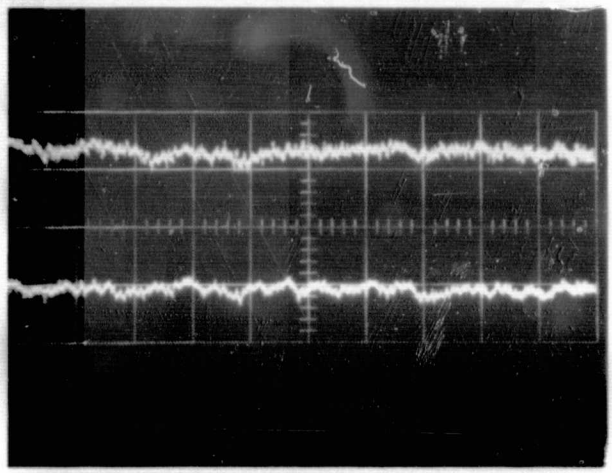

a - Background

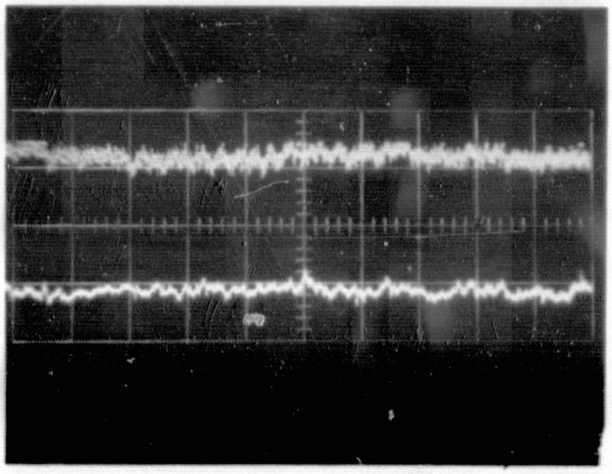

b - Heater Fan On

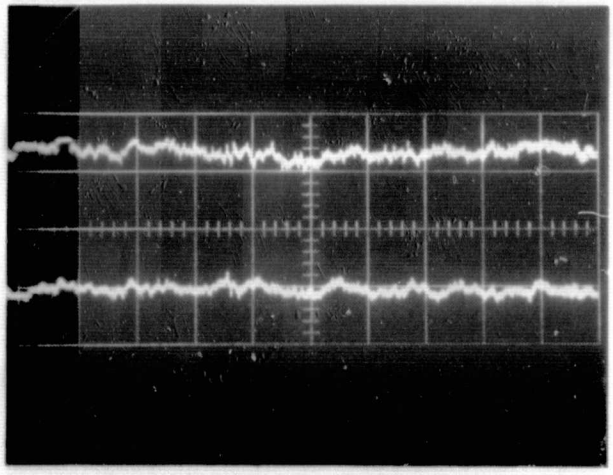

c - Hood Fan On

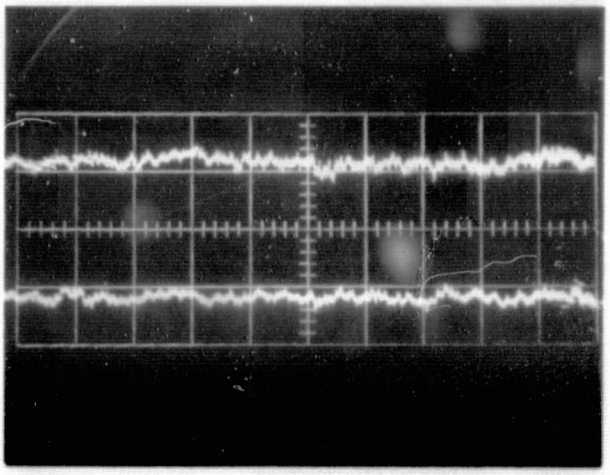

d - Scan Motor On

Fig. 30 Vibrations Inside Quartz Tube on Furnace 10

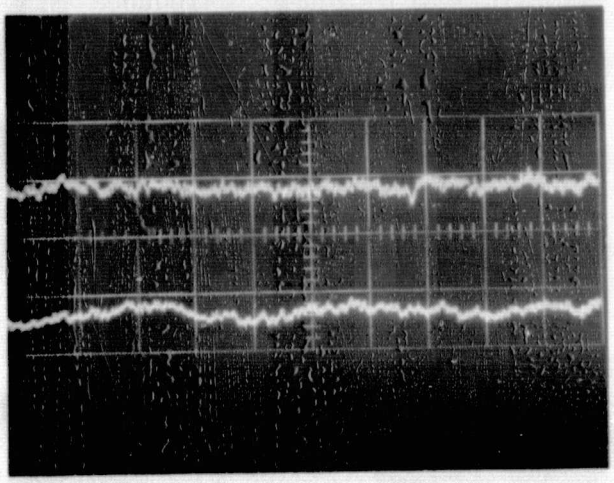

a - Background

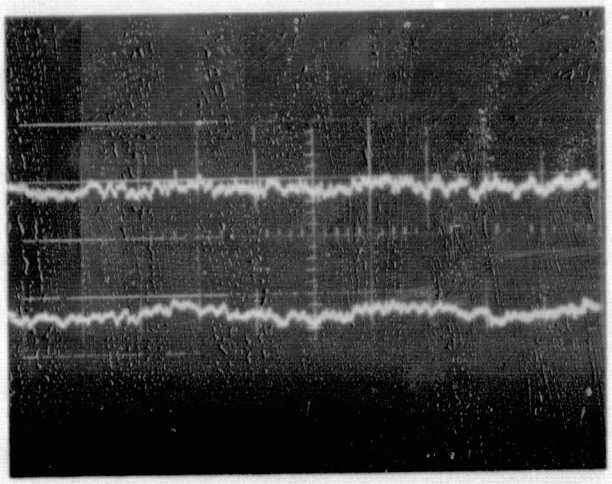

b - Heater Fan On

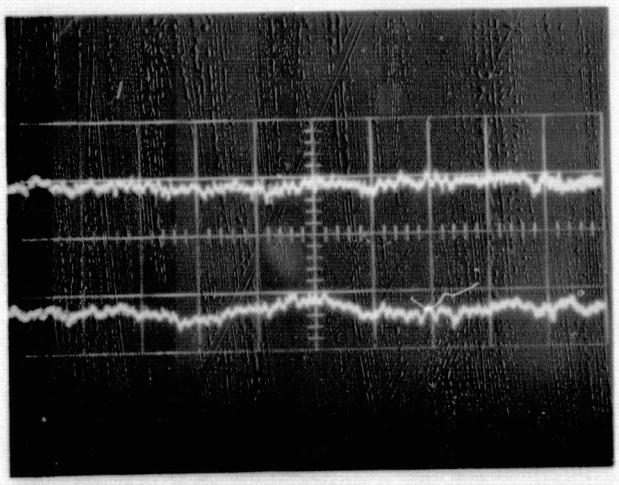

c - Hood Fan On

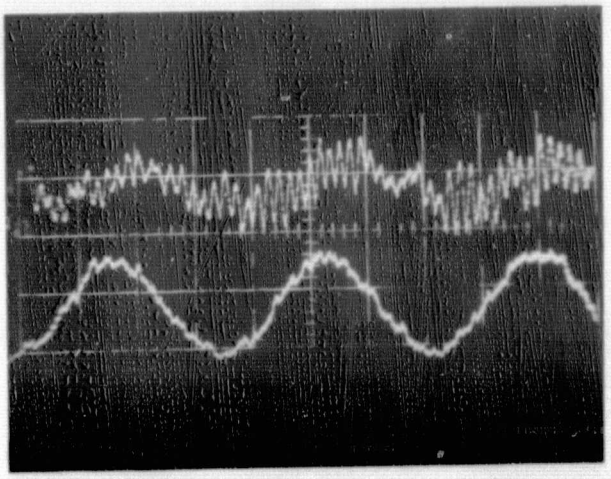

d - Scan Motor On

Fig. 31 Vibrations on SiC Tube of Furnance 3

the horizontal background noise appeared to be slightly increased. But the greatest differences between these sets of pictures are observed in the vibrations introduced by the unbalanced scan motor. The amplitude in the horizontal direction is almost doubled. The vertical vibration signal also increased in amplitudes, particularly in the secondary vibrations of higher frequencies.

Figures 32a through 32c, from Run 6, show that tapping the end doors at locations marked as "X" in Fig. 28 introduced severe vibrations on the SiC tube on furnace 3. Note that the vertical scale on these photos is 0.111 g/cm, rather than 0.037 g/cm as in all the other pictures (Figs. 29, 30, 31 and 32). Also, the horizontal vibration signals were about 2-1/2 times stronger than the vertical signals. Figure 32a also shows some transient behavior of the vibration in the horizontal direction.

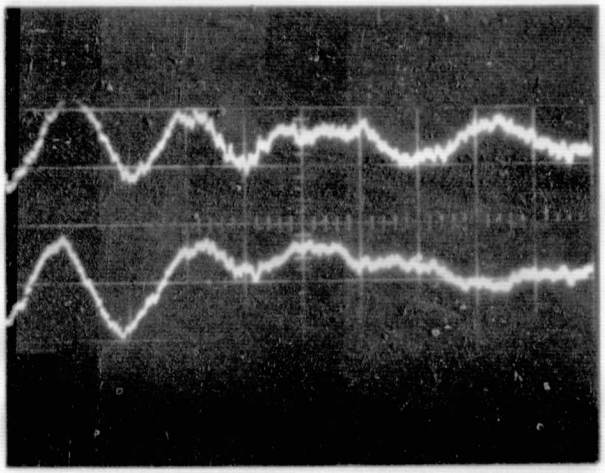

a - Tap End Door

30 x gain
5V/cm
1.5 v/G

$$\frac{5V}{cm} \times \frac{G}{1.5V} \times \frac{1}{30} = \frac{1}{9} = 0.111 \frac{G}{cm}$$

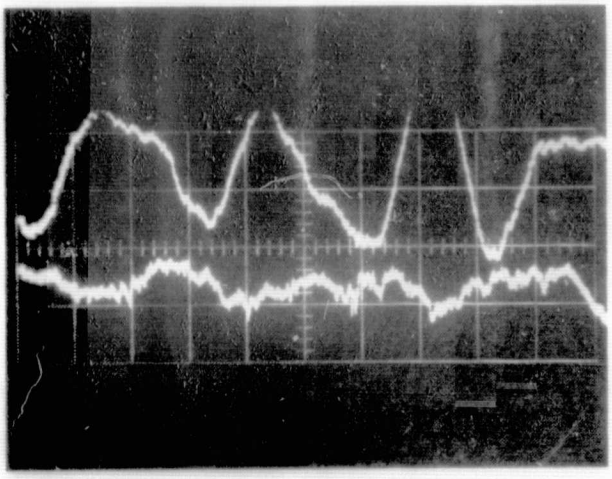

b - Tap End Door
0.111 G/cm

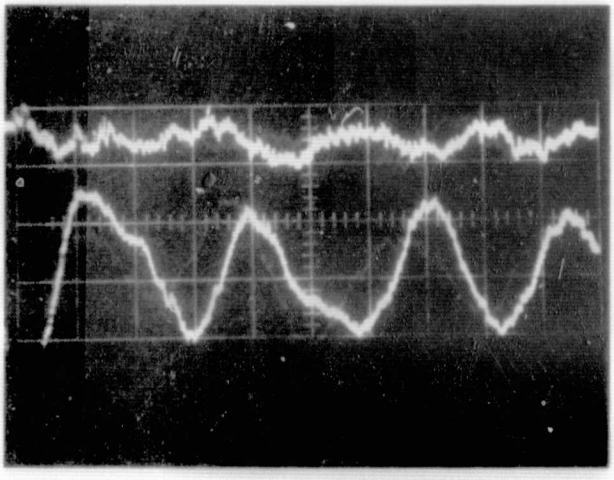

c - Tap End Door
0.111 G/cm

Fig. 32 Vibrations Due to Tapping on Sic Tube of Furnace 3

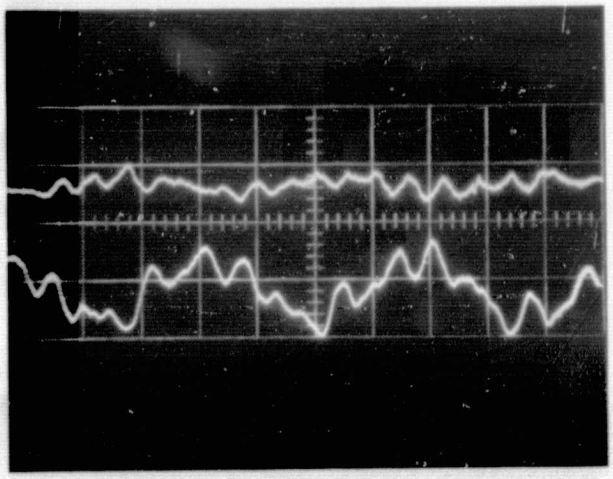

a - Vibrations on Chain Block

Fig. 33 Vibrations Due to Scan Motor of Furnace 3

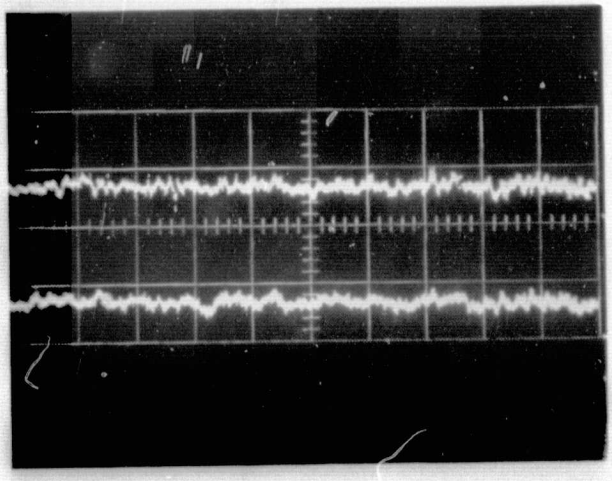

Fig. 34 Vibrations Due to Passing Freight Train on Chain Block of Furnace 3

by a digital plotter. Figures 35 to 56 are examples of the PSD analyses of some of the vibrations recorded. The vertical ordinate in all these figures is proportional to the squared amplitude of the signal (e.g., g^2) while the horizontal abscissa indicates the frequency of the signal.

By putting both square and sine waves of three different amplitudes each, we proved that the vertical ordinate on the PSD curves are proportional to the applied signals (or voltages) squared. Since we know the applied voltage is proportional to the acceleration force , (in g's), the vertical ordinate can thus be calibrated into g^2. This has been done for each PSD curve, as is shown in the figures.

Figures 35-44 show, in subgroups of two for the vertical and horizontal signals, the computer-plotted, PSD analyses of the vibration signals recorded on the quartz boat inside furnace 3. These figures are, in order: background noise; cooling fan on; heater and cooling fans on; hood, heater, and cooling fans on; and scan motor, and hood, heater, and cooling fans on. The background noises peaked at about 30 Hz in the vertical directions (Fig. 35), while the horizontal signal peaked at about 55 Hz (Fig. 36). The cooling fan did not appreciably change the vibration spectra, either in the vertical or in the horizontal directions (Figs. 37 and 38). The heater fan did, however, introduce at least one new vibration spectrum with a peak at 50 Hz in the vertical direction (Fig. 39), which is higher than the 30 Hz vertical background noise, but no appreciable horizontal peak (Fig. 40). The hood fan noises peaked at 123 Hz, both in the vertical and horizontal directions (Figs. 41 and 42). The scan motor introduced at least two additional peaks, a strong peak at 54 Hz, which is much stronger than the hood or other noises, and a weaker peak at 247 Hz (Figs. 43 and 44).

Figures 45 to 53 show similar results of PSD analyses of the recorded vibration signals, but for furnace 10 with a balanced motor. The background noise here peaked at 120 Hz, both in the vertical and horizontal directions (Figs. 45 and 46). Neither the cooling fan (Fig. 47) nor the heater fan (Figs. 48 and 49) contributed much vibration signal. The hood fan did, however, introduce at least one additional strong signal at 123 Hz, with the vertical signal being much stronger than the background (Fig. 50), but the horizontal signal being weaker than the background (Fig. 51). The scan motor noises peaked at 28 Hz in both directions. (Fig. 52 and 53).

Figure 54 shows the PSD analyses of the vibration signals on the SiC tube of furnace 3, with the scan motor, hood fan, heater fan, and cooling fan on. The signals of the scan motor again predominated at, as expected, 54 Hz.

Figures 55 and 56 show the effect of tapping the end doors. The strong tapping signals peaked at 110 Hz.

Table 20 summarizes the results of PSD analyses of the above vibration signals and gives such statistical data as average signal density, maximum signal density, and standard deviation of the spectra for each case. The peak accelerations (in g) and the frequence of the peaks are also given.

Figure 57 exemplifies an autocorrelation analysis of the vibration signal in the vertical direction, as recorded on the SiC tube of furnace 3, with the scan motor, hood fan, heater fan, and cooling fan on; 2,000 data points were included in the analysis.

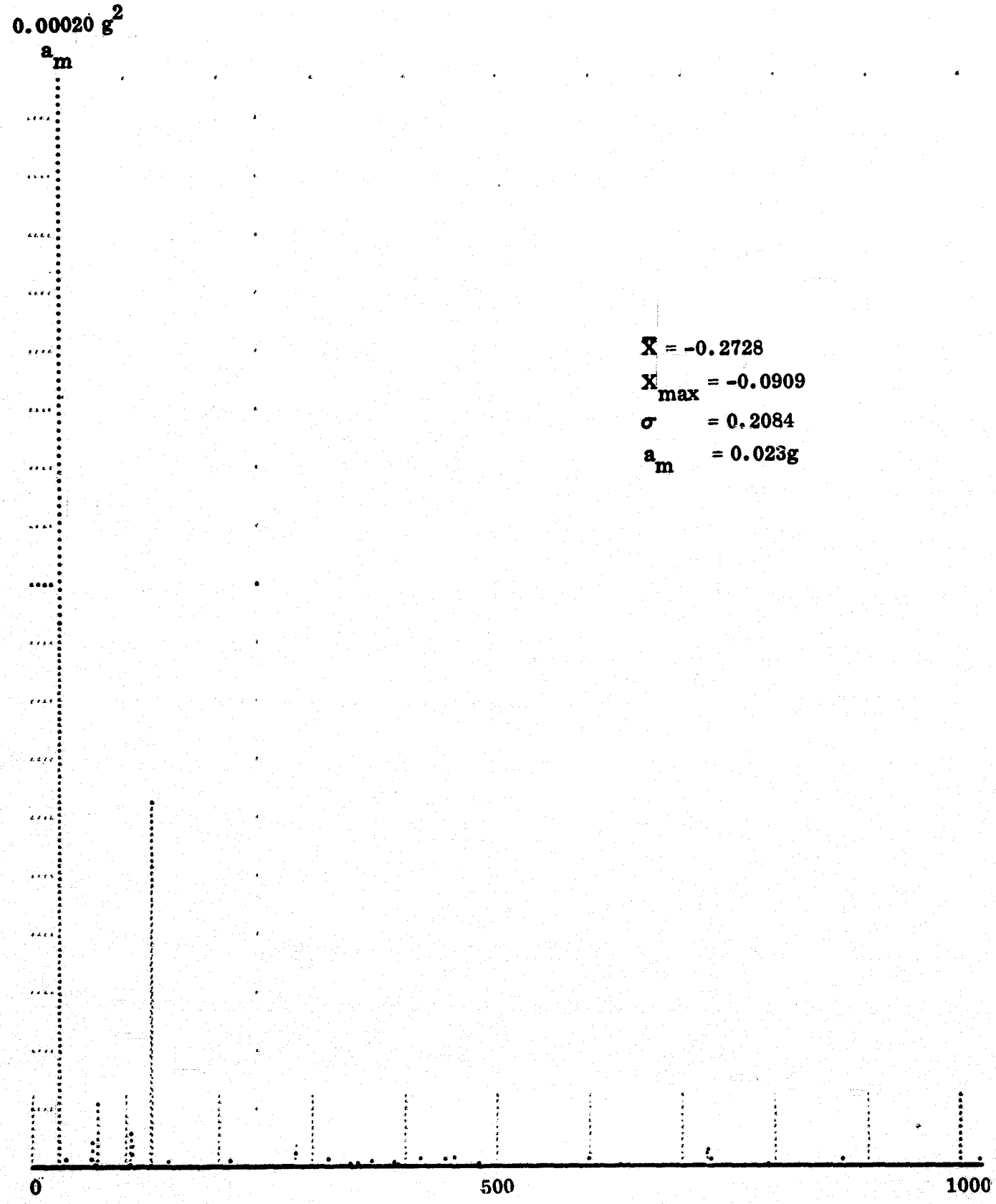

Fig. 35 PSD Inside Furnace 3, Vertical Position Background

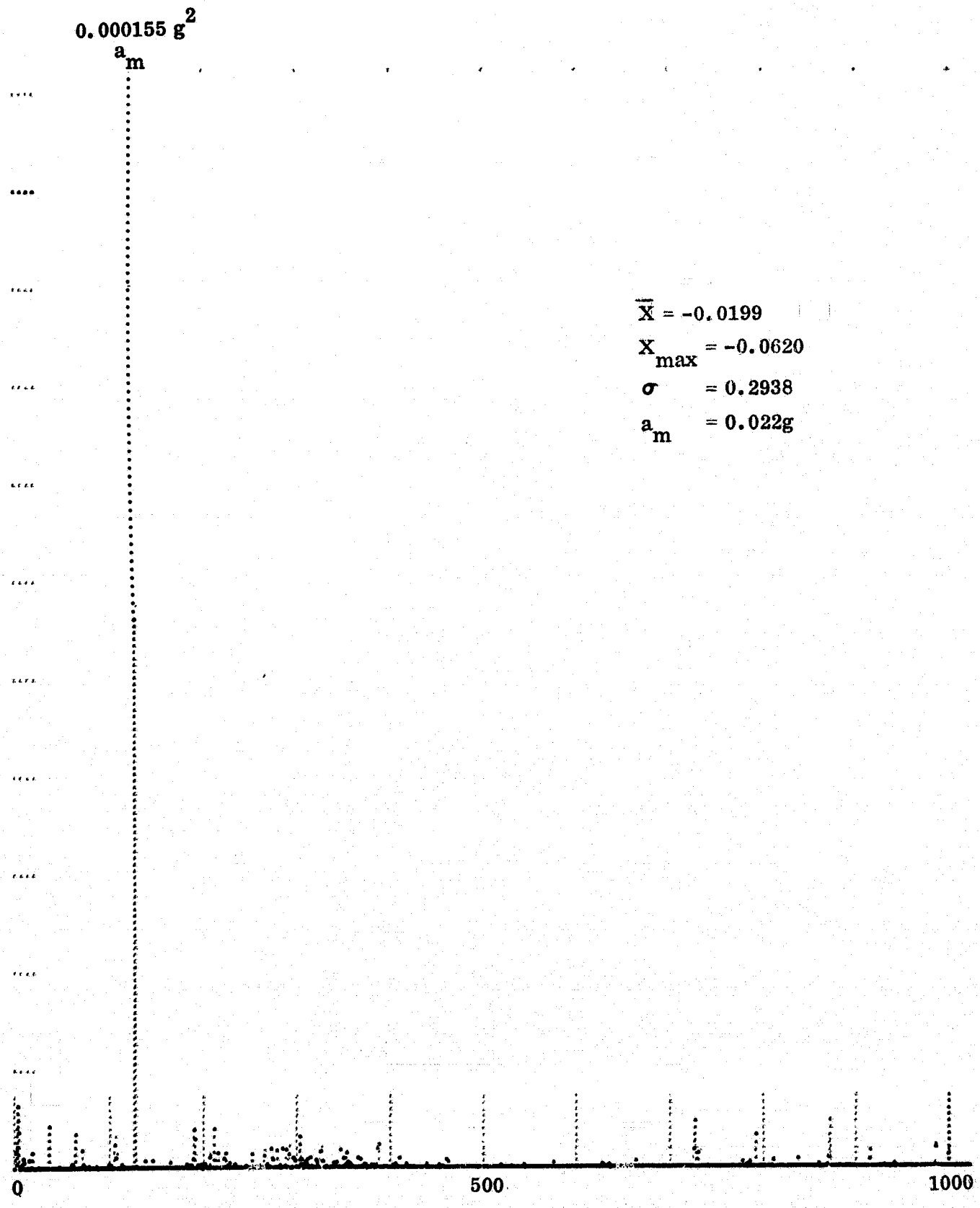

Fig. 36 PSD Inside Furnace 3, Horizontal Position Background

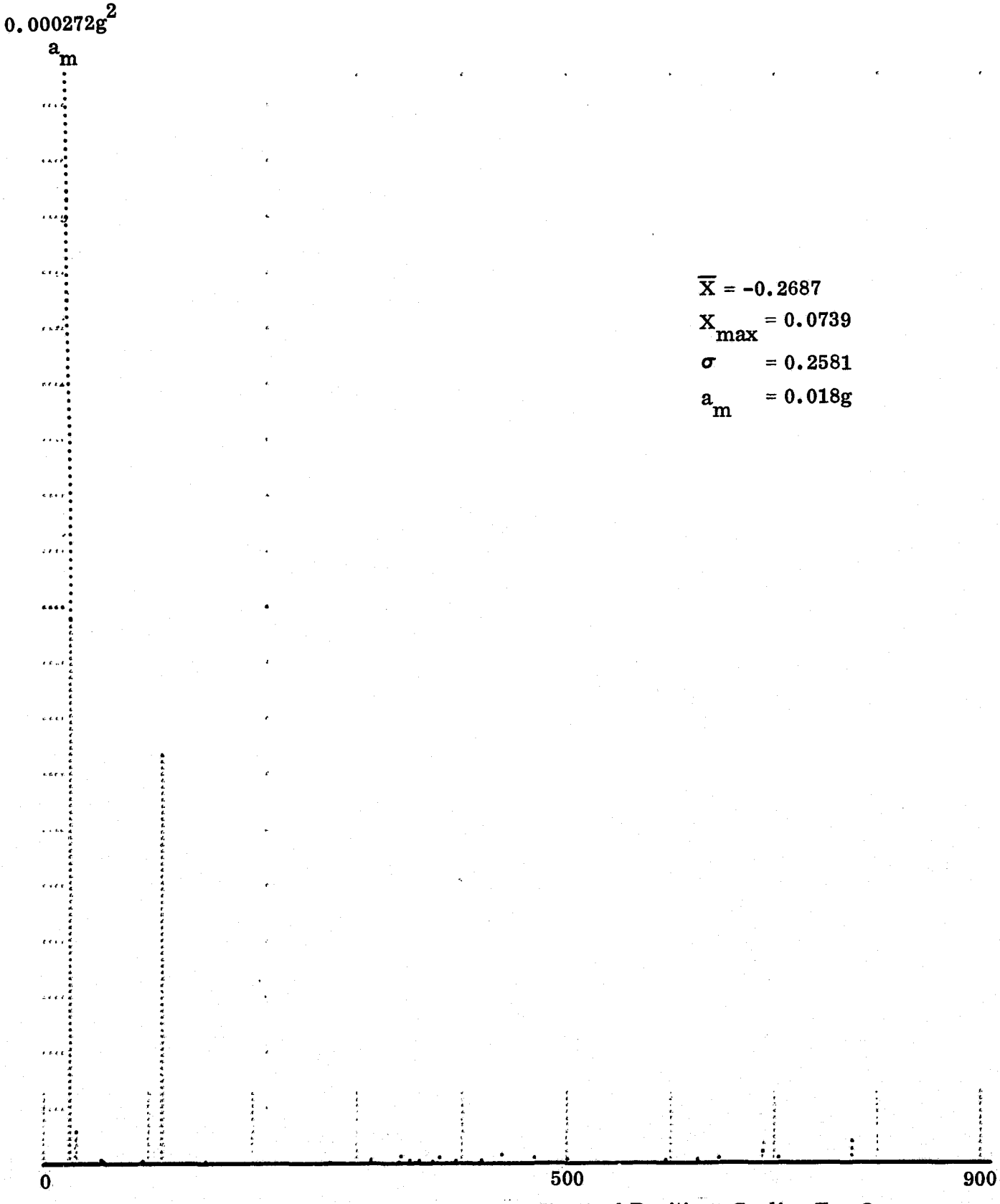

Fig. 37 PSD Inside Furnace 3, Vertical Position, Cooling Fan On

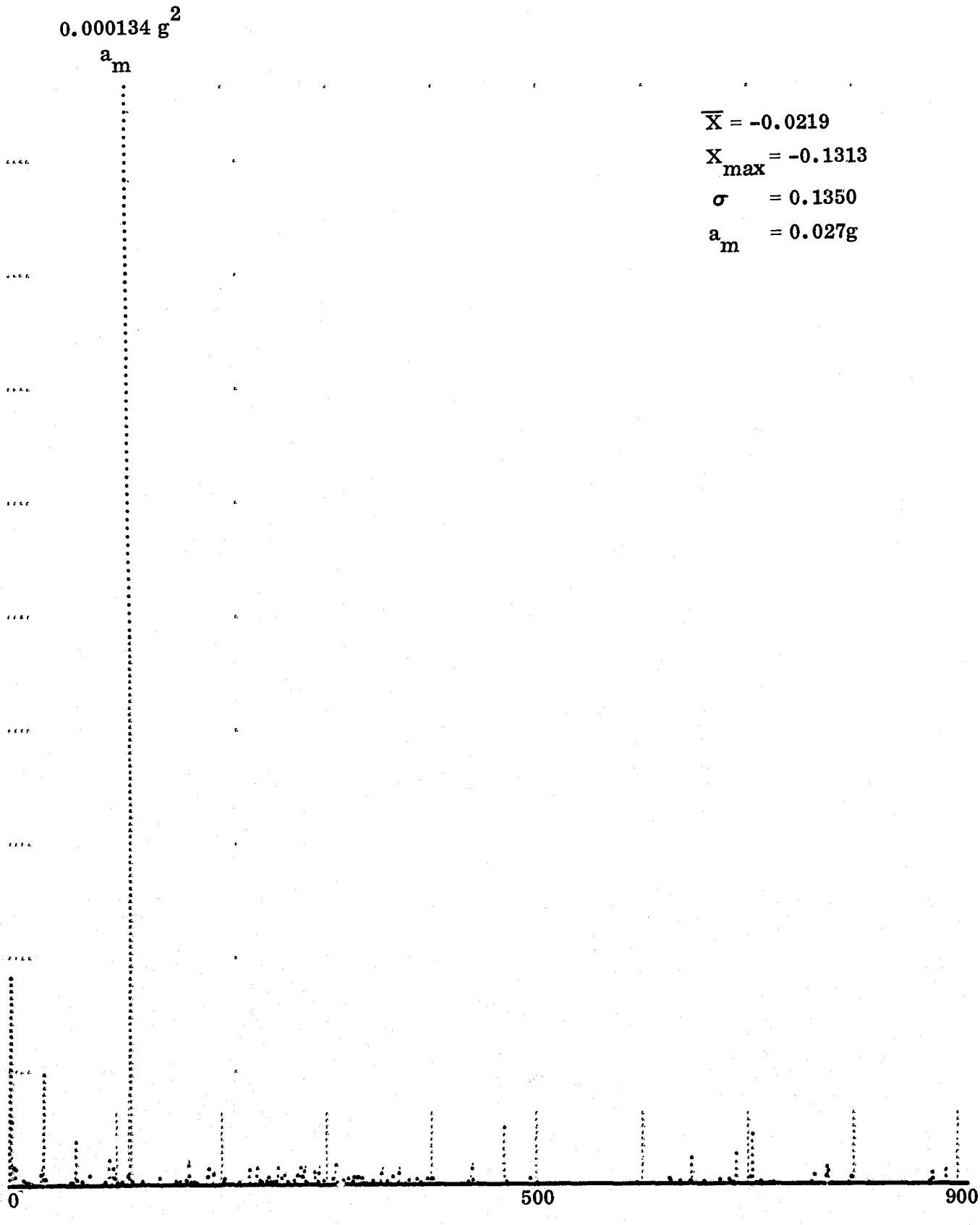

Fig. 38 PSD Inside Furnace 3, Horizontal Position, Cooling Fan On

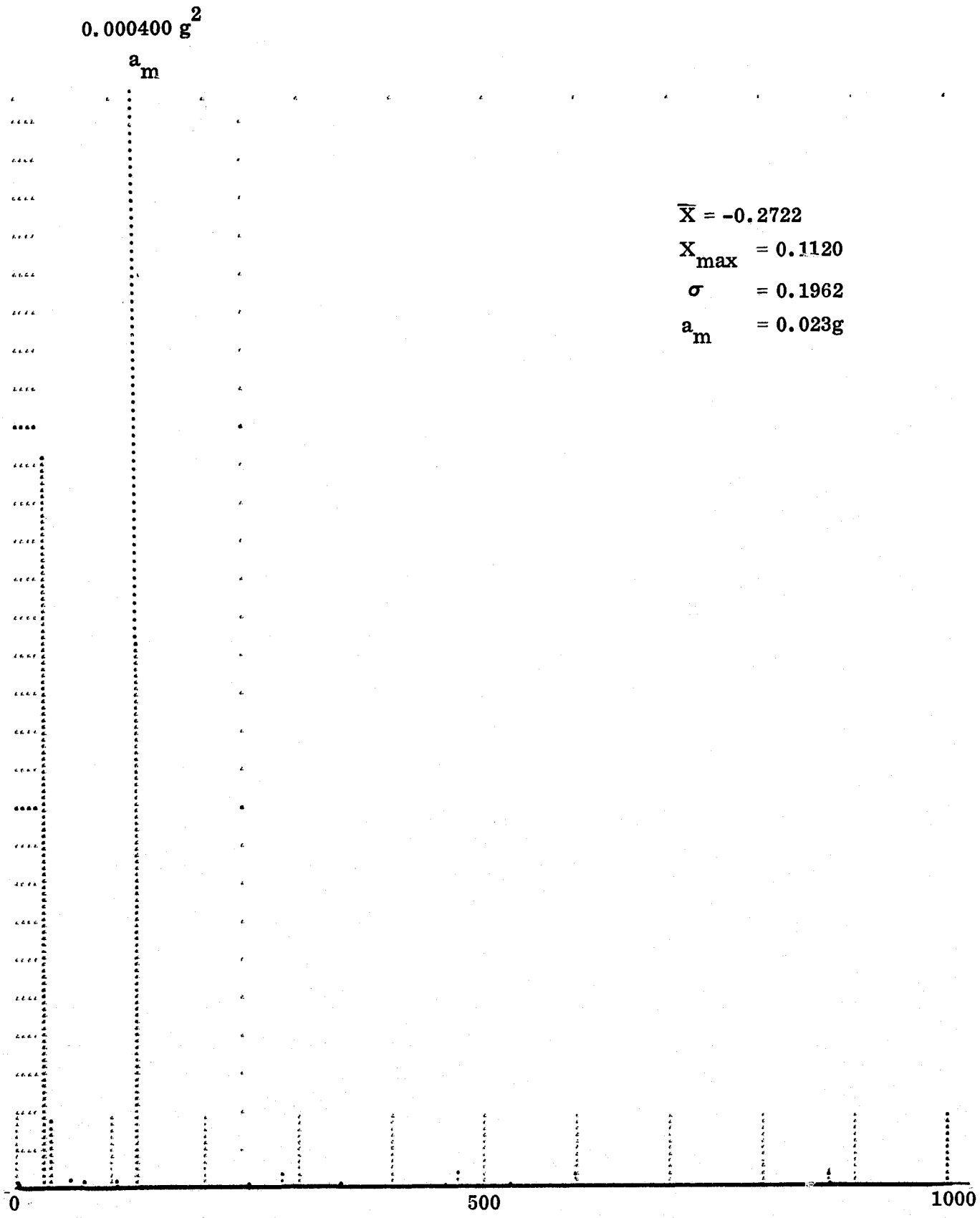

Fig. 39 PSD Inside Furnace 3, Vertical Position, Heater and Cooling Fans On

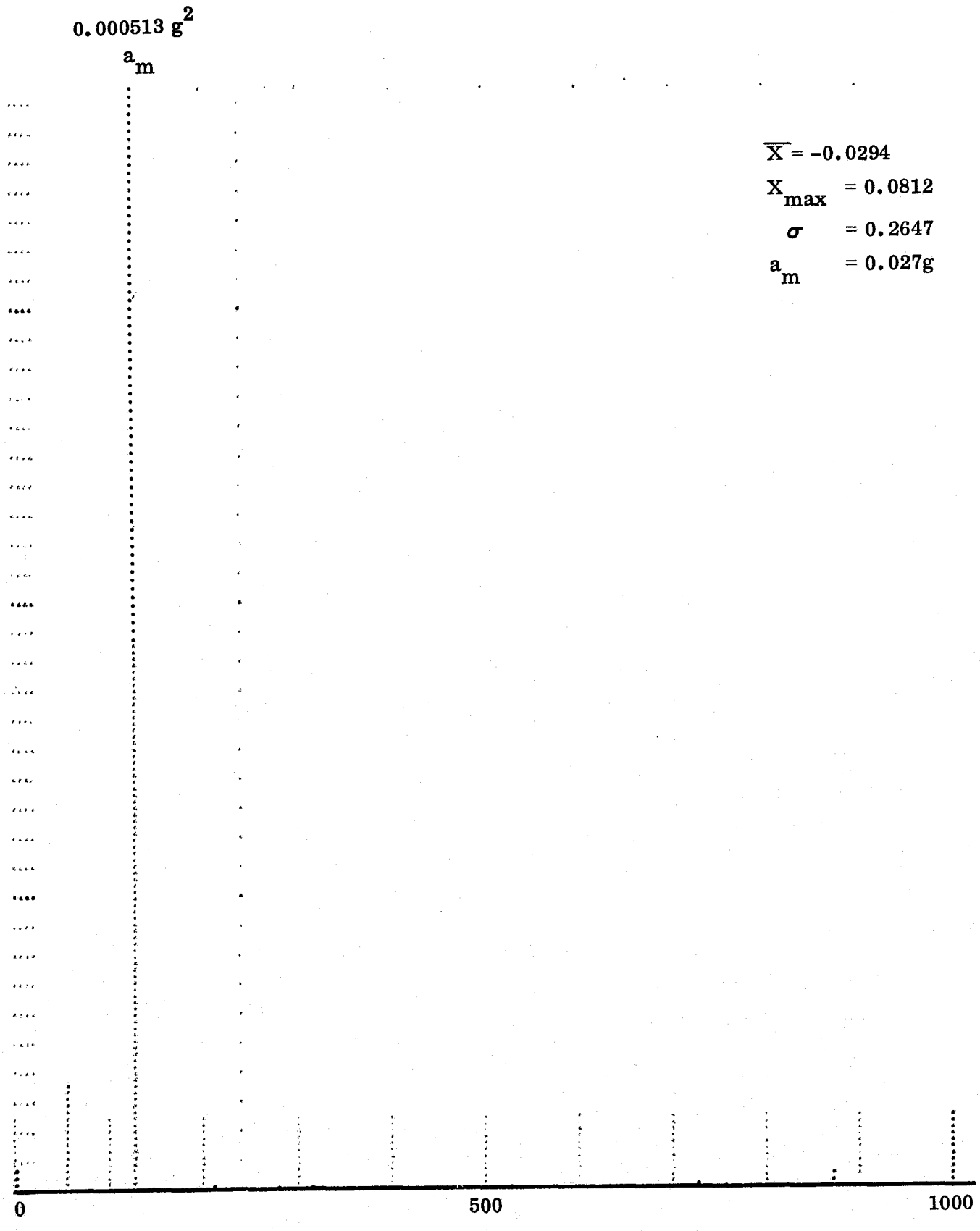

Fig. 40 PSD Inside Furnace 3, Horizontal Position, Heater and Cooling Fans On

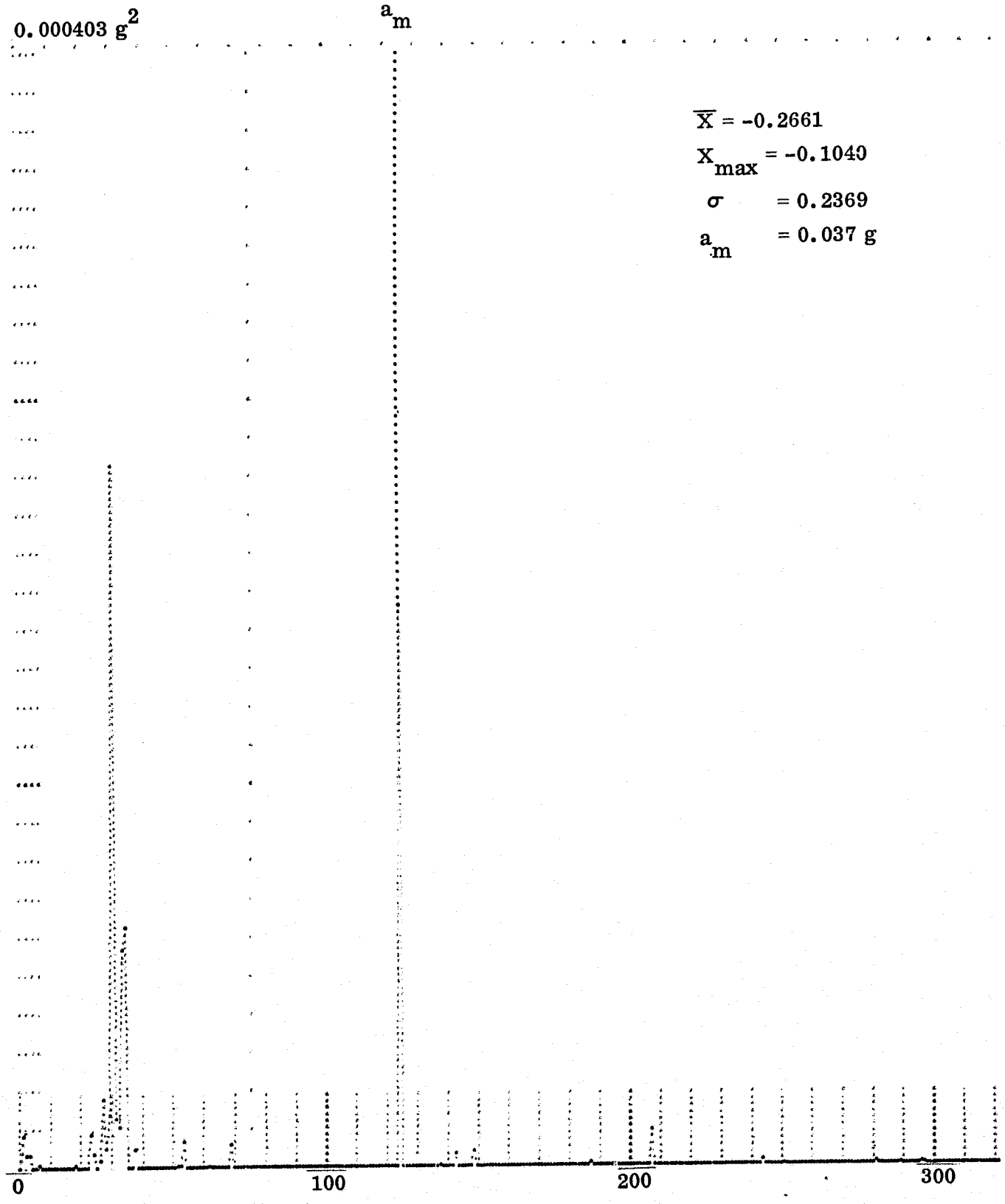

Fig. 41 PSD Inside Furnace 3, Vertical Position, Hood, Heater, and Cooling Fans On

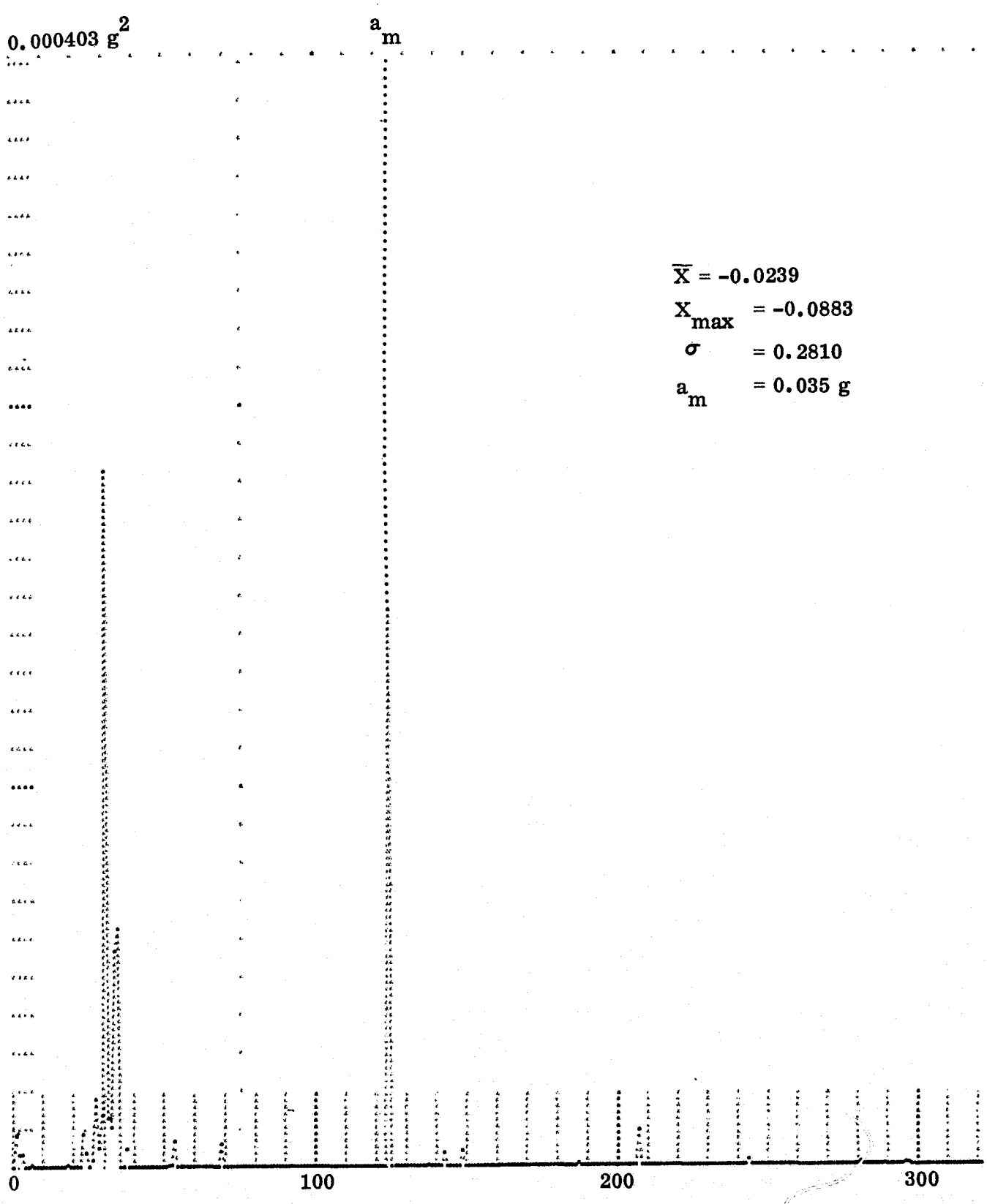

Fig. 42 PSD Inside Furnace 3, Horizontal Position, Hood, Heater, and Cooling Fans On

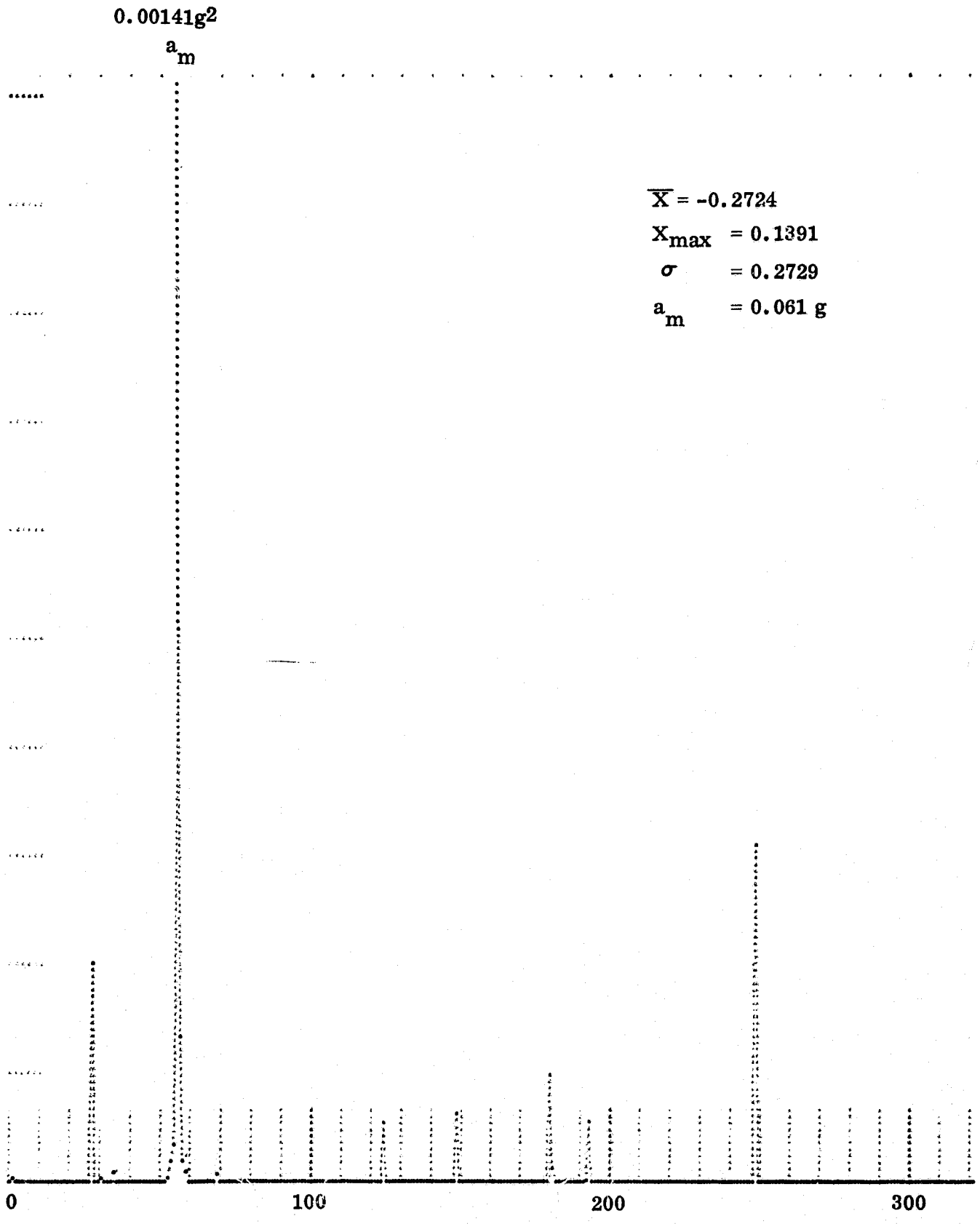

Fig. 43 PSD Inside Furnace 3, Vertical Position, Scan Motor, Hood, Heater and Cooling Fans On

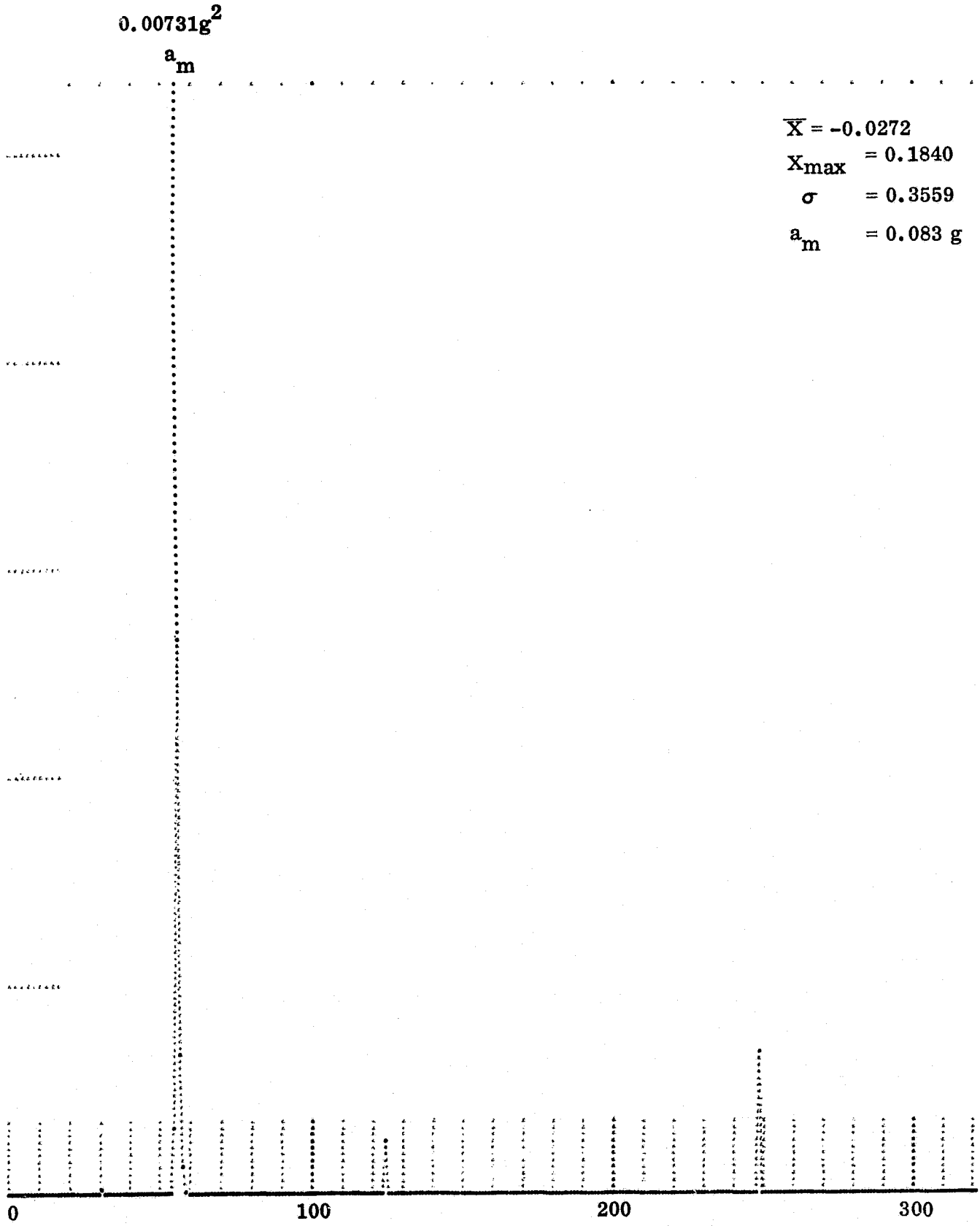

Fig. 44 PSD Inside Furnace 3, Horizontal Position, Scan Motor, Hood, Heater, and Cooling Fans On

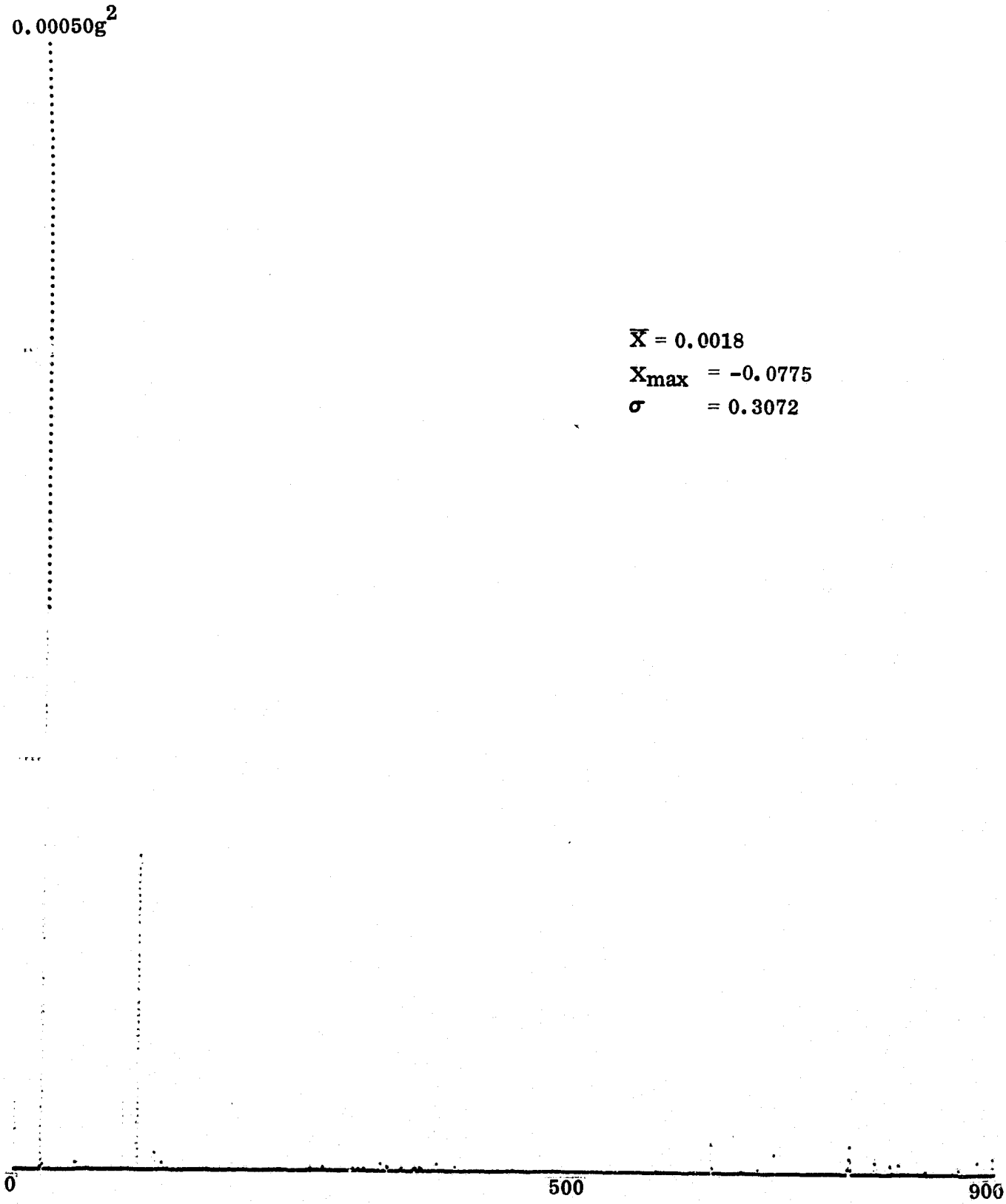

Fig. 45 PSD Inside Furnace 10, Vertical Position, Background

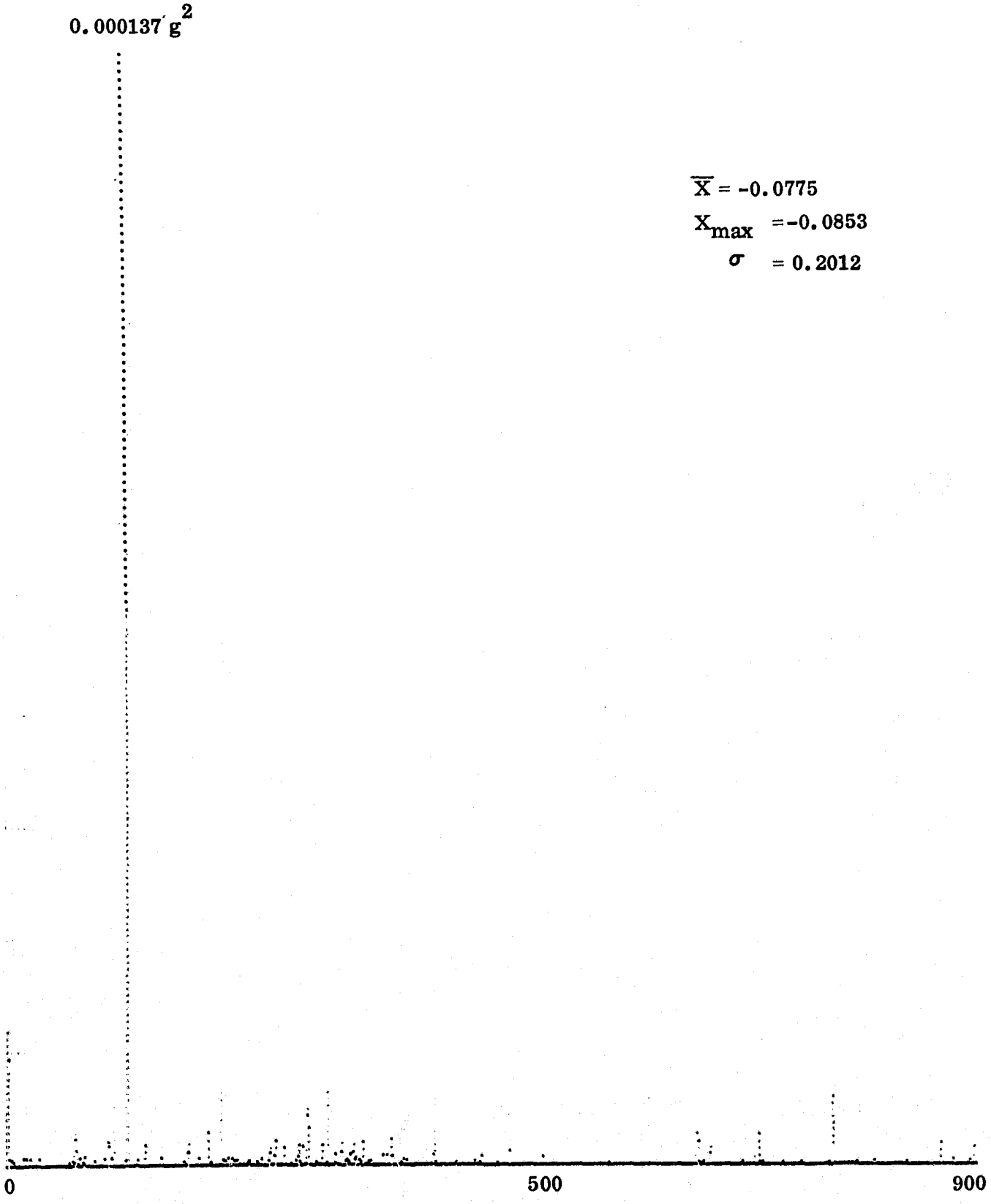

Fig. 46 PSD Inside Furnace 10, Horizontal Position, Background

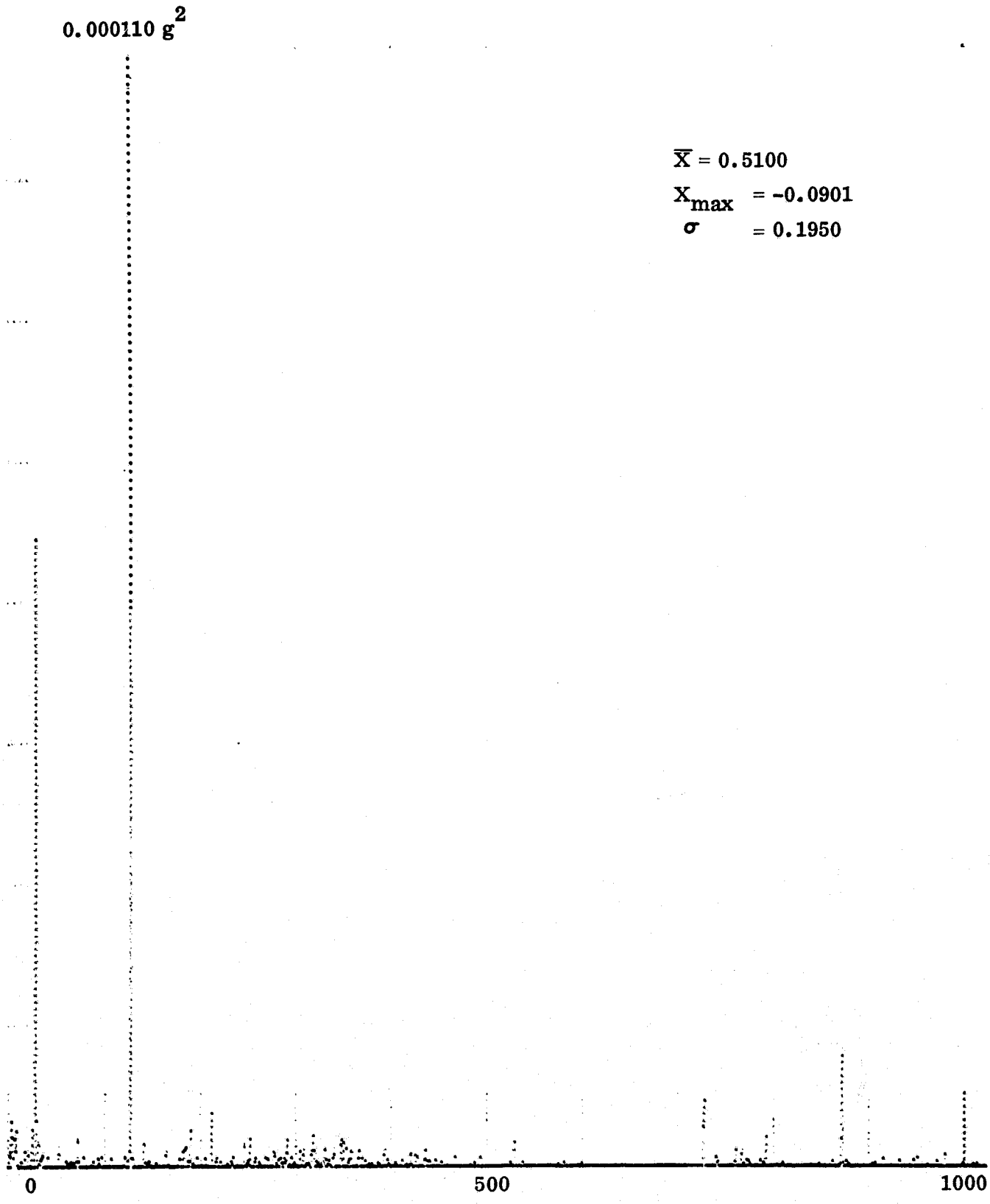

Fig. 47 PSD Inside Furnace 10, Horizontal Position, Heater and Cooling Fans On

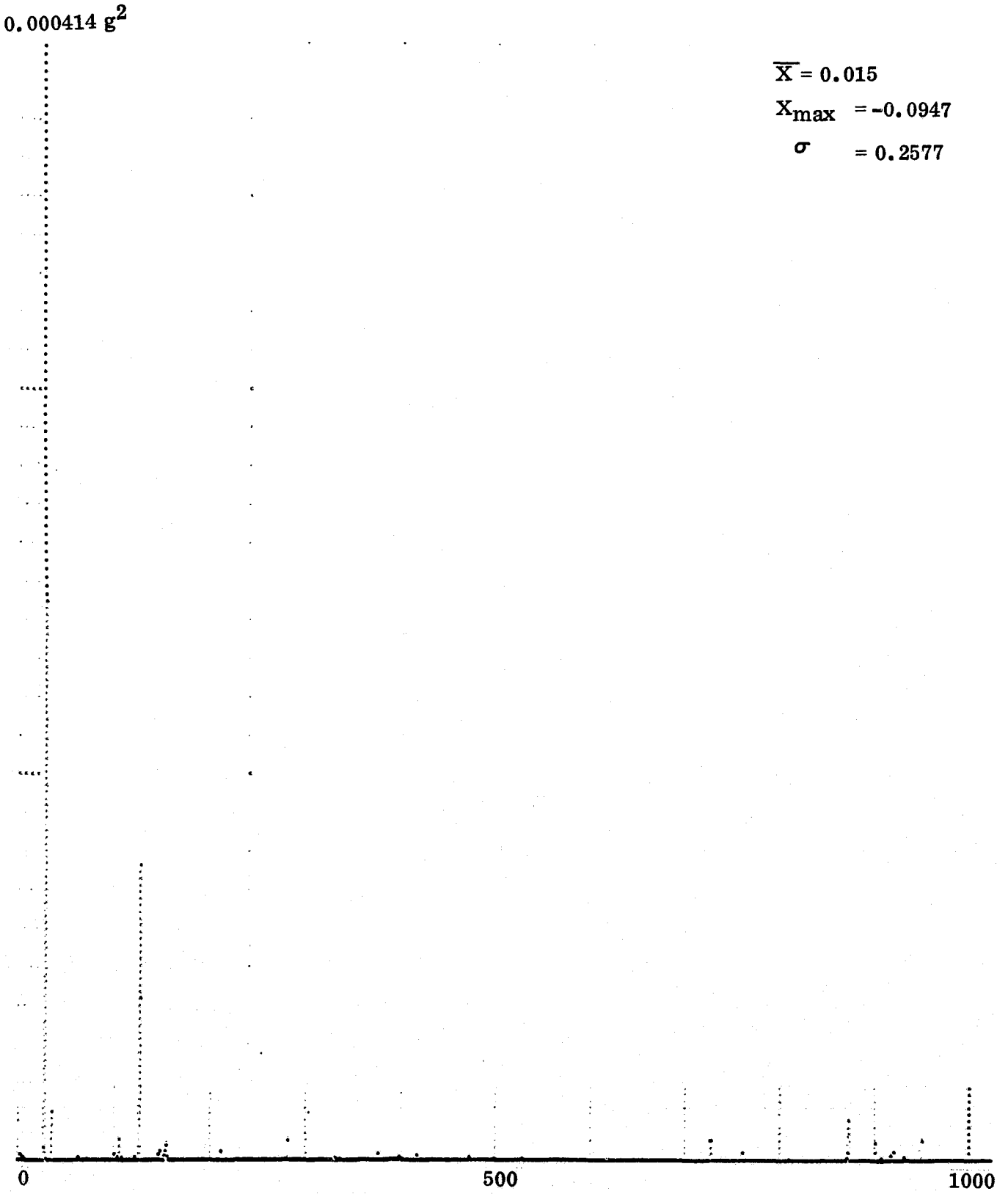

Fig. 48 PSD Inside Furnace 10, Vertical Position, Heater and Cooling Fans On

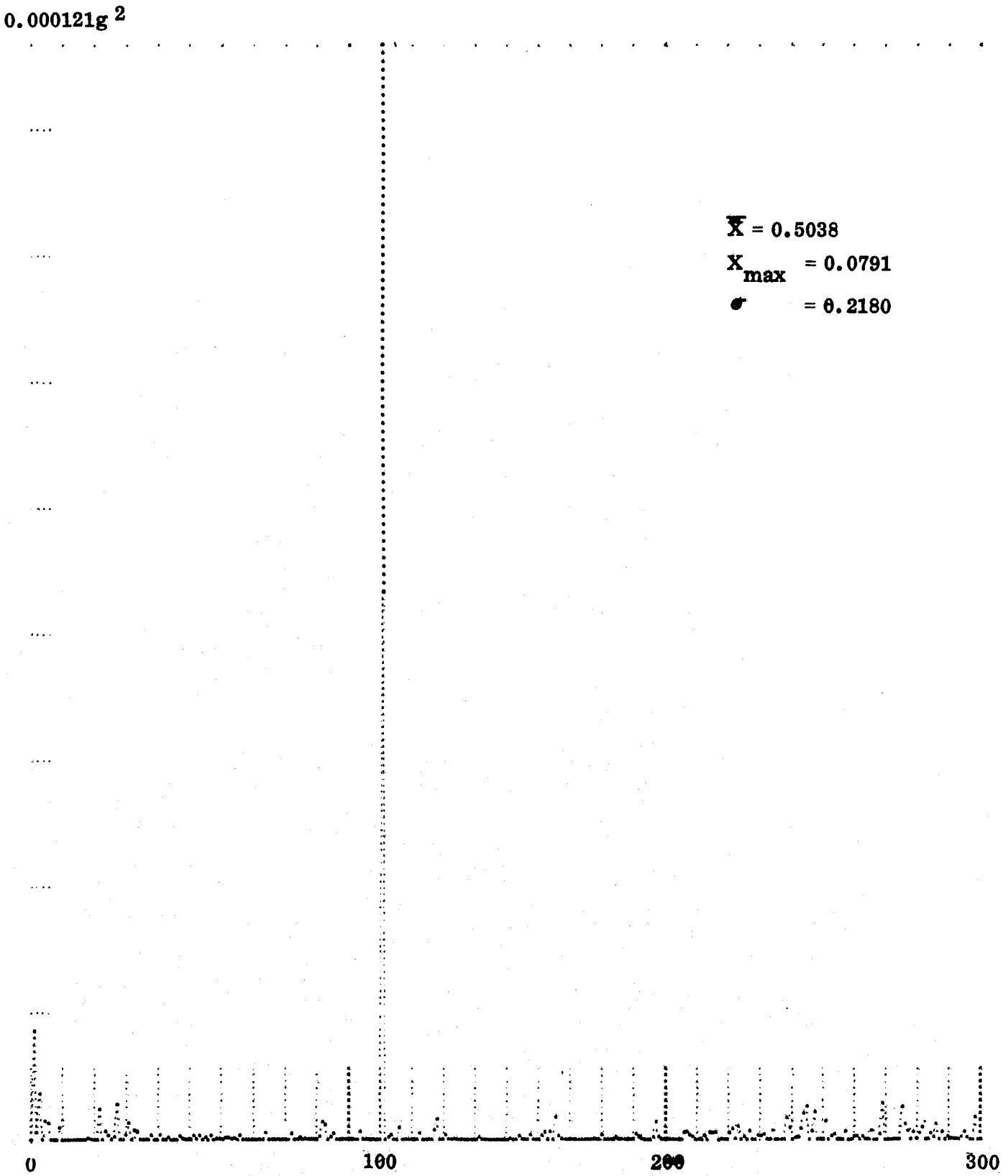

Fig. 49 PSD Inside Furnace 10, Horizontal Position, Hood, Heater, and Cooling Fans On

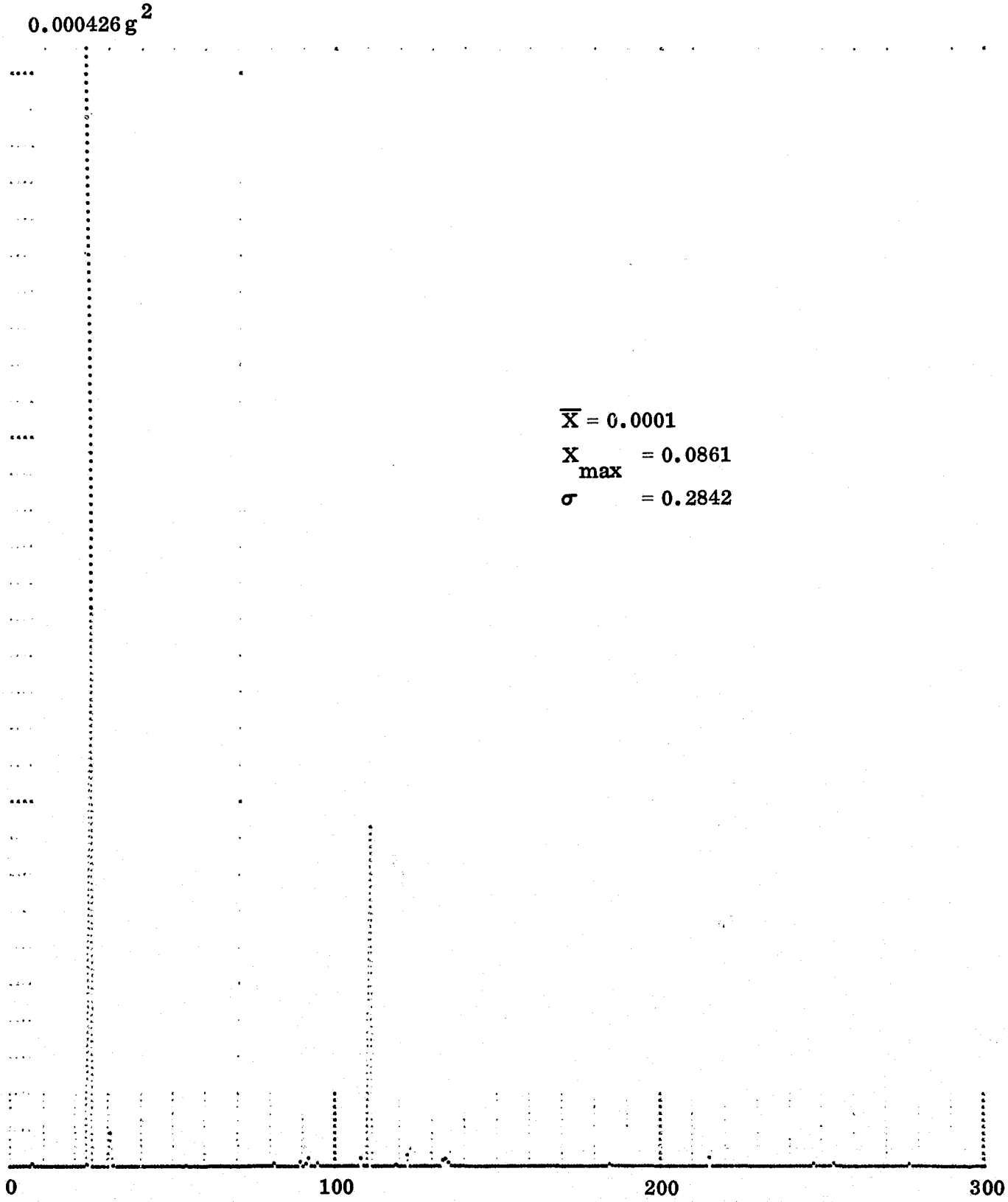

Fig. 50 PSD Inside Furnace 10, Vertical Position, Hood, Heater and Cooling Fans On

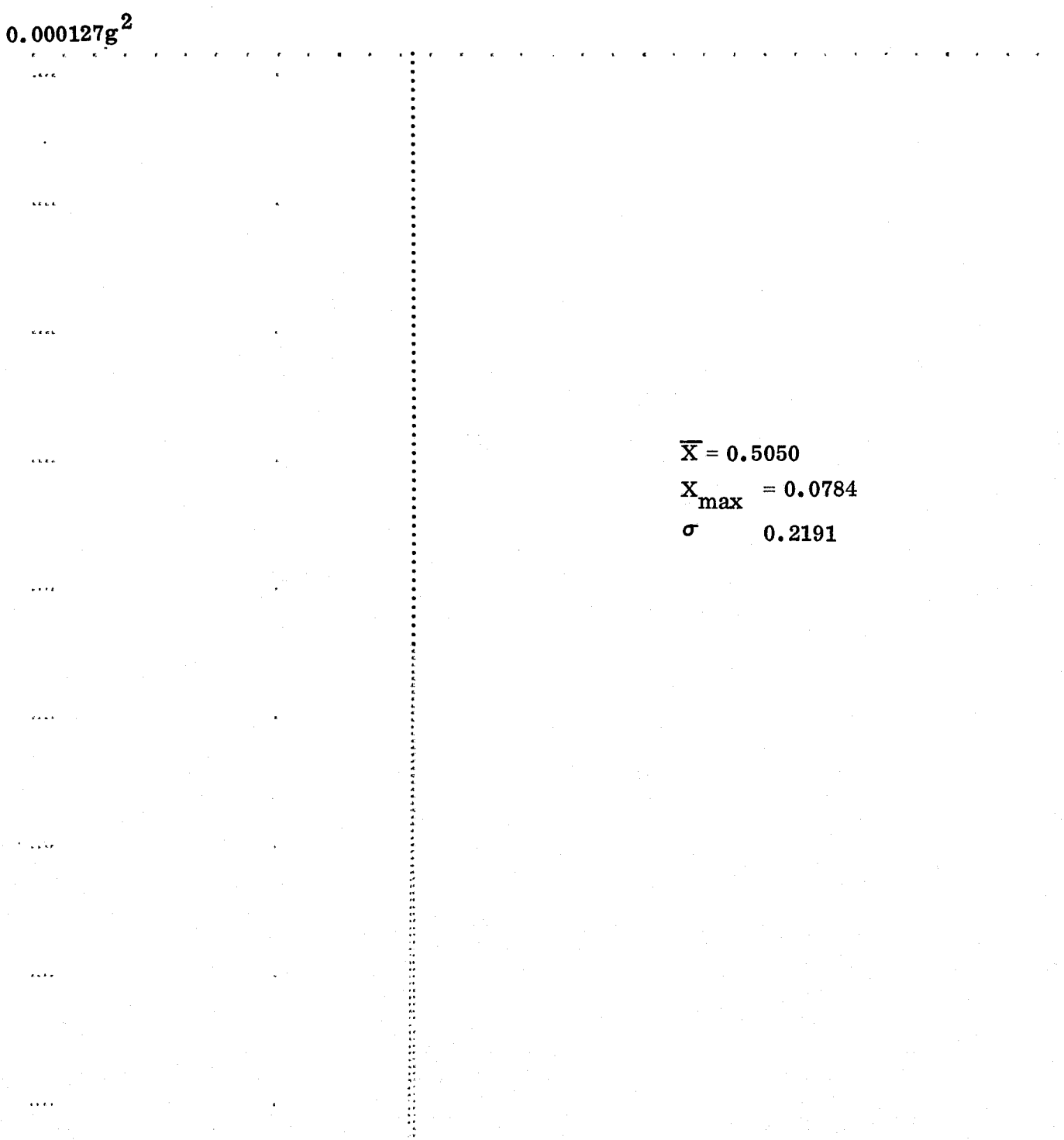

Fig. 51 PSD Inside Furnace 10, Horizontal Position, Scan Motor, Hood, Heater and Cooling Fans On

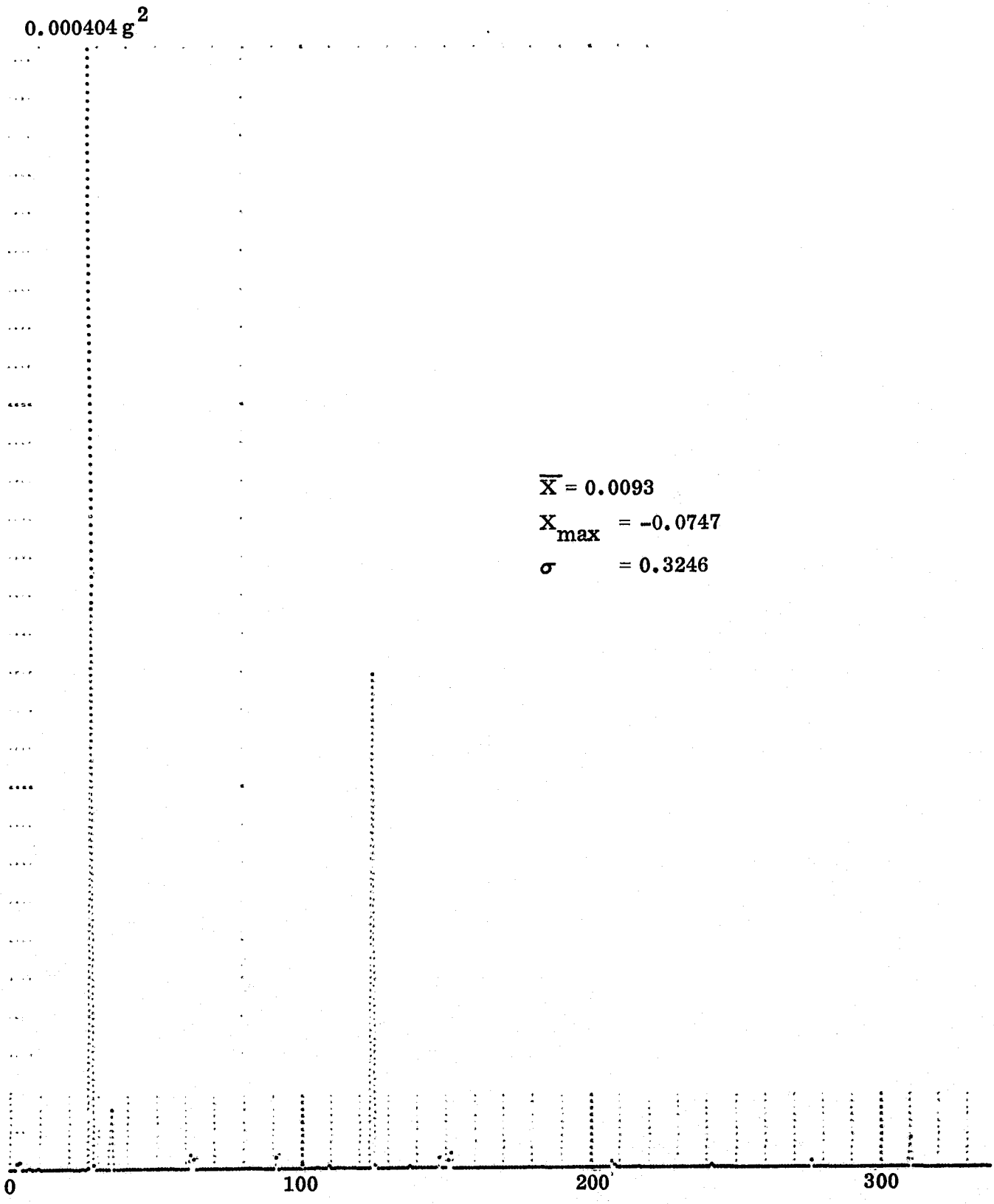

Fig. 52 PSD Inside Furnace 10, Vertical Position, Scan Motor, Hood, Heater and Cooling Fans On

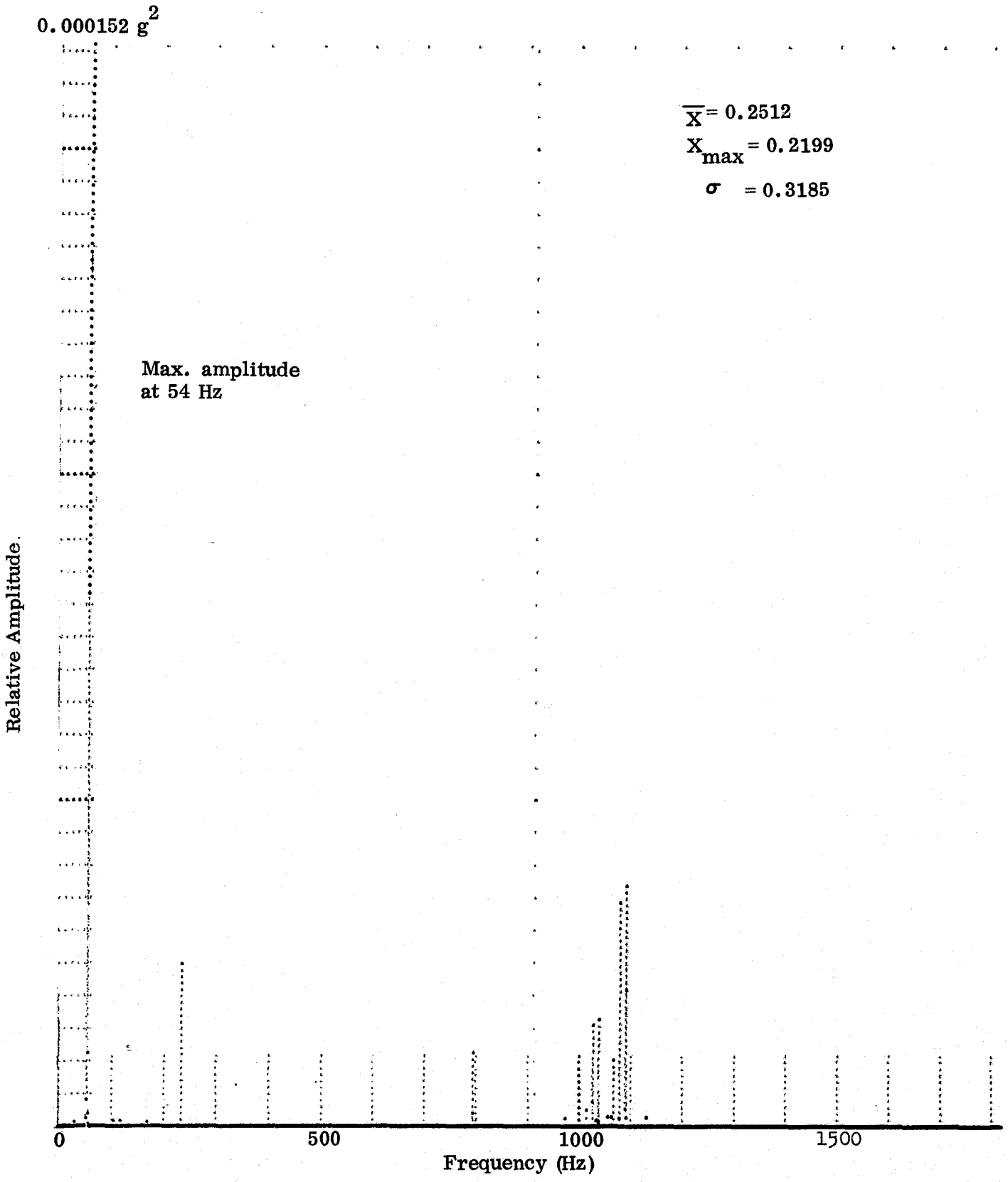

Fig. 53 PSD Inside Furnace 10, Horizontal Position, Scan Motor, Hood, Heater, and Cooling Fans On

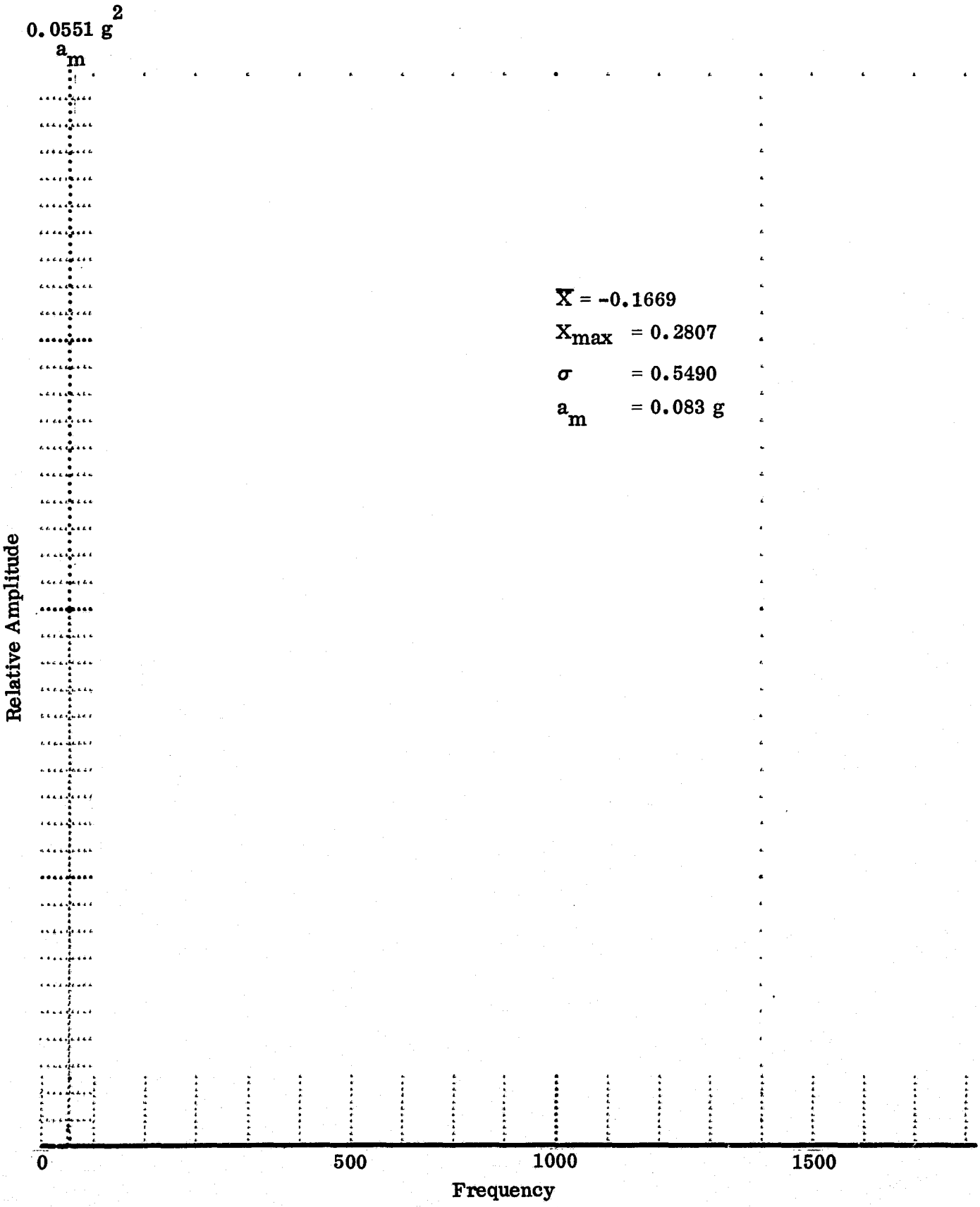

Fig. 54 PSD on Furnace 3 SiC Tube, Horizontal Position, Scan Motor, Hood, Heater, and Cooling Fans On

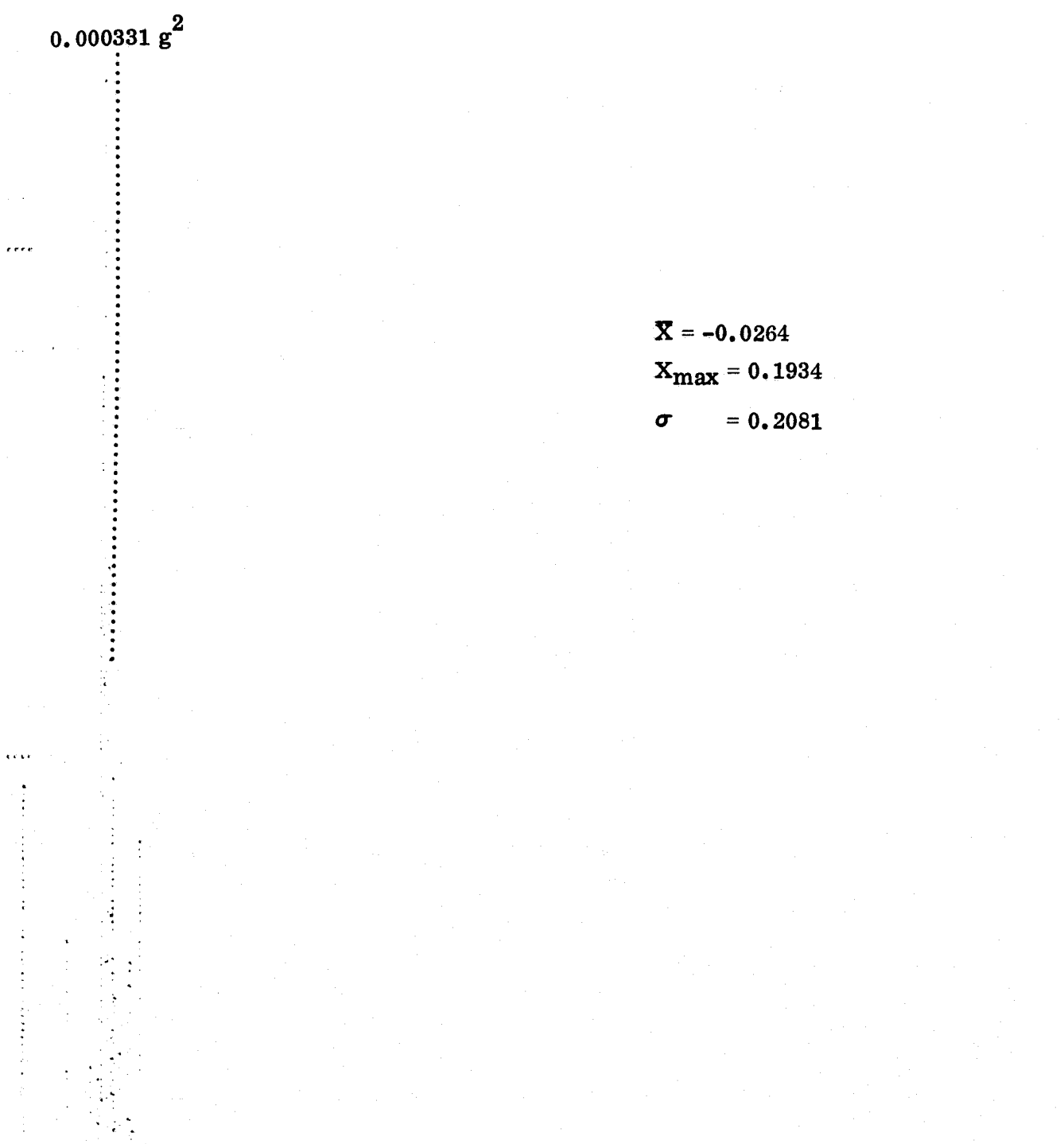

Fig. 55 PSD on Furnace 3 SiC Tube, Vertical Position, Tapping on Door

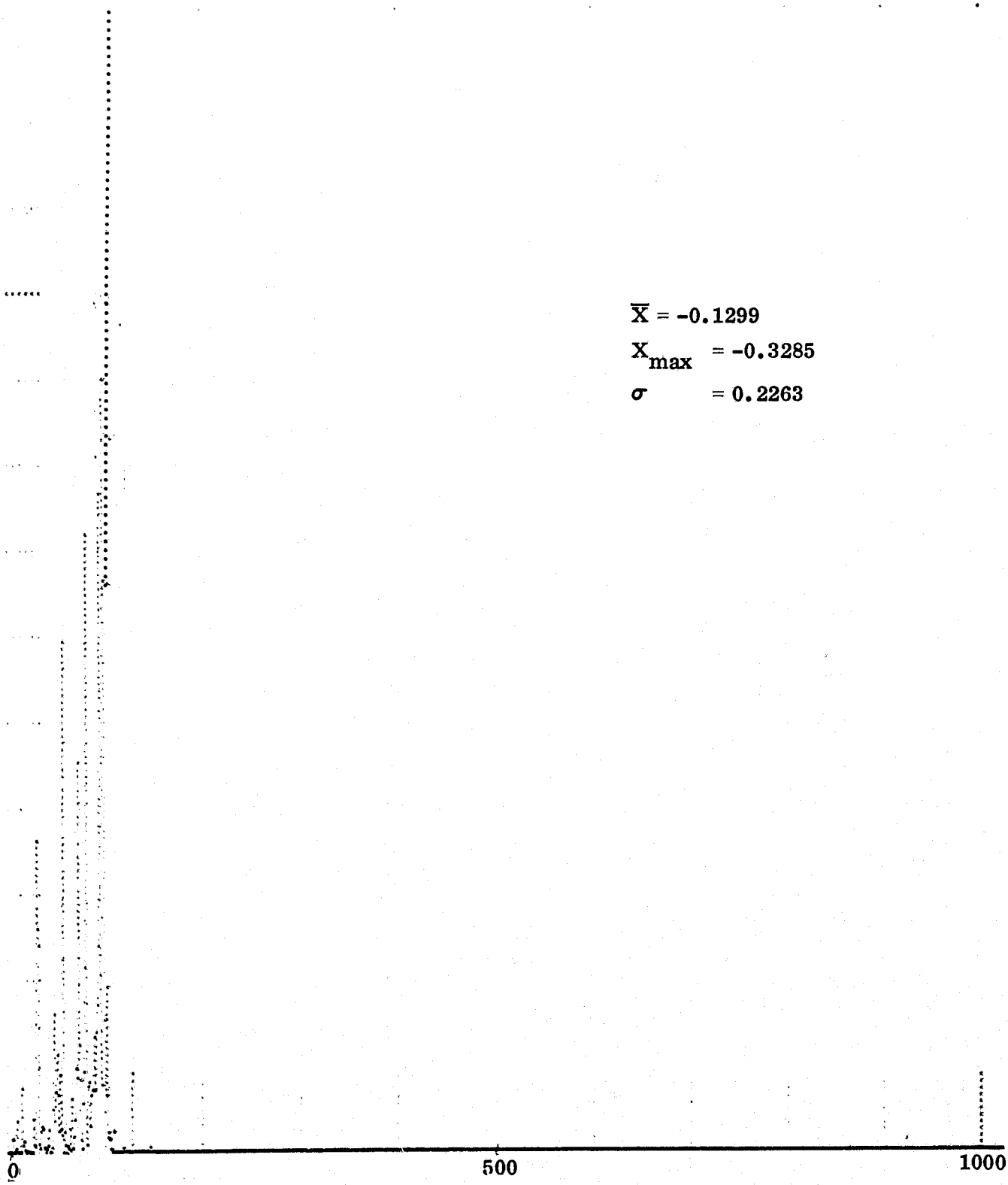

Fig. 56 PSD on Furnace 3 SiC Tube, Horizontal Position, Tapping on Door

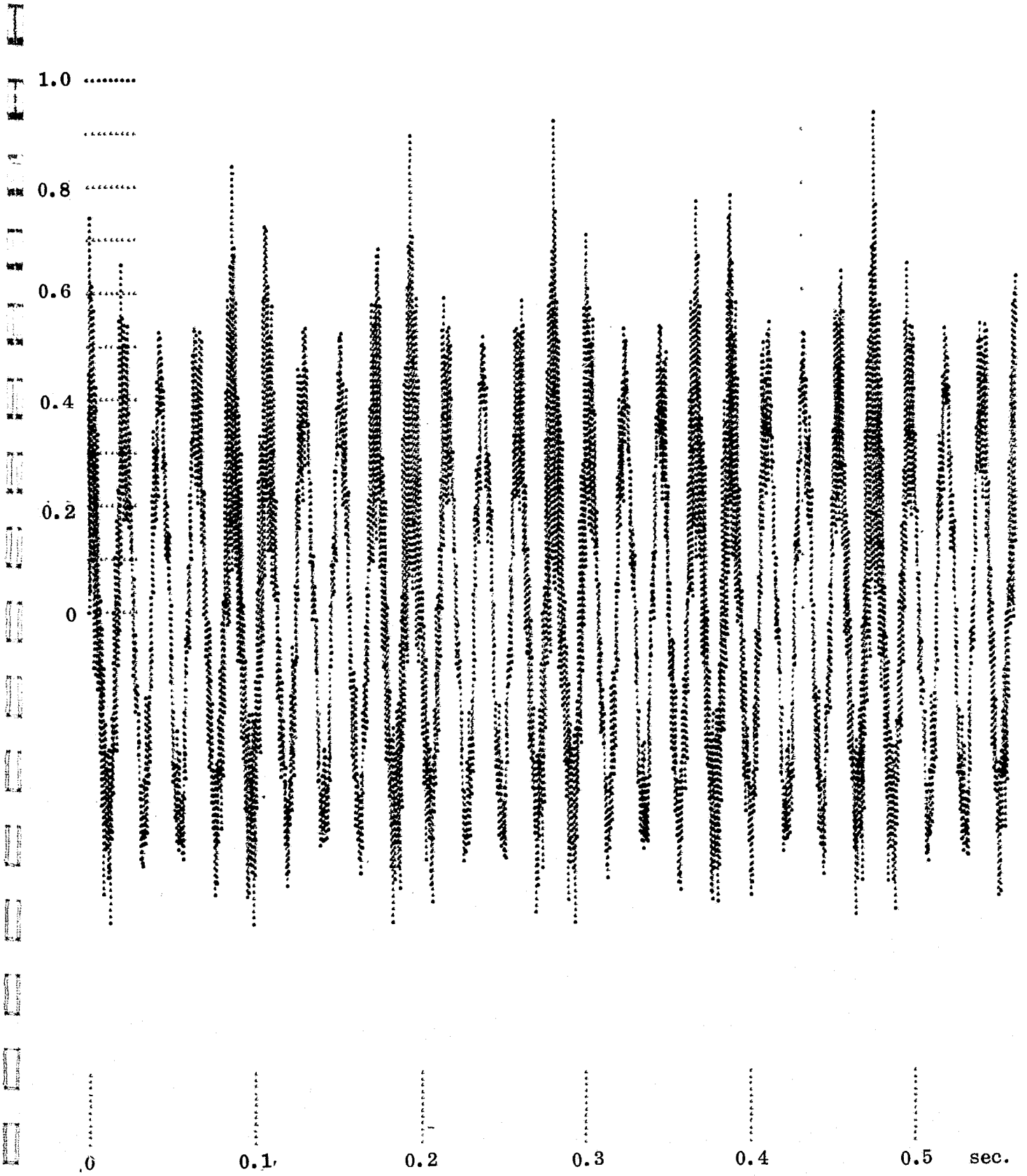

Fig. 57 Autocorrelation on Furnace 3 SiC Tube, Vertical Position, Scan Motor, Hood, Heater, and Cooling Fans On

Table 20. Summary of PSD Analyses of Vibration Signals

Source	Position	Furnace	Direction	$\overline{X}$	X_{max}	σ	$a_{max,g}$	$fa,_{max}$
Background	Quartz bt	3	Vert	-0.272	-0.091	0.208	0.016	30 Hz
Background	Quartz bt	3	Hor	-0.020	-0.062	0.294	0.012	120
Cool Fan	Quartz bt	3	Vert	-0.269	0.074	0.258	0.016	30
Cool Fan	Quartz bt	3	Hor	-0.022	-0.131	0.135	0.012	120
Htr & Cool Fan	Quartz bt	3	Vert	-0.272	0.112	0.196	0.020	130
Htr & Cool Fan	Quartz bt	3	Hor	-0.294	0.081	0.265	0.022	125
Hd, Htr, Cool Fan	Quartz bt	3	Vert	- .266	-0.104	0.237	0.020	125
Hd, Htr, Cool Fan	Quartz bt	3	Hor	- .024	- .088	0.281	0.020	125
Fans, all	Quartz bt	3	Vert	-0.272	0.139	0.272	0.038	57
Background	Quartz bt	3	Hor	-0.027	0.184	0.356	0.085	57
Background	Quartz bt	10	Vert	0.002	-0.078	0.307	0.020	25
Cool Fan	Quartz bt	10	Hor	-0.078	-0.085	0.201	0.012	110
Cool Fan	Quartz bt	10	Vert					
Htr & Cool Fan	Quartz bt	10	Hor	0.510	-0.090	0.195	0.010	125
Htr & Cool Fan	Quartz bt	10	Vert	0.002	-0.095	0.258	0.020	30
Hd, Htr, Cool Fan	Quartz bt	10	Hor	0.504	0.079	0.218	0.011	110
Hd, Htr, Cool Fan	Quartz bt	10	Vert	0.000	-0.086	0.284	0.021	35
Scan, Hd, Htr, Cool	Quartz bt	10	Hor	0.505	0.078	0.219	0.011	125
	Quartz bt	10	Vert	0.009	-0.075	0.325	0.020	28
Fans, all	Quartz bt	10	Hor	0.578	0.077	0.254	0.012	120
	SiC tube	3	Vert	-0.251	0.220	0.318	0.022	60
Tapping On Door	SiC tube	3	Hor	-0.167	0.281	0.549	0.235	60
Tapping On Door	SiC tube	3	Vert	-0.026	0.193	0.208	0.018	110
	SiC tube	3	Hor	-0.130	-0.328	0.226	0.042	110

Each of the 2000 points on this figure was obtained by correlating the signal spectra with a similar signal spectra but shifted by increments of one data point. The wavy curve fluctuates from +1.0 for perfect positive correlation to -1.0 for perfect negative correlation. The regularity and periodicity of the wave line are to be noted.

E. Other Analyses

Other computer analyses show that the vibration spectra all appeared to be Gaussian type. Also, walking and jumping near the furnace, or opening and slamming a door to the next room did not introduce any additional vibration.

As expected, maximum vibration occurred directly on the scan motor, followed by positions on the support chain block (for the transmission gears), SiC tubes inside the furnace, and the quartz boat inside the furnace at the seed position.

The unbalanced scan motor on furnace 3 generated substantial vibrations at 54 Hz in both the vertical and horizontal directions. Finger tapping of the end doors also created transient vibrations whose frequencies between 60 and 100 Hz had the largest amplitudes in the horizontal direction. In the vertical direction, 80 to 120 Hz were the most predominant. In both cases, 100 Hz signals had the largest amplitudes. By considering that tapping could excite all frequencies, including resonantly frequencies, these tests point towards a resonant frequency of about 100 Hz for the SiC tube in furnace 3. In amplitudes, these excited vibrations are twice that created by the unbalanced scan motor on furnace 3.

F. Conclusions and Discussions on Vibration Effects on Crystal Growth

We conclude, from the above results, that

1. the fluctuations in crystal yield at our vendor were not due to random causes, but due to a definite causative effect.

2. Such a causative effect can be traced to a damaged, unbalanced motor. The effect of this motor on crystal growth was significant, independent of the growth furnace or growth period.

3. This motor introduced a vibration spectra in the vertical and horizontal directions which were completely different from those due to an undamaged or control motor.

4. The vibration spectra due to this unbalanced motor has been fully characterized by detailed measurements. Their amplitudes peaked at milli-g's at 54 Hz. These amplitudes were much greater than the background noises.

5. In contrast, the cooling fan for the electronic temperature control circuit did not introduce any appreciable additional vibrations over the background; the heater fan for the room had some additional vibration spectra of low amplitudes at 50 Hz in the vertical direction. The hood exhaust fan introduced some vibrations at 123 Hz which were stronger than those due to the heater fan, but still much weaker than those due to the unbalanced scan motor.

6. Tapping the end doors of the furnaces created vibrations at 110 Hz which were much stronger than those due to the unbalanced motor. This indicates the need to improve the door designs to minimize vibrations.

7. All the vibration spectra appeared to be Gaussian type. The regularity and periodicity of the wave line on the autocorrelation curve suggest the regularity and periodicity of the vibration signals. That is, these signals were probably sinusoidal in shape.

8. Walking and jumping near the furnace, or opening and slamming a door (6 feet away) to the next room did not introduce any additional measurable vibrations. This conclusion confirms the good isolation of the furnace support.

9. A freight train passing within 200 feet did not noticeably affect any of the background vibration spectra. This disproves the common fallacy that good crystal growth facilities must be located, often at great costs, far away from railway tracks

We also conclude that a proper vibration (or oscillating) force of even less than 0.05 g is significant in improving crystal quality and yield. Such a small g force is subtle and is easily masked in ground experiments, such as the previous MIT work (Ref. 25), but probably requires space environment for systematic study, i.e., isolation, evaluation, and optimization.

This vibration experiment presented some interesting questions related to space processing. Did the vibrations due to the unbalanced motor indeed improve the liquid mixing ahead of the solid-liquid interface? Did these vibrations really have a "massaging" action? If milli-g forces were beneficial, could proper micro-g forces also be beneficial? What are the vibration spectra due to g-jitters, astronauts walking or handling the equipment? Could some of the mysterious Skylab results be due to some hidden vibrations?

We have thus carefully and systematically documented the different sources of vibrations on one set of GaAs growth furnaces, and, in particular, fully characterized the beneficial vibration spectra due to an unbalanced motor. We cannot, without any additional work, pinpoint exactly which particular single or combined vibration frequencies are beneficial, nor the critical amplitude ranges for each such frequency. Nor can we speculate as to the exact mechanism of improved crystal yield. This important crystal growth knowledge must probably also be unambiguously obtained by controlled space experiments for subsequent uses on earth.

7. CONCLUSIONS

We have briefly reviewed results developed under our previous contract (NAS8-27891) and assessed where we were when present contract started.

The new computer programs developed under this contract are found to be powerful in the study of the combined effects of evaporation and solidification. Some unexpected results have thus been discovered. Specifically, we have found that the solidification-evaporation is sensitively affected in a complicated manner by the combined effects of melt temperature and composition, or liquid mass transfer mechanisms such as convection currents. The solidification velocity does not even necessarily change monotonically with the cooling time. Also, the liquid mass transfer markedly affects the position of the solidification boundary, but not that of the evaporation boundary. On the other hand, varying the initial solute concentration in the melt affects the position of the evaporation boundary, but not that of the solidification boundary. We thus have confirmed the importance of evaporation in solidification studies, and also showed some limitations of the conventional solidification theories (without evaporation).

Also from these computed results, we found a maximum effect of a given change in the liquid mass transfer on solidification. By using this information, we may maximize the subtle zero-gravity effects among the effects of other uncontrolled variables so that future space processing experiments can be designed systematically for maximum scientific returns, particularly when the technique related to a proposed "econo-technical Model of Crystal Growth" (Appendix E) is used.

We also discovered, by microprobing, some unexpected segregation effects in GaAs samples, and revealed, through determining the velocity distribution pattern, some evidence of convection currents during the GaAs growth. We thus conclude that space-grown GaAs samples by the horizontal Bridgeman method should be more uniform and perfect, in line with other Skylab crystal growth results.

A GaAs statistically designed experiment is presented to show the efficiency and applicability of this type of experiments in crystal growth, particularly during space processing where the sample sizes and available equipment, personnel, and time are necessarily limited.

In growing the GaAs crystals, we also noticed some unique, beneficial effects of vibration on crystal yield and perfection. We examined the many possible effects of vibration on crystal growth and believe that the most plausible mechanism relates to liquid mixing ahead of the solid-liquid interface. Hence, understanding vibration effects may contribute importantly to understanding the reduced liquid mass transfer in space conditions. We have carefully documented the different sources of vibrations on some GaAs growth furnaces and, in particular, fully characterized the beneficial vibration spectra that improved the crystal quality. However, more work is still required to confirm the proposed beneficial mechanism, and to optimize and apply these mechanisms in space and ground crystal growth operations.

8. RECOMMENDATION FOR FUTURE WORK

We recommend:

1. Additional study of convection currents in crystal growth.

2. Investigate the mechanism of the beneficial effects of vibration.

3. Use of computed results to correlate and explain existing space processing results and to coordinate space crystal growth experiments.

4. Continuation on the improvement of computer programs to develop additional crystal growth models.

5. Additional systemmatic study of combined evaporation and solidification with improved programs.

6. Study why segregation in GaAs and possibly other III-V compounds do not follow the usual phase diagrams.

9. REFERENCES

1. Li, C. H., Phys. Stat. Solidi 15, 3 and 419, 1966.

2. Li, C. H., "Review of Grumman Studies in Metal Solidification," Grumman Research Memorandum RM-525, 1971.

3. Li, C. H., Final Report, NASA Contract NAS 8-27891, Grumman Research Report RE-458, June 1972.

4. Mukerjee, J. L., Gupta, K. P., and Li, C. H., "Evaporative Segregation in 80%-20% Cr and 60%-40% Ni Alloys," Grumman Research Memorandum RM-552, October 1972; J. Vac. Sci. 11, 33, 1974.

5. Mukerjee, J. L., Gupta, K. P., and Li, C. H., "Purification Kinetics of Beryllium during Vacuum Induction Melting," Grumman Research Memorandum RM-553, 1971.

6. Zinsmeister, G., Vakuum-Tech., No. 8, 223, 1964.

7. Li, C. H., "Evaporation in Space Processing," AIAA meeting, Boston, July 1974.

8. Kittel, C. Introduction to Solid State Physics, 3rd Ed. Wiley, N.Y. 1967

9. Swalin, R. A., Thermodynamics of Solids, J. Wiley, N.Y., 1962

10. NASA/MSFC, Third Space Symposium 1974.

11. Cochran, W. G. and Cox, G. M., Experimental Designs, Wiley, N.Y. 1950

12. Tiller, W. A. et al, Acta Met 1, 1428, 1953.

13. Willardson, R. K. and Goering, H. L., Ed, Compound Semiconductors, Van Nostrand, Reinhold, New York, 1962

14. Metals Handbook, ASM, 8th Ed., 1961, p44.

15. Anderson, R.L. and Bancroft, T. A., Statistical Theory in Research, McGraw Hill, New York, 1952.

16. Bennett, C. A. and Franklin, N.L. Statistical Analysis in Chemistry and the Chemical Industry, Wiley, N.Y. 1954.

17. IBM, System/360 Scientific Subroutine Package, Programmer Manual H 20-0205, 1966

18. Pohl, R. G., Jour Appl Phys. 25, 668 and 1170, 1954

19. Hansen, M., Constitution of Binary Alloys, McGraw Hill, New York, 1958

20. Illegens, M. and Pearson, G.L., Proc. 1968 Symp. on GaAs (London: IPPS) pp3-10, 1968

9. REFERENCES (Cont.)

21. Jost, W., Diffusion, Academic, New York, 1952.

22. Nickal, D., Materials Research Corp., Private Communication, 1975.

23. Hollander, M. and Wolfe, D. A., Non-Parametric Statistical Methods, Wiley, New York, 1973.

24. Laudise, R. A., Bell Telephone Lab, Private Communication, 1975.

25. Gato, H, MIT, Private Communication, 1975

26. Anthony, T., et al, Acta Met. 19, 491, 1971

27. Anthony, T., et al, Phil. Mag. 22, 893, 1970

28. Anthony, T., et al, Phil. Mag. 24, 695, 1971

29. Powell, G. L. F., Trans AIME 239, 1244, 1967

30. Marcontonio, J. A., and Mondolfo, L., Met. Trans 5, 1325, 1974.

APPENDIX A

IMPORTANCE OF EVAPORATION

Evaporation is important in space melting and solidification for the following reasons:

- Significant evaporation of alloy components always occurs at high temperatures in space vacuum environments

- High-temperature evaporation of alloys is generally a neglected area of systematic research. Yet, unless the complete evaporative segregation behavior is understood and analyzed, solidification and its related segregation effects may not be properly studied because of ill-defined initial conditions. Before the liquid alloy can be controllably solidified or even melted, there is invariably some surface evaporation to cause changes in composition, freezing temperature, supercooling characteristics, nucleation and growth morphology conditions, and the like

- Controlled space evaporation probably most closely meets the requirements of our model of normal evaporation. We may be able to obtain material purity or evaporation standards, thermal properties, or even such basic thermodynamic properties as heat of evaporation, activity coefficients, and sticking coefficients that are difficult or impossible to obtain on earth

- Evaporation is a much simpler process than freezing, since the former does not involve such complicated phenomena as nucleation, phase transformation, and constitutional or nonconstitutional supercooling. Thus, in normal evaporation for specific geometries or alloy systems, we may ideally isolate and investigate such other phenomena as heat conduction or radiation, liquid or solid diffusion, fluid dynamics, and convection currents. Exact knowledge of these phenomena is necessary to understand solidification

- Evaporation causes surface cooling due to the heat of evaporation. This evaporative cooling effect is particularly important in low-melting materials (Ref. A1)

- Different rates of evaporation at various surface regions give rise to unbalanced forces and momenta that may produce erratic or unwanted accelerations, surface distortions and vibrations, exceedingly large "equivalent gravities," and possibly new types of powerful convection currents in zero-gravity conditions

- Evaporation may cause the surface composition of certain unwanted or unsuspected impurities to be increased a thousandfold or millionfold within seconds so that the layer's melting point and other thermophysical properties, nucleation characteristics, base for undercooling, and critical velocity to

avoid constitutional supercooling may be completely unexpected. In fact, anomalous "constitutional" or evaporative melting on cooling, or solidification on heating, is possible because of surface evaporation. In addition, very large artificial gravities (e.g., 10 g), strong fluid disturbances, or even new and significant convection currents may be produced from surface evaporation. These phenomena have been observed in the M553 movies, according to Dr. Martin Tobin of Westinghouse Co., Pa.

The much greater evaporative segregation effects, if unaccounted for, would almost certainly conceal any minor or subtle zero-gravity effects, particularly in the presence of other unknown or uncontrolled effects. Definitive space solidification work should probably, therefore, be preceded by an evaporative compatibility study of the sample materials and their possible associated impurities. In fact, evaporation is almost certain to be very important or so overwhelming that the effect of zero-gravity or freezing segregation may be masked or even reversed. A freely suspended molten drop in space may, for example, have its surface solute concentration greatly enriched (as much as a millionfold), by neglected and undetectable trace imputities within seconds of its deployment. We are then dealing at the critical surface layer with a completely new and unanticipated alloy having an entirely different composition, melting point, surface tension, thermophysical properties, latent heat of fusion, undercooling and nucleation characteristics, growth morphology, and the like.

From this we can also see that any analytical, computer, or experimental study on solidification may yield completely unexpected or irrelevant results if the important and ever-present evaporation phenomena is not adequately taken care of. This is particularly true in the study of nucleation, undercooling, and space processing. Another important aspect of the present contractual work is to incorporate this generally neglected evaporation phenomena to define the exact initial and boundary conditions before and during the alloy solidification process.

References:

A1. Reichman, J. "Solidification of Metal Spheres in Vacuum," Grumman Research Memorandum RM-544, June 1972.

APPENDIX B

COMPUTER PROGRAM WITHOUT SURFACE EVAPORATION AND RADIATION

Solidification, even in one-g, is a complicated process involving a multitude of interrelated phenomena such as mass and heat transfer, phase change, and fluid motion. Comprehensive reviews on solidification have been given, for example, by Chalmers (Ref. B1), Tiller (Ref. B2), Christian (Ref. B3), and Li (Ref. B4).

Solidification in zero-g is still very complicated. Here, gravitational force is negligibly small, but other effects as a result become important. For example, surface tension often plays a dominant role in determining the sample shape, processing technique and the resulting contamination level of the processed samples. Evaporation is another ever-present, complicating or dominating factor, but one that may be used to advantage when understood. Neglected, or improperly controlled evaporation may drastically change sample surface composition, fluid motion, equivalent gravities, nucleation, and undercooling characteristics as previously described. The previous program, under Contract NAS 8-27891, however, does not deal with evaporation.

Mathematical Definition of Solidification Problem

To understand thoroughly solute segregation either from combined evaporation and solidification, or in single-crystal growth, one requires a complete characterization of the (mass) diffusion and temperature fields in the solid crystal and remaining melt. The zero-gravity effect on the solidification may be overshadowed by other effects invariably present (such as evaporation) in any such growth process – a condition necessitating that such characterization be accurately defined. Unfortunately, the coupled partial differential equations for the diffusion and temperature fields are generally not solvable. Although special case solutions have been given for some types of usually physically nonsatisfying, two-phase Stefan problems, for the general case solution we must resort to numerical computations. Existing numerical methods are always subject to such unrealistic assumptions as constancy of interfacial velocity, temperature or temperature gradients, segregation coefficients, diffusion constants, and other material thermophysical properties.

Under NAS 8-27891, a number of computer programs were developed to study the unidirectional solidification of a binary alloy. These programs employ analytical and numerical methods. The analytic program is based on some closed-form solutions of a simple model and gives results for our numerical program to compare. The model for the analytic program deals with a binary alloy at a constant temperature and concentration throughout the initial liquid melt, with the surface temperature

instantaneously dropped below the liquidus temperature. The liquid-solid interface temperature is assumed constant, and the concentrations of the alloy at the interface are given by the phase diagram having curved liquidus and solidus lines. In addition, the interface boundary plane moves according to a square root law relative to the solidification time. The program also allows the interface temperature and interface boundary to vary from these fixed rules, but in practice the variation is negligible and not above the computer error level (Ref. B5).

Although covered in detail in the final report on NAS 8-27891, the mathematical formulation of the model is presented below for the sake of completeness.

We deal in unidirectional solidification with a liquid binary alloy to be directionally solidified into two phases, liquid and solid. We consider the liquid alloy to be semi-infinite with original (at t = 0) temperature T_o and concentration C_o. Solidification occurs when the temperature at x = 0 is changed from T_o to a lower value T_1, either instantaneously or gradually, so that T_1 is below the temperature T_2 at which the liquid mixture at concentration C_o can be in equilibrium with a solid phase. As solidification occurs, the solid phase grows and its boundary is located at x = y(t), and the interface temperature at this point is $T_i(t)$. The partial differential equations describing the solidification process are the following:

$$a_s^2 \frac{\partial^2 T_s}{\partial x^2} = \frac{\partial T_s}{\partial t}, \quad D_s \frac{\partial^2 C_s}{\partial x^2} = \frac{\partial C_s}{\partial t} \text{ for } 0 < x < y(t) \tag{1}$$

$$a_\ell^2 \frac{\partial^2 T_\ell}{\partial x^2} = \frac{\partial T_\ell}{\partial t}, \quad D_\ell \frac{\partial^2 C_\ell}{\partial x^2} = \frac{\partial C_\ell}{\partial t} \text{ for } y(t) < x < \infty \tag{2}$$

where the variables T, C represent the temperature and concentration (of solute in solvent) and the subscripts ℓ, s denote the liquid and solid phases, respectively. The thermal and mass diffusion coefficients a_s, a_ℓ, D_s, D_ℓ are assumed constant. The following conditions are usually assumed throughout:

(a) $T_\ell\ (x, 0) = T_o$ and $C_\ell\ (x, 0) = C_o$

(b) $T_\ell\ (\infty, t) = T_o$ and $C_\ell\ (\infty, t) = C_o$

(c) $T_s\ (y(t), t) = T_\ell\ (y(t), t) = T_i\ (t)$

(d) $C_s\ (y(t), t) = f_s\ (T_i(t))$

(e) $C_\ell\ (y(t), t) = f_\ell\ (T_i(t))$

(f) $\rho\gamma\dot{y}(t) = k_s \frac{\partial T_s}{\partial x} - k_\ell \frac{\partial T_\ell}{\partial x}$ for x = y(t)

(g) $\left[f_s(T_i(t)) - f_\ell(T_i(t)) \right] \dot{y}(t) = D_\ell \frac{\partial C_\ell}{\partial x} - D_s \frac{\partial C_s}{\partial x}$

for x = y(t)

In many cases, it is also assumed

(h) $y(t) = \alpha \sqrt{t}$.

Equation (a) describes the condition that the original mixture is all liquid at temperature T_o and concentration C_o. Equatinn (b) is a consequence of the semi-infinite nature of the mixture so that at any time t, the portion near infinity is unchanged. Equation (c) assumes that at the solid-liquid interface plane there is an interface temperature $T_i(t)$ and that both the solid and liquid phases at $x = y(t)$ have this temperature. There is no discontinuity in temperature. Equations (d) and (e) state that the concentrations of solid and liquid at the interface are given by the solidus and liquidus curves, respectively, of the constitutional diagram for the alloy. Equation (f) connects the derivative of the moving boundary with the redistribution of temperature and Eq. (g) connects the same boundary with that of concentration. Equation (h) relates the position of the interface boundary to the solidification time t.

The conditions on $T_s(0, t)$ and $C_s(0, t)$ are not fixed in our discussion, and a number of alternatives are considered:

1. $T_s(0, t) = T_1(t)$ with $T_1(t)$ equal to a constant for all t;

2. linear, $T_1(t) = T_o + t(T_1 - T_o)/s$ for $t < s$ and $T_1(t) = T_1$ for $t \geq s$;

3. exponential, $T_1(t) = T_1 + (T_o - T_1)\, e^{-t/s}$ so $T_1(0) = T_o$ and $T_1(\infty) = T_1$.

For $C_s(0, t)$ the conditions considered are $C_s(0, t) = C_1$ usually taken $C_s(T_2)$ or at times a condition conserving mass between 0 and ∞.

The two approaches we have pursued may be designated as analytic and numerical. The numerical approach can be applied to all three conditions on temperature whereas the analytic approach holds only the case of constant temperature instantaneously applied. A variant of this analytic method to apply to linear varying temperature has been investigated.

An analytic solution to the coupled partial differential equations (1) and (2) subject to the initial and boundary conditions (a) through (g) has been given (Ref. B6). A numerical program has been designed for the analytic solution.

These numerical programs developed under NAS 8-27891 are based upon finite difference approximations of the partial and ordinary derivatives and involve a variable spacing (for improved computing efficiency). The programs have given acceptable results and compared well with the reference analytic solution, where comparable. The basic physical properties such as densities, diffusivities, specific heats, thermal conductivities, and heat of fusion have been held to be constant, and independent of temperatures and concentrations.

References

B1 Chalmers, B., Solidification, Wiley, New York, 1969.

B2 Tiller, W., "Solidification" in Physical Metallurgy, Ed. R. W. Cahn, Wiley, New York, 1965, pp. 385-441.

B3 Christian, J. W., The Theory of Transformations in Metals and Alloys, Pergamon Press, New York, 1965, pp. 527-593.

B4 Li, C. H., "Freezing Segregation in Alloys," Materials Science Series, Ed. H. H. Herman, Academic Press, New York, 1975.

B5 Li, C. H., Final Report, NASA contract NAS8-27891 Grumman Research Report RE-458, June 1972.

B6 Rubenstein, L. I., The Stefan Problem, Amer. Math. Soc., Prividence, Rhode Island, 1971.

APPENDIX C

IMPROVED COMPUTER PROGRAM

The complete computer program for the generalized solidification problem is listed herein, together with a glossary explaining the special names used in the program. This computer program has the following unique features:

- Surface evaporation, and its related effects such as material loss, evaporative segregation, and surface cooling due to the heat of evaporation, have been considered
- Material parameters such as solid and liquid densities, specific heats, thermal conductivities, mass diffusivities, and latent heat of fusion or evaporation, are allowed to vary with the temperature and composition
- Realistic phase diagrams involving curved liquids and solidus lines are used
- Two moving boundaries are involved, i. e., the evaporative boundary and freezing boundary
- Surface temperature is determined by the combined effect of heat radiation, evaporative cooling, and thermal diffusion

Use of Computer Program

The computer program works well if the following three input program parameters are properly chosen: 1) time step size (DELT), 2) grid spacing (DELX), and 3) maximum iteration count (NIT).

The solidification boundary is sensitive to the grid spacing. This is because in passing through a mesh point, discontinuity in the computation occurs for the following reasons. We compute the derivatives in terms of the temperatures and concentrations at the discrete mesh points. When one mesh point is dropped because solidification occurs near it, the derivative based on a substituting new mesh point is discontinuous with that based on the previous mesh point. Though this discontinuity can be reduced by using a smaller time step size, it would be a self-defeating strategy. An alternative is to accept the discontinuous results as they occur, advantages being taken of the fact that the program corrects itself. Although the derivative dz/dt is large when the solid-liquid interface passes through a mesh point, it becomes smaller thereafter thereby correcting the solidification boundary position.

The frequency of this self-correction depends on the grid spacing. Too small a grid spacing would cause too frequent self-corrections. Too large a grid spacing, on the other hand, would obscure the rapid temperature variations around the solidification boundary. This indicates that a proper choice of the grid spacing is required to

achieve an optimal tradeoff between accuracy and computing time. There is another tradeoff between the time step size and maximum iteration count for optimal computing results (see Tables C1-C3).

Since each evaporation-solidification problem represents a different and unique physical situation, each case must be dealt with separately. However, based on our experience, the following guidelines would be helpful:

The first consideration for the choice of the grid spacing is the behavior of the evaporation boundary after solidification begins. If the evaporation boundary is virtually stationary as compared to the solidification boundary, the grid spacing should be chosen so that the evaporation boundary is within the first mesh interval (between the first and second mesh points). If, on the other hand, the evaporation boundary is moving at velocities comparable to those of the solidification boundary, then the grid spacing can be selected more freely. The major consideration in this case is the relationship between the grid spacing and the time step size. For a fixed time step size, the grid spacing should be chosen so that at least four time intervals (of step sizes) occur before the solidification boundary passes through a mesh point.

In cases where the evaporation boundary is virtually stationary, one must experiment to determine an optimum time step size in terms of accuracy and computing time. The conditions of the experiment are as follows. Set both the minimum time step size (DELTM) and the time printing interval (DELP) to zero. Setting the time printing interval to zero will cause the computer to print out every computer time step. Setting the minimum time step size to zero will not cause the program to cut back indefinitely but will use, as the minimum, the time step size divided by 1024. By examining the computed results, one can see at what time step sizes the program is running. By examining the actual iteration count (IT), one can see if the program is converging or not. If not converging repeatedly, a smaller time step size is indicated. If the program is converging most of the time, then the minimum time step size can be set at the level of the most frequent time step size and the actual iteration count reexamined to see if the program still converges most of the time. For long runs, the time printing interval must not be zero or small, but must be chosen in consideration with the amount of the required output.

To improve the computing time on long runs, one should consider enlarging the grid spacing as suggested above as one of the tradeoffs. In addition, one may change the maximum iteration count upwards or downwards to also improve the computing time.

Our computer program has the capability for assuming equal or unequal (doubling) mesh point spacings. Our experience, as indicated in Tables C-1 to C-4, shows that the unequal spacing scheme gives practically the same accuracy with far less computations as compared with the equal spacing scheme. This may be due to the rapidity at which the temperature declines at the evaporation boundary. Other physical situations may give different results and may indicate that the equal spacing scheme should be used.

The program input parameters consist of a set of integers IX, IAM, NIT, IM, and NONCN; and a set of real numbers DELX, DELT, DELTM, DELP, TF, and S. IX is the maximum number of mesh points to be used in the program. Present, IX 28.

IAM is the spacing option indicator. If IAM equals 0, the points of mesh are equally spaced with grid spacing DELX. If IAM = 1, an unequal spacing is indicated. The first two intervals are equal and set to DELX. Thereafter, each interval is double the previous interval in spacing. NIT is the maximum number of iterations as interpreted in the context of halving the time step size. If the step is begun at the minimum time step, the NIT is the maximum number of iterations allowed. IM is the number of mesh points in actual use. The input value of IM introduces the minimum number of mesh points to be used. Thereafter additional mesh points are added as required by a substantial change in temperature at next to last mesh point, that is, 1 degree below the initial temperature. IM is increased until IM is equal to IX.

Table C-1. Variation of Temperature (^{o}C) at Evaporative Boundary For Various Computation Schemes

Scheme	I	II	III	IV	V
Grid Spacing	0.01 equal	0.01 unequal	0.001 equal	0.001 unequal	0.0001 cm unequal
time, ms					
0.2	966.5	966.5	966.5	966.5	966.5
0.6	959.4	959.4	959.4	959.4	959.5
1.4	945.7	945.7	945.7	945.7	945.8
1.8	938.9	938.9	938.9	938.9	939.0
2.0	935.5	935.5	935.5	935.5	935.6
2.05	934.7	934.7	934.7	934.7	N.C.
2.075	934.2	934.2	934.2	934.2	N.C.
2.0875	934.0	934.0	934.0	934.0	N.C.
2.09375	933.9	933.9	933.9	933.9	N.C.
2.1	933.8	933.8	933.8	933.8	933.9
2.1125	933.6	933.6	933.6	933.6	933.7*
2.1375	933.2	933.2	933.2	933.2	933.3*
2.1875	932.4	932.4	932.4	932.4*	932.5*
2.2875	930.8	930.8	930.8	930.8*	930.9*
2.4875	927.7	927.7	927.2	927.7*	927.7*
2.8875	921.5	921.5	921.5	921.5*	921.5*
3.6875	909.3	909.3	909.3	909.3*	909.3*
5.2875	885.8	885.8	885.8		

*Hand interpolations
N.C. not computed

Table C-2. Variation of Position (m) of Evaporative Boundary With Time For Various Computation Schemes

Scheme	I	II	III	IV	V
Grid Spacing	0.01 equal	0.01 unequal	0.001 equal	0.001 unequal	0.0001 cm unequal
time, ms					
0.2	0.122	0.122	0.122	0.122	0.122
0.6	0.351	0.351	0.351	0.351	0.351
1.4	0.752	0.752	0.752	0.752	0.752
1.8	0.927	0.927	0.927	0.927	0.928
2.0	1.009	1.009	1.009	1.009	1.010
2.05	1.029	1.029	1.029	1.029	N. C.
2.075	1.039	1.039	1.039	1.039	N. C.
2.0875	1.044	1.044	1.044	1.044	N. C.
2.09375	1.046	1.046	1.047	1.047	N. C.
2.1	1.047	1.047	1.047	1.047	1.050
2.1875	1.048	1.048	1.048	1.048*	1.052
2.2875	1.049	1.049	1.049	1.048*	1.053
2.4875	1.051	1.051	1.051	1.050*	1.055
2.8875	1.055	1.055	1.055	1.054*	1.059
3.6875	1.061	1.061	1.062	1.061	1.066
5.2875	1.072	1.072	1.072	–	–

*Hand interpolations
N. C. not computed

Table C-3. Variation of Position (μm) of Solid-Liquid Interface

Scheme	I	II	III	IV	V
Grid Spacing	0.01 equal	0.01 unequal	0.001 equal	0.001 unequal	0.0001 cm unequal
time, ms					
0.21	0.205	0.204	0.109	0.109	0.106
0.24875	0.211	0.211	0.179	0.180	0.408
0.28875	0.229	0.229	0.350	0.350*	1.03
0.36875	0.283	0.283	0.866	0.860*	2.76
0.52875	0.429	0.429	2.291	N. C.	N. C.

Table C-4. Variation of Temperature (^{o}C) At Solid-Liquid Interface

Scheme	I	II	III	IV	V
Grid Spacing	0.01 equal	0.01 unequal	0.001 equal	0.001 unequal	0.0001 cm unequal
time, ms					
0.21	933.8	933.8	933.8	933.8	933.9
0.24875	927.7	927.7	927.7	927.7*	927.9*
0.28875	924.5	921.4	921.5	921.4*	921.6*
0.36875	909.3	909.3	909.3	909.3*	909.4*
0.52875	885.8	885.8	885.8		

*Hand interpolations
N. C. not computed

NONCN is a nonconvergence option. Failure to converge occasionally is not necessarily an indication of unacceptable results. Therefore, it is desirable to continue computations and examine the results to see if they are acceptable. This is done by setting NONCN to 1. If NONCN is set at 0, the nonconvergent results are not printed unless called for by the print interval. If NONCN is -1, the program stops on nonconvergent results.

The quantity DELX is the grid spacing. Equal spacing and unequal double spacing both make use of this quantity as indicated in the discussion of IAM. The quantity DELT is the maximum time interval (step size) for computation. The quantity DELTM is the input minimum time interval. The program uses as its actual minimum the larger of the quantities DELT/1024 and DELTM. Thus, even if DELTM is set at 0, the number of halving on cutting back the time interval is at most 10 ($2^{10} = 1024$). The program in its presolidification phase starts with its actual time step DELTS set to DELT/8 and allows it to build up to DELT by quick convergence.

On the other hand, near the beginning of solidification, DELTS is allowed to cut back to as small as DELT/256 in order to find an acceptable start of solidification. After solidification has begun, then the restriction of DELTS is between DELTK and DELT. If halving reduces DELTS below DELTK, it is set to DELTK. The quantity DELP is the print interval. If DELP = 0, then every time step is printed. TPR is the time for outputing results. TPR is set originally to DELP and after printout is reset to TPR + DELP. The program prints results if the time TIME1 at the end of the time step equals or exceeds TPR. The program does not attempt to set DELTS so that TPR = TIME1. This is only a slight inconvenience when the print interval is large as compared to DELTM. Generally, we would like DELTM to be set close to the most frequent DELTS provided that failure to converge does not ensue on a regular basis. TF is the final time of program. This means that if TIME1 equals or exceeds TF, no additional time steps are taken.

The decimal quantity S between 0 and 0.5 is used to determine closeness to a mesh point. If the boundary point (either evaporation or solidification) is such that it exceeds the point that divided the mesh interval surrounding the boundary point in the ratio (1-S)/S, then the mesh reference point for computation is moved to the next mesh point. The introduction of S is to make the transition due to passing a mesh point less abruptly discontinuous. The best values of S are between 0.05 and 0.15. For computations on the solid side of the solidification boundary, we continue to use the old mesh points until the boundary point passes the point that divides the new mesh interval about the solidification point in the ratio S/(1-S). This strategy causes a gradual transition from one mesh point to another. The integers II1, II2 are used as reference point indicators for the solid and liquid sides, respectively. For the evaporation boundary, II3 is used to indicate which points are used. II4 is used only to indicate the first mesh point to the left of the evaporation boundary.

Typical Computer Input

The definitions of the various inputs fed into the computer are given in the Glossary of Program Parameters. Typical input values are as follows:

IX = 28 = maximum number of mesh points

IAM = 1, unequal, doubled grid spacing

NIT = 20, maximum number of iterations

IM = 16, actual number of points in mesh

NONCN = 0, allowing the program to continue when nonconvergence occurs with no special printout of these results.

The alloy phase diagrams are determined from the five constants ET, EA, EB, EC, and ED, which define the liquidus C_ℓ and solidus lines C_s as two functions of the temperature, T:

$$C_\ell(T) = ED \times (ET - T)^2 + EC \times (ET - T)$$

$$C_s(T) = EB \times (ET - T)^2 + EA \times (ET - T)$$

In our example of 10 mole percent ($C_o = 0.10$) of antimony in germanium initially uniform at 970°C ($T_o = 970$)

ET = melting point of pure germanium = 956° C

EA = 0.128812×10^{-3}

EB = -0.82218×10^{-7}

EC = 0.466678×10^{-2}

ED = -0.60466×10^{-5}

The evaporation constants for the solvent and solute as defined previously under "The Equation at the Evaporative Boundary" are:

AU = $A_u = 0.1115 \times 10^2$

BU = $B_u = 0.863 \times 10^4$

EMU = $M_u = 0.2435 \times 10^3$

AV = $A_v = 0.1171 \times 10^2$

BV = $B_v = 0.1803 \times 10^5$

EMV = $M_v = 0.726 \times 10^2$

EK = $K_e = 5.833 \times 10^{-4}$

The diffusion coefficient of the solute in solvent in the solid and liquid states are, respectively

DS $= D_s = 0.10 \times 10^{-6}$

DL $= D_\ell = 0.10 \times 10^{-3}$

The density ρ, and latent heat of evaporation, γ, of the pure solvent are, respectively,

RHO $= \rho_v = 5.32$

GAMMA $= \gamma_v = 160$

Corresponding values for pure solute are:

RHOU $= \rho_u = 6.68$

GAMMAU $= \gamma_u = 39$

The above give two derived quantities:

ALS $= a_\ell^2 = k_\ell / \rho_v c$

ASS $= a_s^2 = k_s / \rho_v c$

where

CEE $= c = 0.740 \times 10^{-1}$ = specific heat

The two input parameters in the surface radiation terms are:

EE $= \epsilon = 0.55$ = emissivity coefficient, and

SIG $= \sigma = 0.136 \times 10^{-7}$ = Stefan-Boltzmann constant.

Computer Output

The first line of computer outputs gives the program input parameters IX, IAM, NIT, IM, and NONCN, which are defined previously and also in the "Glossary." The next two lines of computer output give the phase diagram constants (ET, EA, EB, EC, and ED) and evaporation constants (AU, BU, EMU, AV, BV, EMV, and EK), respectively. The next printouts are for CEE, DS, DL, TO, CO, XKL, RHO, GAMMA, RHOU, GAMMAU, EE, SIG, T2, and COO, where T2 is the temperature when solidification begins for the melt of initial solute concentration CO.

The computed numbers are then outputed as follows:

IT = actual iteration count

IM = number of points in mesh

II1 = grid point reference for solid side of mesh

II2 = grid point reference for liquid side of mesh

II3 = grid point reference for evaporation boundary

II4 = grid point reference for point after evaporation boundary

These printouts are then followed by the computed values associated with the evaporation boundary: time, location y, concentration C, temperature T, extent of points X(IM), current time interval DELTS, dy/dt DYDT1, dC/dt DCDT1, dT/dt DTDT1. If solidification has not begun, then there is no information about the solidification boundary. Otherwise, we have position of the solidification boundary z computer language (ZI1), solid solute concentration C_s (CS1), liquid solute concentration C_ℓ (CL1), temperature T (TI1), and rate of movement dz/dt (DZDT1). All decimal outputs are five per line with excess going to the next lines.

Representative Computed Results

The study of the effect of varying the grid spacing DELX on the computed results is summarized in Tables 1 through 4. The five cases considered are:

Case I: DELX = 0.01 cm with equal spacing

Case II: DELX = 0.01 cm with unequal spacing

Case III: DELX = 0.001 cm with equal spacing

Case IV: DELX = 0.001 cm with unequal spacing

Case V: DELX = 0.0001 cm with unequal spacing

APPENDIX D

AN IMPROVED COMPUTER PROGRAM

```
      DIMENSION X(28),T(28),TT(28),C(28),CC(28),                        BIN00010
     *TEM(10)      ,A(84)                                               BIN00020
      NAMELIST /INVAR/CEE,DS,DL,T0,C0,XKL,RHO,GAMMA,RHOU,GAMMAU,EE,SIG  BIN00030
     *,ET,EA,EB,EC,ED,AU,BU,EMU,AV,BV,EMV,EK,IX                         BIN00040
      D2(X,F,Y,G,Z,H)=((H-G)/(Z-Y)-(F-G)/(X-Y))/(Z-X)*2.                BIN00050
      ABS1(X)=AMAX1(1.,ABS(X))                                          BIN00060
      UE(V)=EK*(10.**(AU-BU/(273.12+V)))/SQRT(EMU*(273.12+V))           BIN00070
      VE(V)=EK*(10.**(AV-BV/(273.12+V)))/SQRT(EMV*(273.12+V))           BIN00080
      FS(V)=(EB*(ET-V)+EA)*(ET-V)                                       BIN00090
      FL(V)=(ED*(ET-V)+EC)*(ET-V)                                       BIN00100
      XCL(V)=ET-2.*V/(EC+SQRT((EC)**2+4.*(ED)*(V)))                     BIN00110
      XCSL(V)=ET+2.*V/((EC-EA)+SQRT((EA-EC)**2+4.*(EB-ED)*V))           BIN00120
      DFL(V)=-(2.*ED*(ET-V)+EC)                                         BIN00130
      II=1                                                              BIN00140
      IO=8                                                              BIN00150
      READ(II,100) IX,IAM,NIT,IM,NONCN                                  BIN00160
  100 FORMAT (16I5)                                                     BIN00170
      NITH=NIT/2                                                        BIN00180
      NITQ=NITH/2                                                       BIN00190
      NITL=NITH+NITQ                                                    BIN00200
   64 READ(II,101) ET,EA,EB,EC,ED                                       BIN00210
      AQUAN=-(EA-EC)**2/(4.*(EB-ED))                                    BIN00220
  101 FORMAT(7E10.0)                                                    BIN00230
      READ(II,101) AU,BU,EMU,AV,BV,EMV,EK                               BIN00240
      READ(II,101) CEE,DS,DL,T0,C0,XKL,RHO,GAMMA    ,RHOU,GAMMAU,EE,SIG BIN00250
      ALS=XKL/(RHO*CEE)                                                 BIN00260
      XKS=1.1*XKL                                                       BIN00270
      ASS=1.1*ALS/1.03                                                  BIN00280
      AS=SQRT(ASS)                                                      BIN00290
      AL=SQRT(ALS)                                                      BIN00300
      READ(II,101) DELX,DELT,DELTM,DELP,TF,S                            BIN00310
      DELTK=AMAX1(DELTM,DELT/1024.)                                     BIN00320
      T2=XCL(C0)                                                        BIN00330
      C00=FL(T2)                                                        BIN00340
  201 DO 1 I=1,IX                                                       BIN00350
      IF(I-2) 2,3,4                                                     BIN00360
    2 X(1)=0.                                                           BIN00370
      GO TO 1                                                           BIN00380
    3 X(2)=DELX                                                         BIN00390
      GO TO 1                                                           BIN00400
    4 IF(IAM) 5,5,6                                                     BIN00410
    5 X(I)=X(I-1)+DELX                                                  BIN00420
      GO TO 1                                                           BIN00430
    6 X(I)=X(I-1)+X(I-1)                                                BIN00440
    1 CONTINUE                                                          BIN00450
  999 WRITE(IO,100)IX,IAM,NIT,IM,NONCN                                  BIN00460
      WRITE(IO,102)ET,EA,EB,EC,ED                                       BIN00470
      WRITE(IO,102)AU,BU,EMU,AV,BV,EMV,EK                               BIN00480
      WRITE(IO,102)CEE,DS,DL,T0,C0,XKL,RHO,GAMMA ,RHOU,GAMMAU,EE,SIG,T2,BIN00490
     *C00                                                               BIN00500
      TPR=DELP                                                          BIN00510
      RAT=1.                                                            BIN00520
      TSI1=T0                                                           BIN00530
      TI1=T0                                                            BIN00540
      CSL1=C0                                                           BIN00550
```

```
      YI1=0.                                                            BIN00560
      ZI1=0.                                                            BIN00570
      II1=2                                                             BIN00580
      II2=2                                                             BIN00590
      II3=2                                                             BIN00600
      D2T2=0.                                                           BIN00610
      D2T3=0.                                                           BIN00620
      D2T4=0.                                                           BIN00630
      D2C3=0.                                                           BIN00640
      D2C4=0.                                                           BIN00650
      D2C2=0.                                                           BIN00660
      D2T1=0.                                                           BIN00670
      D2C1=0.                                                           BIN00680
      DCLDX=0.                                                          BIN00690
      DTSDX=0.                                                          BIN00700
      D2C5=0.                                                           BIN00710
      D2T5=0.                                                           BIN00720
      D2C6=0.                                                           BIN00730
      D2T6=0.                                                           BIN00740
      TIME =0.                                                          BIN00750
      DCDX0=0.                                                          BIN00760
      DTDX0=0.                                                          BIN00770
      DELTS=DELT/8.                                                     BIN00780
        TIME1=TIME+DELTS                                                BIN00790
      DO 10 I=  1,IM                                                    BIN00800
      C(I)=C0                                                           BIN00810
      CC(I)=C0                                                          BIN00820
      TT(I)=T0                                                          BIN00830
   10 T(I)=T0                                                           BIN00840
      IFL=0                                                             BIN00850
      IFS=0                                                             BIN00860
      III=II2                                                           BIN00870
   14 IT=0                                                              BIN00880
      IF(IFS.EQ.1)GO TO 199                                             BIN00890
      IF(IFL) 11,11,20                                                  BIN00900
   11 U0=UF(T0)                                                         BIN00910
      V0=VF(T0)                                                         BIN00920
      IFL=1                                                             BIN00930
  199 IF(IFS.NE.0)CSL1=CS1                                              BIN00940
      IF(IFS.EQ.1)IFS=2                                                 BIN00950
      DYDT0=U0*EMU*CSL1/RHOU+V0*EMV*(1.-CSL1)/RHO                       BIN00960
       HB0=-EE*SIG*(273.12+TSI1)**4-U0*GAMMAU*CSL1-V0*GAMMA*(1.-CSL1)   BIN00970
      DCDT0=DCDX0*DYDT0-(U0-V0)*CSL1                                    BIN00980
      DTDT0=DTDX0*DYDT0+HB0                                             BIN00990
   20 YI2=YI1+DELTS*DYDT0                                               BIN01000
      IF(IFS.EQ.0)ZI2=YI2                                               BIN01010
      IF(IFS.NE.0)ZI2=ZI1+DELTS*DZDT0                                   BIN01020
      IF(ZI2.GT.X(II2+1))ZI2=(X(II2)+YI2)/2.                            BIN01030
      TSI2=TSI1+DELTS*DTDT0                                             BIN01040
      TI2=TSI2                                                          BIN01050
      CSL2=CSL1+DELTS*DCDT0                                             BIN01060
      IF(IFS.EQ.0)CL2=CSL2                                              BIN01070
   77 IF(IFS.EQ.0)GO TO 777                                             BIN01080
      IF (IFL.GT.1)GO TO 877                                            BIN01090
      IIT=0                                                             BIN01100
```

```
877 CS2=FS(TI2)                                                        BIN01110
    CL2=FL(TI2)                                                        BIN01120
777 D2C2=D2(ZI2,CL2,X(II2),CC(II2),X(II2+1),CC(II2+1))                 BIN01130
    CC(II2)=(CC(II2)+C(II2)+.5*DELTS*(D2C1+D2C2)*DL      )/2.          BIN01140
     CALL MOTON(X(II2),CC(II2),ZI2,CL2,X(II2+1),CC(II2+1))             BIN01150
    IF(ZI2.LT.X(II2-1))CC(II2-1)=CC(II2)+(X(II2-1)-X(II2))*            BIN01160
   *(CL2-CC(II2))/(ZI2-X(II2))                                         BIN01170
    IF(II1-II3-1)83,87,84                                              BIN01180
 87 XP=YI2                                                             BIN01190
    CP=CSL2                                                            BIN01200
    GO TO 184                                                          BIN01210
 84 XP=X(II1-2)                                                        BIN01220
    CP=CC(II1-2)                                                       BIN01230
184 D2C4=D2(XP,CP,X(II1-1),CC(II1-1),ZI2,CS2)                          BIN01240
    CC(II1-1)=C(II1-1)+.5*DELIS*(D2C3+D2C4)*DS                         BIN01250
    CALL MOTON(X(II1-1),CC(II1-1),XP,CP,ZI2,CS2)                       BIN01260
 83 IF(II2.EQ.II1.OR.ZI2.LT.X(II2-1)) GO TO 85                         BIN01270
    IF(II2-II3.GT.1)GO TO 185                                          BIN01280
    XP=YI2                                                             BIN01290
    CP=CSL2                                                            BIN01300
    GO TO 51                                                           BIN01310
185 XP=X(II2-2)                                                        BIN01320
    CP=CC(II2-2)                                                       BIN01330
 51 CC(II2-1)=CP+(X(II2-1)-XP)*(CS2       -CP)/                        BIN01340
   *(ZI2      -XP)                                                     BIN01350
 85 D2T2=D2(ZI2,TI2,X(II2),TT(II2),X(II2+1),TT(II2+1))                 BIN01360
    IF (D2T2.GT.0.)D2T2=0.                                             BIN01370
    TT(II2)=(TT(II2)+T(II2)+.5*DELTS*(D2T1+D2T2)*ALS      )/2.         BIN01380
    CALL MOTON(X(II2),TT(II2),ZI2,TI2,X(II2+1),TT(II2+1))              BIN01390
    IF (IFS.EQ.0)GO TO 485                                             BIN01400
485 IF(ZI2.LT.X(II2-1))TT(II2-1)=TT(II2)+(X(II2-1)-X(II2))*            BIN01410
   *(TI2-TT(II2))/(ZI2-X(II2))                                         BIN01420
    IF(II1-II3-1) 69,169,269                                           BIN01430
169 TP=TSI2                                                            BIN01440
    XP=YI2                                                             BIN01450
    GO TO 16                                                           BIN01460
269 TP=TT(II1-2)                                                       BIN01470
    XP=X(II1-2)                                                        BIN01480
 16 D2T4=D2(XP,TP,X(II1-1),TT(II1-1),ZI2,TI2)                          BIN01490
    TT(II1-1)= T(II1-1)+.5*DELTS*(D2T3+D2T4) *ASS                      BIN01500
    CALL MOTON(X(II1-1),TT(II1-1),XP,TP,ZI2,TI2)                       BIN01510
 69 IF(II2.EQ.II1.OR.ZI2.LT.X(II2-1)) GO TO 86                         BIN01520
 52 IF(II2.LT.II3-1)GO TO 186                                          BIN01530
    XP=YI2                                                             BIN01540
    TP=TSI2                                                            BIN01550
    GO TO 352                                                          BIN01560
186 XP=X(II2-2)                                                        BIN01570
    TP=TT(II2-2)                                                       BIN01580
352 TT(II2-1)=TP +(X(II2-1)-XP)*(TI2       -TP)/                       BIN01590
   *(ZI2      -XP)                                                     BIN01600
 86 IF(IFS.EQ.0)GO TO 299                                              BIN01610
    DCLDX=(CL2-CC(II2))/(ZI2-X(II2))                                   BIN01620
    IF (D2C2.GT.0.) DCLDX=DCLDX-D2C2*(X(II2)-ZI2)/2.                   BIN01630
    IF (D2C2.LT.0.)D2C2=0.                                             BIN01640
    DTLDX=(TI2-TT(II2))/(ZI2-X(II2))                                   BIN01650
```

```
      IF (D2T2.LT.0.)DTLDX=DTLDX-.5*D2T2*(X(II2)-ZI2)                    BIN01660
      IF(II3.EQ.II1)GO TO 386                                            BIN01670
      XP=X(II1-1)                                                        BIN01680
      TP=TT(II1-1)                                                       BIN01690
      CP=CC(II1-1)                                                       BIN01700
      GO TO 486                                                          BIN01710
  386 XP=YI2                                                             BIN01720
      TP=TSI2                                                            BIN01730
      CP=CSL2                                                            BIN01740
      DCSDX=(CS2-CP)/(ZI2-XP)                                            BIN01750
      DTSDX=(TI2-TP)/(ZI2-XP)                                            BIN01760
      GO TO 686                                                          BIN01770
  486 DCSDX=(CP-CS2)/(XP-ZI2)   -D2C4*(XP-ZI2)/2.                        BIN01780
      DTSDX=(TP-TI2)/(XP-ZI2)-D2T4*(XP-ZI2)/2.                           BIN01790
  686 DZDT=(DL*DCLDX-DS*DCSDX)/(CS2-CL2)                                 BIN01800
       DZDTT=(XKS*DTSDX-XKL*DTLDX)/(RHO*GAMMA)                           BIN01810
      FSL=DZDT*(CS2-CL2)/DZDTT                                           BIN01820
      IF(FSL.GT.0..OR.FSL.LT.AQUAN )GO TO 772                            BIN01830
      TII=XCSL(FSL)                                                      BIN01840
      GO TO 771                                                          BIN01850
  772 TII=RT                                                             BIN01860
  771 COE1=XKS/(ZI2-XP)                                                  BIN01870
      COE2=XKL/(X(II2)-ZI2)                                              BIN01880
  586 TI=(RHO*GAMMA*DZDT+COE1*(TP-D2T4*.5*(XP-ZI2)**2)+COE2*(TT(II2)-.5  BIN01890
     **D2T2*(X(II2)-ZI2)**2))/(COE1+COE2)                                BIN01900
  773 IF (TI.LT.TSI2.AND.TI.LT.TII)TI=TII                                BIN01910
      IF (TI.LT.TSI2.OR.TI.GT.TT(II2+1))TI=TT(II2)                       BIN01920
      IF (DZDT.LT.0..AND.DZDTT.GT.0.)  DZDT=DZDTT                        BIN01930
      IF(ABS(TI-TI2)-1.E-5*ABS1(TI+TI2))587,587,770                      BIN01940
  587 IF(ABS(DZDT-DZDT1)-1.E-3*ABS1(DZDT+DZDT1))298,298,770              BIN01950
  770 TI2=(TI+TI2)/2.                                                    BIN01960
      IF (DZDT .LT.0.)DZDT=DZDT1                                         BIN01970
      DZDT1=(DZDT+DZDT1)/2.                                              BIN01980
      ZI2=ZI1+.5*DELTS*(DZDT1+DZDT0)                                     BIN01990
      IF(ZI2.GT.X(II2+1))ZI2=(X(II2)+YI2)/2.                             BIN02000
      IIT=IIT+1                                                          BIN02010
      IF(IIT.GT.5)  GO TO 298                                            BIN02020
      GO TO 877                                                          BIN02030
  298 IF(TI.GT.TT(II2))TI=TT(II2)                                        BIN02040
      IF(TI.LT.TSI2)TI=TSI2                                              BIN02050
      IF(II1-II3-1)398,498,598                                           BIN02060
  598 D2T6=D2(YI2,TSI2,X(II3),TT(II3),X(II3+1),TT(II3+1))                BIN02070
      D2C6=D2(YI2,CSL2,X(II3),CC(II3),X(II3+1),CC(II3+1))                BIN02080
      DTDX1=(TSI2-TT(II3))/(YI2-X(II3))-D2T6*(X(II3)-YI2)/2.             BIN02090
      DCDX1=(CSL2-CC(II3))/(YI2-X(II3))-D2C6*(X(II3)-YI2)/2.             BIN02100
      GO TO 599                                                          BIN02110
  498 DTDX1=DTSDX+D2T4*(XP-ZI2)                                          BIN02120
      DCDX1=DCSDX+D2C4*(XP-ZI2)                                          BIN02130
      D2T6=D2T4                                                          BIN02140
      D2C6=D2C4                                                          BIN02150
      GO TO 599                                                          BIN02160
  398 DCDX1=DCSDX                                                        BIN02170
      DTDX1=DTSDX                                                        BIN02180
      GO TO 599                                                          BIN02190
  299 DTDX1=(TT(II2)-TI2)/(X(II2)-YI2)-.5*D2T2*(X(II2)-YI2)              BIN02200
```

```
      DCDX1=(CC(II2)-CL2)/(X(II2)-YI2)-.5*D2C2*(X(II2)-YI2)                BIN02210
  599 U1=UE(TSI2)                                                         BIN02220
      V1=VE(TSI2)                                                         BIN02230
      HB1=-EE*SIG*(273.12+TSI2)**4-U1*GAMMAU*CSL2-V1*GAMMA*(1.-CSL2)      BIN02240
      DYDT1=U1*EMU*CSL2/RHOU+V1*EMV*(1.-CSL2)/RHO                         BIN02250
      DCDT1=DCDX1*DYDT1-(U1-V1)*CSL2                                      BIN02260
      DTDT1=DTDX1*DYDT1+HB1                                               BIN02270
      IF (IFL.LT.2) GO TO 76                                              BIN02280
      IF(IFS.GE.1)GO TO 174                                               BIN02290
      IF(TSI2.GT.TT(II2)) GO TO 399                                       BIN02300
      TT2=XCL(CSL2)                                                       BIN02310
      IF(TSI2.GT.TT2) GO TO 174                                           BIN02320
      IF(TSI2.GE.TT2-.05)GO TO 400                                        BIN02330
      IF (DELTS.LE.DELTK) GO TO 400                                       BIN02340
      GO TO 399                                                           BIN02350
   76 YI=YI1+.5*(DYDT0+DYDT1)*DELTS                                       BIN02360
      IF(IFS.EQ.0)ZI=YI                                                   BIN02370
      TSI =TSI1+.5*(DTDT0+DTDT1)*DELTS                                    BIN02380
      IF(TSI.LT.0.)TSI=TSI1                                               BIN02390
      CSL=CSL1+.5*(DCDT0+DCDT1)*DELTS                                     BIN02400
      IF (IFS.EQ.0) GO TO 73                                              BIN02410
      IF(IIT.GT.5)GO TO 70                                                BIN02420
      IF(TSI.GT.TT(II2).OR.TSI.GT.TI2) GO TO 70                           BIN02430
   73 IF(ABS(YI-YI2)-1.E-6*ABS1(YI+YI2))74,74,70                          BIN02440
   74 IF(ABS(CSL-CSL2)-1.E-4*ABS1(CSL+CSL2))75,75,70                      BIN02450
   75 IF(ABS(TSI-TSI2)-1.E-5*ABS1(TSI+TSI2))7,7,70                        BIN02460
   70 TSI2=(TSI+TSI2)/2.                                                  BIN02470
      IF (IFS.EQ.0)TI2=TSI2                                               BIN02480
      YI2=(YI+YI2)/2.                                                     BIN02490
      IF (IFS.EQ.0)ZI2=YI2                                                BIN02500
      CSL2=(CSL+CSL2)/2.                                                  BIN02510
      IF(IFS.EQ.0)CL2=CSL2                                                BIN02520
      IF(ZI2.LT.(1.-S)*X(II2)+S*X(II2-1)) GO TO 24                        BIN02530
   22 IF(II1-II2) 24,96,96                                                BIN02540
   96 II2=II2+1                                                           BIN02550
   46 D2C1=D2(ZI1,CL1,X(II2),C(II2),X(II2+1),C(II2+1))                    BIN02560
      D2T1=D2(ZI1,TI1,X(II2),T(II2),X(II2+1),T(II2+1))                    BIN02570
   24 IF (IT-NITQ) 48,174,160                                             BIN02580
  160 IF(IT-NITH) 48,47,48                                                BIN02590
   47 IF(DELTS-DELTK) 48,48,53                                            BIN02600
   53 DELTS=DELTS/RAT                                                     BIN02610
  152 IF(RAT-1.) 153,153,154                                              BIN02620
  153 RAT=2.*RAT                                                          BIN02630
       DELTS=DELTS/2.                                                     BIN02640
       GO TO 152                                                          BIN02650
  154 TIME1=TIME+DELTS                                                    BIN02660
  212 DO 45 I=II3,IM                                                      BIN02670
      TT(I)=(TT(I)+(RAT-1.)*T(I))/RAT                                     BIN02680
   45 CC(I)=(CC(I)+(RAT-1.)*C(I))/RAT                                     BIN02690
  148 RAT=1.                                                              BIN02700
   48 IT=IT+1                                                             BIN02710
      IF(IT.EQ.NITH+1)GO TO 20                                            BIN02720
      IF (IT-NITL) 161,174,161                                            BIN02730
  161 IF(IT-NIT) 77,77,402                                                BIN02740
  402 IF(DELTS.GT.DELTK) GO TO 399                                        BIN02750
```

```
      IFL=2                                                              BIN02760
      GO TO 77                                                           BIN02770
   26 IF (NONCN) 99,48,48                                                BIN02780
    7 IFL=IFL+1                                                          BIN02790
      DZDT1=DZDT                                                         BIN02800
      IF(IFS.NE.0) ZI2=ZI1+.5*DELTS*(DZDT0+DZDT1)                        BIN02810
      TSI2=TSI                                                           BIN02820
      YI2=YI                                                             BIN02830
      IF(IFS.EQ.0) ZI2=YI2                                               BIN02840
      CSL2=CSL                                                           BIN02850
      IF (IFS.NE.0) TI2=TI                                               BIN02860
      IF (TI2.LT.TSI2) TI2=TSI2                                          BIN02870
      IF (IFS.EQ.0) TI2=TSI2                                             BIN02880
      IF(IFS.EQ.0) CL2=CSL2                                              BIN02890
      GO TO 77                                                           BIN02900
  399 IF(DELTS.LE.DELTK) GO TO 26                                        BIN02910
      IT=NITH                                                            BIN02920
      IFL=1                                                              BIN02930
      GO TO 153                                                          BIN02940
  117 IF(TIME.EQ.TIME1)TIME1=TIME1    +DELTS                             BIN02950
      TIME=TIME1                                                         BIN02960
       IF (RAT.NE.2..AND.RAT.NE.0.) DELTS=DELTS/RAT                      BIN02970
      RAT=1.                                                             BIN02980
      IF(IT-NITQ) 82,82,81                                               BIN02990
   82 IF(DELTS.GT.DELT/2.) GO TO 81                                      BIN03000
      DELTS=DELTS+DELTS                                                  BIN03010
      RAT=2.                                                             BIN03020
   81 TIME1=TIME1+DELTS                                                  BIN03030
  282 D2C1=D2C2                                                          BIN03040
      D2C3=D2C4                                                          BIN03050
      D2C5=D2C6                                                          BIN03060
      D2T3=D2T4                                                          BIN03070
      D2T1=D2T2                                                          BIN03080
      D2T5=D2T6                                                          BIN03090
      DYDT0=DYDT1                                                        BIN03100
      DCDT0=DCDT1                                                        BIN03110
      U0=U1                                                              BIN03120
      V0=V1                                                              BIN03130
      DTSDX1=DTSDX                                                       BIN03140
      DCSDX1=DCSDX                                                       BIN03150
      IF(IFS.NE.0) DCDX0=DCDX1                                           BIN03160
      IF(IFS.NE.0) DTDX0=DTDX1                                           BIN03170
      IF(IFS.NE.0) DZDT0=DZDT1                                           BIN03180
      CSL1=CSL2                                                          BIN03190
      TSI1=TSI2                                                          BIN03200
      YI1=YI2                                                            BIN03210
      ZI1=ZI2                                                            BIN03220
      IF(IFS.NE.0)CS1=CS2                                                BIN03230
      HB0=HB1                                                            BIN03240
      CL1=CL2                                                            BIN03250
      TI1=TI2                                                            BIN03260
      IF(YI2.LT.X(II3))GO TO 410                                         BIN03270
      II3=II3+1                                                          BIN03280
      D2T5=D2(YI1,TSI1,X(II3),TT(II3),X(II3+1),TT(II3+1))                BIN03290
      D2C5=D2(YI1,CSL1,X(II3),CC(II3),X(II3+1),CC(II3+1))                BIN03300
```

```
 410 IF(II1.EQ.II2.OR.ZI2.LT.S*X(II2)+(1.-S)*X(II2-1))GO TO 33          BIN03310
     II1=II2                                                           BIN03320
     IF(II1-II3-1)33,310, 110                                          BIN03330
 310 XP=YI1                                                            BIN03340
     CP=CSL1                                                           BIN03350
     TP=TSI1                                                           BIN03360
     GO TO 210                                                         BIN03370
 110 XP=X(II1-2)                                                       BIN03380
     CP=CC(II1-2)                                                      BIN03390
     TP=TT(II1-2)                                                      BIN03400
 210 D2C3=D2(XP,CP,X(II1-1),CC(II1-1),ZI1,CL1)                         BIN03410
     D2T3=D2(XP,TP,X(II1-1),TT(II1-1),ZI1,TI1)                         BIN03420
     IF(II1-II3.NE.1)GO TO 33                                          BIN03430
     D2T5=D2T3                                                         BIN03440
     D2C5=D2C3                                                         BIN03450
     GO TO 33                                                          BIN03460
 174 III=II2                                                           BIN03470
     IF(ZI2.LT.X(II2-1))III=III-1                                      BIN03480
     IF (II1-II3.LT.2) GO TO 18                                        BIN03490
     IF(II1-II3.GT.2)GO TO 29                                          BIN03500
     TT(III)=(T(III)/DELTS+.5*ASS*D2T5                                 BIN03510
    *+TT(III+1)*ASS/(X(III+1)-X(III))/(X(III+1)-YI2)+TSI2*ASS/(X       BIN03520
    *(III)-YI2)/(X(III+1)-YI2))/(1./DELTS+ASS/(X(III+1)-YI2)*(1./(X(III3BIN03530
    *+1)-X(III))+1./(X(III)-YI2)))                                     BIN03540
     CC(III)=(C(III)/DELTS+.5*DS*D2C5                                  BIN03550
    *+CC(III+1)*DS/(X(III+1)-X(III))/(X(III+1)-YI2)+CSL2*DS/(X(I       BIN03560
    *I3)-YI2)/(X(III+1)-YI2))/(1./DELTS+DS/(X(III+1)-YI2)*(1./(X(I13+1)BIN03570
    *-X(III))+1./(X(III)-YI2)))                                        BIN03580
     GO TO 18                                                          BIN03590
  29 X(III-1)=(YI2+YI1)/2.                                             BIN03600
     C(III-1)=CSL1                                                     BIN03610
     CC(III-1)=CSL2                                                    BIN03620
     T(III-1)=TSI1                                                     BIN03630
     TT(III-1)=TSI2                                                    BIN03640
     CALL TRIST(X,T,TT,III-1,III-1,ASS,DELTS,A)                        BIN03650
     CALL TRIST (X,C,CC,III-1,III-1,DS,DELTS,A)                        BIN03660
     GO TO 18                                                          BIN03670
  27 IF(T(IM-1)-T0+1.E0)    30,32,32                                   BIN03680
  30 IF (IM-IX) 15,32,32                                               BIN03690
  15 IM=IM+1                                                           BIN03700
     T(IM)=T0                                                          BIN03710
     C(IM)=C0                                                          BIN03720
  32 TT(IM)=T(IM)                                                      BIN03730
     CC(IM)=C(IM)                                                      BIN03740
     GO TO 14                                                          BIN03750
  18 IF(DELTS.LT.DELTK)DELTS=DELTK                                     BIN03760
     CALL TRIST(X,T,TT,III,IM,ALS,DELTS,A)                             BIN03770
     CALL TRIST(X,C,CC,III,IM,  DL,DELTS,A)                            BIN03780
      DO 21 I=II2,IM                                                   BIN03790
      IF (I.EQ.II2) GO TO 21                                           BIN03800
  21 CONTINUE                                                          BIN03810
 219 IF (IFL.EQ.2) GO TO 117                                           BIN03820
     GO TO 48                                                          BIN03830
  33 IF(TIME-TPR) 50,34,34                                             BIN03840
  50 IF (NONCN) 98,98,54                                               BIN03850
```

```
   54 IF(IT-NIT) 98,98,42                                                    BIN03860
   34 IF(DELP.EQ.0.)GO TO 42                                                 BIN03870
      TPR=TPR+DELP                                                           BIN03880
   42 WRITE(IO,100) IT,IM ,II1,II2 ,II3                                      BIN03890
      WRITE(IO,102)TIME,YI1,CSL1,TSI1,U1,V1,HB1,DYDT1,DTDT1,DCDT1,DELTS      BIN03900
      IF(IFS.NE.0)WRITE(IO,102)ZI1,CS1,CL1,TI1,DZDT1                         BIN03910
  143 WRITE(IO,102) (TT(I),I=II3,IM),(CC(I),I=II3,IM)                        BIN03920
  102 FORMAT(5E14.6)                                                         BIN03930
      IF(TIME -TF) 98,99,99                                                  BIN03940
   98 DO 97 I=II3,IM                                                         BIN03950
      TTT=TT(I)+RAT*(TT(I)-T(I))                                             BIN03960
      T(I)=TT(I)                                                             BIN03970
      TT(I)=TTT                                                              BIN03980
   97 CONTINUE                                                               BIN03990
       DO 197 I=II3,IM                                                       BIN04000
      CCC=CC(I)+RAT*(CC(I)-C(I))                                             BIN04010
      C(I)=CC(I)                                                             BIN04020
  197 CC(I)=CCC                                                              BIN04030
       IFL=1                                                                 BIN04040
       GO TO 27                                                              BIN04050
  400 CSS=FS(TI2)                                                            BIN04060
      CLL=FL(TI2)                                                            BIN04070
      DELZ=(CLL-CL2)/((CLL+CC(II2))-2.*CSS)*(X(II2)-YI2)                     BIN04080
      ZI2=YI2+DELZ                                                           BIN04090
      DZDT0=DELZ/DELTS                                                       BIN04100
      DZDT1=DZDT0                                                            BIN04110
      CL2=CLL                                                                BIN04120
      CS2=CSS                                                                BIN04130
      DCDX0=0.                                                               BIN04140
      DTDX0=0.                                                               BIN04150
      DTDX1=0.                                                               BIN04160
      WRITE(IO,103)TIME1,YI2,TI2,ZI2,CS2,CL2,DELZ,DELTS,DZDT0                BIN04170
  103 FORMAT('  SOLIDIFICATION HAS BEGUN '/(5E14.6))                         BIN04180
      IFS=1                                                                  BIN04190
      GO TO 174                                                              BIN04200
   99 READ(II,INVAR)                                                         BIN04210
      IF(IX.GT.0)GO TO 999                                                   BIN04220
      STOP                                                                   BIN04230
      END                                                                    BIN04240
```

GLOSSARY OF PROGRAM PARAMETERS

AS, AL = temperature diffusion coefficients

ASS, ALS = squares of temperature diffusion coefficients

AU, BU, AV, BV, EK = evaporation constants for solute and solvent

CEE = C specific heat

CEEUO = c_{uo} - constant term for specific heat of solute

CEEUT = c_{ut} - linear coefficient for specific heat of solute

CEEVO = c_{vo} - constant term for specific heat of solvent

CEEVT = c_{vT} - linear coefficient for specific heat of solvent

C_{ℓ} = concentration of solid at the start of solidification

CL1, CL2 = concentration of liquid at solid-liquid boundary

COE1 = k_s divided by the interface to the first left mesh point

COE2 = k_{ℓ} divided by the interface to the first right mesh point

COO = equals CO

CS1, CS2 = concentration of solid at solid-liquid boundary

CSL, CSL1, CSL2 = concentration at evaporation boundary

D2C1, D2C2 = $\left(\frac{\partial^2 C_2}{\partial x^2}\right)_z$ at liquid side of solid-liquid boundary

D2C3, D2C4 = $\left(\frac{\partial^2 C_s}{\partial x^2}\right)_z$ at solid side of solid-liquid boundary

D2C5, D2C6 = $\left(\frac{\partial^2 C}{\partial x^2}\right)_y$ at evaporation boundary

D2T1, D2T2 = $\left(\frac{\partial^2 T_2}{\partial x^2}\right)_z$ at liquid side of solid-liquid boundary

D2T3, D2T4 = $\left(\frac{\partial^2 T_s}{\partial x^2}\right)_z$ at solid side of solid-liquid boundary

D2T5, D2T6 = $\left(\frac{\partial^2 T}{\partial x^2}\right)_y$ at evaporation boundary

D3C2 = third derivative approx. $\frac{\partial^3 T}{\partial x^3}$

D3C4 = third derivative approx. $\frac{\partial^3 T}{\partial x^3}$

D3T2 = third derivative approx. $\frac{\partial^3 T}{\partial x^3}$

D3T4 = third derivative approx. $\frac{\partial^3 T}{\partial x^3}$

DCDTO, DCDT1 = $\frac{dC}{dT}$ derivative of concentration at evaporation boundary

DCDX0, DCDX1 = $\left(\frac{\partial C}{\partial x}\right)_y$ partial derivative of concentration at evaporation boundary

DCLDX = $\left(\frac{\partial C_L}{\partial x}\right)_z$ partial derivative of concentration in liquid at solid-liquid boundary

DCLX2 = $\partial c_\ell / \partial x$

DCSDX = $\left(\frac{\partial C_s}{\partial x}\right)_z$ partial derivative of concentration in solid at solid-liquid boundary

DCSX2 = $\partial c_\ell / \partial x$

DELP = time print interval

DELSC = ratio of step size the program wants to use to the computed step size

DELT = maximum time interval (step size)

DELTC = indicated step size for the initial amount of solid

DELTK = larger of quantities DELT/1024 and DELTM

DELTM = minimum time interval

DELTS = current time interval

DELX = length of the first mesh interval (x_0, x_1)

DFL (V) = derivative of liquidus equation

DLC = D_{LC} - linear coefficient for concentration for mass diffusivity of liquid

DLT = D_{LT} linear coefficient for concentration for mass diffusivity of liquid

DLO = D_{LO} - constant term for mass diffusivity of liquid

DS, DL = mass (concentration) diffusion coefficient

DSC = D_{SC} - linear coefficient for concentration for mass diffusivity of solid

DSO = D_{SO} - constant term for mass diffusivity of solid

DST = D_{ST} - linear coefficient for temperature for mass diffusivity of solid

DTDT0, DTDT1 = $\frac{dT}{dt}$ derivative of temperature at evaporation boundary

DTDX0, DTDX1 = $\left(\frac{\partial T}{\partial x}\right)_y$ partial derivative for temperature at evaporation boundary

DTLDX = $\left(\frac{\partial T_L}{\partial x}\right)_z$ partial derivative of temperature in liquid at boundary

DTSDX = $\left(\frac{\partial T_s}{\partial x}\right)_z$ partial derivative of temperature in solid at boundary

DYDTO, DYDT1 = $\frac{dy}{dt}$ derivative of evaporation boundary

DZDT, DZDTT, DZDT0, DZDT1 = $\frac{dz}{dt}$ derivative of solid-liquid boundary

EE, SIG = radiation constants ϵ, σ

EMU, EMV = molecular weight of solute and solvent atoms

ET, EA, EB, EC, ED = phase diagram constants

FS, FL = arithmetic functions for solidus and liquidus curves

G = temperature gradient, $^{o}C/cm$

GAMMAO = Y_{vo} - constant term of lateral heat of fusion of solvent

GAMMAT = γ_{vT} - linear term of lateral heat of fusion of solvent

GAMMAU, GMMA = specific heats of solute and solvent

GAMMUO = γ_{uo} - constant term of lateral heat of fusion of solvent

GAMMUT = γ_{uT} - linear term of lateral heat of fusion of solvent

HBO, HB1 = heat balance sum of evaporation and radiation terms

IAM = spacing option: 0 indicates equal, 1 unequal doubling

IFL = indicator of convergence: 2 on convergence, <2 before convergence

IFS = indicator of beginning of solidification: IFS = 0 before solidification

IFS > 0 after solidification

II1 = grid point reference for solid side of mesh

II2 = grid point reference for liquid side of mesh

II3 = grid point reference for evaporation boundary

II4 = grid point reference for point after evaporation boundary

III = grid point reference for point after solidification boundary

IM = number of points in mesh

IT = actual iteration count

ITT = parameter controlling surface temperature condition: -1 for instantaneous temperature drop; 0 for linear temperature drop; 1 for exponential drop. Ratio

IX = maximum number of points in mesh, $\leq$ 28

NIT = maximum iteration count

NITH = half of NIT

NITL = 3/4 NIT

NITQ = quarter of NIT

NONCN = nonconvergence option: 1 indicates proceed and printout
0 indicates proceed but do not printout
-1 indicates program stop

RAT = ratio of current time step over previous time step

RHOO = ρ_{VO} - constant term of density of solvent

RHOGAM = $\rho\,\gamma$ - product of density x latent heat of fusion as determined for concentration of solute and solvent - liquid

RHOT	= ρ_{vT} linear coefficient of density of solvent
RHOUO	= ρ_{uo} - constant term of density of solute
RHOUT	= $\rho_{u,T}$ - linear coefficient of density of solvent
S	= a measure of the closeness a number between 0 and $\frac{1}{2}$ used to determine when computing scheme should change the base mesh point. If the ratio of the distance from interface (solid-liquid) to the next right mesh-point, x_i, to the last mesh interval (x_{i-1}, x_i) is less than s, then mesh point x_{i-1} is used instead of x_i in determining derivatives.
T_1	= temperature of cooler zone
T_2	= temperature at start of solidification
T_S	= time to freeze ZL = ZL/YD
T1	= Lower bound for surface temperature variation.
TA	= ambient temperature
TF	= final time
TI, TII, TI1, TI2	= temperatures at solid-liquid boundary
TIME	= time at beginning of time interval
TIME1	= time at end of time interval
TIME0	= time of start of solidification
TO, CO	= initial temperature and concentration distribution
TPR	= time for printing results
TS	= the time when the lower bound of surface temperature is obtained. After this time, the surface temperature remains constant at T1.
TSI, TSI1, TSI2	= temperatures at evaporation boundary
TTF(V)	= computed temperature as an exponential function of time

TU	= eutectic temperature
TX	= proportion of distance between T_0 and T_2 to that between T_0 and T_1
UE, VE	= arithmetic function definition for evaporation rates
U0, U1	= rates of evaporation of solute
V0, V1	= rates of evaporation of solvent
XKLU	= value of thermal conductivity of solute as liquid
XKLUO	= $k_{\ell uo}$ - constant term for thermal conductivity of solute as liquid
XKLUT	= $k_{\ell ut}$ - linear coefficient for thermal conductivity of solute as liquid
XKLV	= value of thermal conductivity of solvent as liquid
XKLVO	= $k_{\ell vo}$ - constant term for thermal conductivity of solvent as liquid
XKLVT	= $k_{\ell vt}$ - linear coefficient for thermal conductivity of solvent as liquid
XKS, XKL	= k_s , k_ℓ for interphase boundary equation
XKSU	= value of thermal conductivity of solute as solid
XKSUO	= k_{suo} - constant term for thermal conductivity of solute as solid
XKSV	= value of thermal conductivity of solvent as solid
XKSVO	= k_{svt} - constant term for thermal conductivity of solvent as solid
YI, YI1, YI2	= values of y (evaporation boundary)
YD	= is the velocity of solidification, i.e., the velocity of the solid-liquid interface.

YG	= first approximation for the amount of solid
ZI1, ZI2	= values of z (solid-liquid boundary)
ZL	= graded temperature zone length, cm

APPENDIX E

ECONOTECHNICAL MODEL OF CRYSTAL GROWTH

A. Introduction

An econotechnical model of crystal growth can be set up to study the effects of such input variables as growth technique or equipment, alloy system, initial solute concentration, initial melt temperature, and material thermophysical parameters on such output variables as solidification velocity, growth morphology, cooling time to solidification, evaporative material loss at anytime, crystal size and perfection, power consumption, and cost. This model may be in the form of a series of linear equations each expressing an output variable as a linear combination of the value of the input variables multiplied by its unique effect. The model can be more complicated and involves not only main effects but also higher-degree terms and multi-factor interactions. The values of these main effects, higher-degree terms, and interactions can be determined from actual experimental or computer simulation data. Statistical designs are useful in planning the experimental or computer runs so that such determinations may be done with maximum confidence even with limited available data.

When fully developed, these correlation equations will allow the prediction of crystal size, quality, and cost; the systematic selection of best growth equipment or alloy system; the optimization of growth or material parameters; and the maximization of zero-gravity effects.

B. The Model

Specifically, for small changes Δx_i in any of the n (critical or interested) input variables x_i, any output variable S_k can be considered as being linearly related to the various values of the x_i's or Δx_i's, i.e.,

$$S_k = \sum_{i=0}^{n} a_i x_i = a_o x_o + a_i x_i + \ldots + a_n x_n = \bar{S}_k + \sum_{i=1}^{n} a_i \Delta x_i \qquad (1)$$

where the a_i's are the respective effects of the n input variables, and $\bar{S}_k = a_o x_o$ is the average value of the output variable S_k within the experimental domain studied.

An example of use of the models to predict the cooling time to solidification and evaporative material loss at beginning of solidification based on initial melt composition and temperature will be given later in this section.

It can be seen that any effect a_i for the input variable x_i is the partial derivative of S_k with respect to x_i, or

$$a_i = \frac{\delta S_k}{\delta x_i} \tag{2}$$

If we chose a particular set of conditions (i.e., values of x_i's) as the standard or base line conditions and refer to these x_{i,b_ℓ}'s to determine the Δx_i's, then Eq. 1 becomes

$$S_k = S_{k,b_\ell} + \sum_{i=1}^{n} a_i \Delta x_i = S_{k,b_\ell} + \sum_{i=1}^{n} \frac{\partial S_k}{\partial x_i} \Delta x_i \tag{3}$$

where S_{b_ℓ} is the value of S_k at the standard or base level conditions under which all the Δx_i's are zero.

In the more general case, particularly when the Δx_i's are large, the same output variable S_k may be also related to higher-degree terms of one or more of the input variables x_i. Hence the following improved model for S_k:

$$S_k^I = S_{k,b_\ell} + \Sigma a_i \Delta X_i + \Sigma b_i \Delta (x_i^2) + \Sigma d_i \Delta (x_i^3) + \tag{4}$$

Further, the input variables in crystal growth are known to interact strongly. Thus, there is no best growth equipment or alloy system. But there is a best combination of growth equipment and alloy system. Even three or more variable interactions are usually present. The classical approach in which only one variable is changed at a time, therefore, seldom reaches the true or global optimum conditions and often is of limited value.

Also, the even more general model of crystal growth is:

$$S_k^{II} = S_{k,b_\ell} + \Sigma a_i \Delta x_i + \Sigma b_i \Delta (x_i^2) + \Sigma d_i \Delta (x_i^3) + \Sigma f_{ij} \Delta (x_i x_j)$$

$$+ \Sigma g_{ijk} \Delta (x_i \cdot x_j \cdot x_k) + \ldots \tag{5}$$

The value of S_k as observed, i.e., s_k^o, in actual experiments or computer simulations, is always different from the true, S_k, by measurement or computational errors which are assumed to be randomly distributed. Hence,

$$S^o_{k,b_\ell} = S_{k,b_\ell} + e_{b_\ell}$$

and $S_k^o = S_{k,b_\ell} + \Sigma a_i \Delta X_i + e$ for the linear model.

Let us take the special case when the standard or base level conditions are ground level or one-g conditions, while the test conditions are the space or zero-g conditions. The zero-gravity effect on the kth output variable is, then:

$$ZGE_k = \Delta S_k = S^{o}_{k,0g} - S^{o}_{k,1g} = \Sigma a_i \Delta x_i + (e_{b\ell} - e) = \Sigma a_i \Delta x_i + e' \qquad (8)$$

where $e' = \sqrt{2\ e} \doteq \sqrt{2\ e_{b\ell}}$ for $e_{b\ell} \doteq e$.

The procedures for determining these various effects a's, b's, d's, f's, and g's by least-square techniques from the experimental or computer data are fairly straight forward. See, for example, References E1 and E2. Techniques are also available to sequentially determine these same effects or coefficients and automatically adding a new important term or eliminating an unimportant term in the model equations.

These model equations are very similar to those used in statistical design of modern experiments and the subsequent variance analyses (Refs. E1 and E2). In fact, the actual or computer experimental runs should fully use such modern statistical techniques to maximize the yield of reliable information.

C. Optimization Techniques

Once these correlation or prediction equations are established, one can estimate any output variable S_k, with a known degree of confidence, from the known values of the input variables. The procedure to optimize a particular S_k relative to one or two input variables involves simply equating the partial derivative of S_k with respect to these variables to zero and checking to see if the extreme S_k thus obtained is indeed the optimum sought. If several or all the input variables are allowed to vary, one can even use the method of steepest ascent (Ref. E3) to simultaneously vary the input variables x_i's, to minimize the number of required experimental runs, for example, in the expensive space environment.

We can even simultaneously optimize a number of output variables S 's representing , e.g., crystal size, crystal perfection, growth velocity, power consumption, contamination index, and cost. These optimizations may be done with or without certain constraints on the available ranges of the input variables x_i's, with the aid of linear or dynamic programming techniques.

D. Uses of the Model

In summary, when fully developed, this program should enable us to:

1. predict any output variable or growth result upon knowing the values of input variables;

2. detect, analyze, and determine any interactions among the various input variables;

3. Rigorously and quantitatively compare two or more growth methods, equipments, alloy systems,. . . for a desired output variable;

4. Define the best or most promising regions of space crystal growth study;

5. Help to achieve best crystal growth results in space by starting in an optimal growth region and zero in to optimization by the method of steepest ascent;

6. Systematically select the unique combinations of growth parameters (or input variables) for maximized zero-gravity effects;

7. Finding the most cost-effective approach to crystal growth in space; and

8. Putting space crystal growth work as a whole on a more objective, efficient, and scientific basis.

E. Example of Usage

As an example, we used the computer program previously discussed (in Section II for calculating the temperature and concentration distributions in a semi-infinite, Ge-Sb binary alloy liquid under unidirectional cooling through surface evaporation and radiation) to determine the time in seconds to initiate solidification t_{bs}, and the length in centimeters evaporated away before solidification starts. x_{bs}. We assume here that t_{bs} and x_{bs} are the output data we want to optimize through controlled variations of two other controllable parameters, i.e., initial melt temperature T_o in ^oC and initial melt composition c_o in moles. The use of the techniques described in this section, and even of the particular prediction equations for t_{bs} and x_{bs}, will be shown.

The variations of the time to solidification and length of evaporated material with T_o and c_o are shown below for the system of antimony in germanium:

Table E-1 Variation of t_{bs} (x 10^{-3} sec) with T_o and c_o

c_o/T_o	970	980	990°C	Average
0.01	0.9	1.5	1.9	1.4
0.02	1.0	1.6	2.1	1.6
0.03	1.2	1.7	2.2	1.7
0.04	1.3	1.8	2.4	1.8
Average	1.1	1.7	2.2	1.6

Table E-2 Variation of x_{bs} (x 10^{-6} cm) with T_o and c_o

c_o/T_o	970	980	990° C	Average
0.01	0.5	0.8	1.3	0.9
0.02	1.2	1.9	2.6	1.9
0.03	1.9	3.0	4.2	3.0
0.04	2.8	4.3	5.8	4.3
Average	1.6	2.5	3.5	2.5

Multiple regression analyses (Refs. E4 and E5) of these data gave the following prediction equations:

1) for the time in ms to indicate solidification, t_{bs} in ms

$$t_{bs}^{1} = 1.030 + 21.4\,C_o \pm 0.60 \quad (1)$$

$$t_{bs}^{2} = -59.81 + 0.0626\,T_o \pm 0.34 \quad (2)$$

$$t_{bs}^{3} = -60.34 + 21.4\,C_o + 0.0626\,T_o \pm 0.23 \quad (3)$$

$$t_{bs}^{4} = 0.692 + 55.2\,C_o - 675\,C_o^{2} \pm 0.66 \quad (4)$$

$$t_{bs}^{5} = -1277.18 + 2.55\,T_o - 0.00127\,T_o^{2} \pm 0.37 \quad (5)$$

$$t_{bs}^{6} = 60.68 + 55.2\,C_o - 675\,C_o^{2} + 0.0626\,T_o \pm 0.25 \quad (6)$$

$$t_{bs}^{7} = -1278 + 21.4\,C_o + 2.55\,T_o - 0.00127\,T_o^{2} \pm 0.25 \quad (7)$$

$$t_{bs}^{8} = -1277.06 + 55.2\,C_o - 676\,C_o^{2} + 2.55\,T_o - 0.00127\,T_o^{2} \pm 0.26 \quad (8)$$

2) for the thickness evaporated away before solidification, x_{bs} in 10^{-6} cm

$$x_{bs}^{1} = -0.333 + 114.3\,C_o \pm 0.92 \quad (9)$$

$$x_{bs}^{2} = -89.35 \text{ to } 0.0938\,T_o \pm 1.45 \quad (10)$$

$$x_{bs}^{3} = 92.21 + 114.3\ \ C_o t\ \ 0.0938\,T_o \pm 0.42 \quad (11)$$

$$x_{bs}^{4} = 0.04174 + 85.17\,C_o + 583.2\,C_o^{2} \pm 1.02 \quad (12)$$

$$x_{bs}^{5} = 278.12 - 0.656\,T_o + 0.00038\,T_o^{2} \pm 1.60 \quad (13)$$

$$x_{bs}^{6} = -91.92 + 85.17\,C_o + 583.2\,C_o^{2} + 0.0938\,T_o \pm 0.47 \quad (14)$$

$$x_{bs}^{7} = 273.90 - 0.6535\,T_o + 0.00038\,T_o^{2} + 114.3\,C_o \pm 0.47 \quad (15)$$

$$x_{bs}^{8} = 277.80 + 85.16\,C_o + 583.37\,C_o^{2} - 0.6608\,T_o + 0.00038\,T_o^{2} \pm 0.53 \quad (16)$$

The first two prediction equations in each case relates t_{bs} or x_{bs} to one independent variable, C_o or T_o. The third equation is a linear prediction equation involving both C_o and T_o. The last five equations involve the squared C_o terms, squared T_o terms, or both. The numbers after the "$\pm$" sign in each equation is the "adjusted standard error" (Refs. E4 and E5).

Thus, t_{bs} can be computed from known values of C_o and T_o according to Eq. 3 with an error of 0.23. 90% of the time, the computed t_{bs} value of (Y estimated) is off from the true value of (Y observed) by 2 x 0.23 = 0.46 ms. as also can be seen from Table E-3.

Similarly x_{bs} can be predicted from known values of C_o and T_o, according to Eq. 11, with an error of 0.42. 90% of the time, the computed x_{bs} value (Y estimated) is off from the true value (Y observed) by 2 x 0.42 = 0.84 sec., as can also be seen from Table E-3.

Table E-3 Summary of Statistical Significances

For t_{bs}

Eq.	Independent Variable	Adjusted Standard Error	Adjusted Regression Coefficient	Variance Ratio, F	Significance Level
1	C_o	0.60 ms	0.4014	1.921	<90%
2	T_o	0.34	0.8566	27.56	99.9%
3	C_o, T_o	0.23	0.9404	38.31	99.9%
4	C_o, C_o^2	0.66	0.3022	0.948	<90%
5	T_o, T_o^2	0.37	0.8474	13.06	99%
6	C_o, C_o^2, T_o	0.25	0.9419	26.21	99.9%
7	$C_o T_o, T_o^2$	0.25	0.9401	25.37	99.9%
8	C_o, C_o^2, T_o, T_o^2	0.26	0.9417	19.51	99.9%

For x_{bs}

Eq.	Independent Variable	Adjusted Standard Error	Adjusted Regression Coefficient	Variance Ratio, F	Significance Level
9	C_o	0.92×10^{-6}	0.8353	23.08	99.9%
10	T_o	1.45	0.5002	3.34	90%
11	C_o, T_o	0.42	0.9709	81.94	99.9%
12	C_o, C_o^2	1.02	0.8180	10.46	95%
13	T_o, T_o^2	1.60	0.4187	1.503	<90%
14	$C_o, C_o 2, T_o$	0.47	0.9686	50.02	99.9%
15	T_o, T_o^2, C_o	0.47	0.9678	48.69	99.9%
16	C_o, C_o^2, T_o, T_o^2	0.53	0.9647	32.92	99.9%

Table E-3 gives the different sets of independent variables used for the above 16 prediction equations for t_{bs} and x_{bs}. Also tabulated are the adjusted standard errors, adjusted regression coefficients, the values of F ratio, and the significance levels (Refs. E3 and E4).

One sees again from this table that the time to solidification t_{bs} depends not much on C_o, but strongly on T_o. The best prediction equation is a linear equation in C_o and T_o, i.e., Eq. 3 (error 0.23 ms). On the other hand, the loss of material due to evaporation before solidification depends strongly on C_o, but not much on T_o, although the best prediction equation for x_{bs} is also a linear equation in C_o and T_o i.e., Eq. 11 (error 42 Å).

In designing or conducting space processing experiments, it is important to know the time of evaporation before solidification t_{bs}. In many cases, this time may be too long to fit into, e.g., a rocket program, or the surface composition may be too much changed from the intended initial composition to be useful. In other cases, this time t_{bs} may be too short for proper instrumentation and recording, e.g., the beginning of solidification or nucleation. Eq. 1-8 given above may, therefore, be used for Ge-Sb alloys within the initial concentration & temperature ranges studied. Of course, other ranges of the same or different alloys can also be similarly studied using the same models and techniques described above.

The material evaporated away before solidification x_{bs} is also important in certain critical space processing operations such as the manufacture of precision parts including thin films.

References

E1. Anderson, R. and Bancroft T., Statistical Theory in Research, McGraw-Hill, New York, 1952

E2. Nalimov, V. and Chernova, N., Statistical Methods for Design of Extreme Experiments, DOD Report AD 673,747, 1968

E3. Davis. O. L., Ed. The Design and Analysis of Industrial Experiments, Second Ed., Hafner, New York, 1971

E4. Bennett, Carl A. and Franklin N. L., Statistical Analysis in Chemistry and The Chemical Industry, Wiley, New York, 1954. Appendix 6A

E5. System/360 Scientific Subroutine Package, Programmer's Manual, H20-0205, IBM, 1966.